Summer 1998

Microhollow Cathode Discharge Excimer Lamps

Ahmed El-Habachi
Old Dominion University

Recommended Citation

El-Habachi, Ahmed. "Microhollow Cathode Discharge Excimer Lamps" (1998). Doctor of Philosophy (PhD), Dissertation, Electrical & Computer Engineering, Old Dominion University, DOI: 10.25777/sq0g-rx89
https://digitalcommons.odu.edu/ece_etds/73

MICROHOLLOW CATHODE DISCHARGE EXCIMER LAMPS

by

Ahmed El-Habachi
B.Sc. June 1991, University of Alexandria, Egypt
M.Sc. March 1994, University of Alexandria, Egypt

A Dissertation Submitted to the Faculty of
Old Dominion University in Partial Fulfillment of the
Requirement for the Degree of

DOCTOR OF PHILOSOPHY

ELECTRICAL ENGINEERING

OLD DOMINION UNIVERSITY
August 1998

Approved by:

Karl H. Schoenbach (Director)

Hani El-Sayed Ali (Member)

Ravindra Joshi (Member)

Leposava Vuskovic (Member)

ABSTRACT

MICROHOLLOW CATHODE DISCHARGE EXCIMER LAMPS

Ahmed El-Habachi
Old Dominion University, 1998
Director: Dr. Karl H. Schoenbach

Microhollow cathode discharges are non-thermal discharges of such small sizes that thermalization of the electrons is prevented. By reducing the diameter of the cathode opening in these discharge geometries to values on the order of 100 μm we were able to operate discharges in argon and xenon in a direct current mode up to atmospheric pressure. The large concentration of high electrons, in combination with high pressures favors three body processes such as excimer formation. This was confirmed by experiments in xenon and argon where emission of excimer radiation at 172 nm and 130 nm, respectively, was observed when the pressure was increased beyond 50 Torr. The intensity of excimer radiation in xenon excimer emitters was found to have a maximum at 400 Torr. At this pressure, the VUV radiant flux of a single discharge operating at currents greater than 2 mA and a forward voltage of 220 V reaches values between 6% and 9% of the input electrical power. These are values, which are comparable to those achieved in barrier discharge excimer lamps. Results of a simple rate equation model indicate that even higher efficiencies (40%) might be achievable. The VUV intensity scales linearly with discharge current, which makes analog control of the excimer emission with semiconductor devices possible.

The possibility to form arrays of these discharges will allow the generation of dc-flat panel excimer lamps with radiant emittances exceeding 60 W/cm^2. Applications for such lamps are lighting, flat panel displays, optical surface processing, pollution control and many others.

ACKNOWLEDGEMENTS

I would like to express my deepest appreciation to my supervisor, Dr. Karl Schoenbach, whose brilliant insight into the work gave me the much needed direction and inspiration in the conception and writing of this thesis. Without his original ideas and thoughtful criticism, this thesis would never have come to fruition. I thank him for his valuable time, for his unrelenting encouragement and praise, and for his belief on me. It has been an honor and a privilege to work with him.

Special thanks are due to Dr. Hani El Sayed for his continuous help and encouragement, which were a main asset in achieving this work.

My appreciation also goes to Dr. R. Joshi and Dr. L. Vuskovic for accepting to serve in my committee.

In addition, I would like to express my gratitude to Dr. R. Stark and to my colleague W. Shi for their help on this research, Dr. D. Manos and J. Ametepe, College of William and Mary, for stimulating discussions and for valuable information.

Finally, I would like to thank my parents, Mohamed El Habachi and Nesmat Amin. Your vision for me set the direction for my life. Your desire for excellence motivated me to follow in your footsteps. I hope that God will give me the strength and the endurance that I may continue the examples you have set. I pray that God will bless you and give you happy and long lives.

I dedicate this work to my wife, Nancy Nabil. The love and encouragement I received from her sustained me throughout this endeavor. Her sacrifices made this dissertation possible. Words cannot adequately express my love and appreciation for her.

TABLE OF CONTENTS

Page

LIST OF TABLES.. x
LIST OF FIGURES.. xi

CHAPTER

I. INTRODUCTION... 1
    CONVENTIONAL UV SOURCES.................................. 1
    EXCIMER LAMPS.. 3
    APPLICATION OF EXCIMER LAMPS............................. 6
        MERCURY FREE FLAT LAMP FOR LIGHTING........ 6
        MATERIAL DEPOSITION................................... 9
        UV CURING.. 11
        SURFACE MODIFICATION AND PHOTO ETCHING.. 12
        POLLUTION CONTROL..................................... 13
II. EXCIMERS.. 14
    THEORY OF EXCIMER FORMATION............................ 15
    KINETIC MODEL.. 18
        PRODUCTION OF THE EXCIMER PRECURSORS... 18
        EXCIMER FORMATION..................................... 22
        EXCIMER DECAY MECHANISM AND LOSS PROCESSES.. 23
III. EXCIMER GENERATION MECHANISMS............................. 26
    GAS DISCHARGE EXCIMER FORMATION..................... 26

NON-THERMAL PLASMAS.. 27

GENERATION OF EXCIMERS USING NON-THERMAL DISCHARGES.. 28

SILENT DISCHARGE.. 28

THEORY OF SILENT DISCHARGE FORMATION.. 29

SILENT DISCHARGE CHARACTERISTICS.... 31

MICRODICHARGES................................. 32

EXCIMER LAMPS BASED ON SILENT DISCHARGE.. 34

OTHER MECHANIMS OF EXCIMER GENERATION.. 36

MICROWAVE DISCHARGES...................... 36

JET DISCHARGES.................................. 40

IV. MICROHOLLOW CATHODE DISCHARGES......................... 42

HOLLOW CATHODE EFFECT..................................... 42

DIFFERENT MECHANISMS RESPONSIBLE FOR THE HOLLOW CATHODE EFFECT...................... 46

DISCHARGE ELECTRICAL BEHAVIOR.......................... 48

ELECTRON ENERGY DISTRIBUTION FUNCTION........... 51

SCALING OF HOLLOW CATHODE DISCHARGES........... 53

LOWER LIMIT OF THE HOLLOW CATHODE DISCHARGE.. 55

UPPER LIMIT OF THE HOLLOW CATHODE

DISCHARGE.. 55

MICROHOLLOW CATHODE DISCHARGE EXCIMER LAMPS.. 57

V. EXPERIMENTAL SET-UP AND PROCEDURES..................... 60

ELECTRODE GEOMETRY.. 60

MHCD EXPERIMENTAL SET-UP................................ 62

DISCHARGE CHAMBER.................................. 62

ELECTRICAL CIRCUIT..................................... 62

VACUUM SYSTEM... 66

EXPERIMENTAL SET-UP FOR VUV SPECTROSCOPY...... 66

MCPHERSON MODEL 219 VACUUM SPECTROGRAPH / MONOCHROMATOR............. 68

MODIFIED MODEL 650 DETECTOR ASSEMBLY..... 68

MCPHERSON MODEL 789A-3 STEPPER DRIVE SCAN CONTROLLER....................................... 70

COMPUTER PROGRAM OVERVIEW.................... 70

VACUUM PROVISION...................................... 71

SPECTRAL CALIBRATION... 71

SAMPLE CONDITIONING.. 72

EFFECT OF SAMPLE CONDITIONING.................. 73

ABSOLUTE MEASUREMENTS..................................... 73

CALIBRATED SOURCES.................................. 74

RADIOMETER TECHNIQUES............................. 76

VI. RESULTS.. 79

SPECTRAL MEASUREMENTS.. 79

ARGON.. 79

XENON.. 82

ELECTRICAL MEASUREMNTS...................................... 86

ARGON 86

XENON. 92

LIFETIME MEASUREMNT.. 94

ABSOLUTE MEASUREMENTS.. 98

VII. DISCUSSION.. 101

PRESSURE AND CURRRENT DEPENDENCE OF EXCIMER EMISSION.. 101

ELECTRON ENERGY.. 101

EXCIMER MODELING.. 103

EFFECT OF CURRENT.. 105

EFFECT OF CONTAMINANTS.. 105

INCREASING THE DISCHARGE VOLTAGE........... 105

REDUCING EXCIMER GENERATION.................... 108

ABSOLUTE MEASUREMENTS.. 110

VIII. SUMMARY AND CONCLUSIONS.................................... 113

REFERENCES.. 117

APPENDIX... 123

VITA.. 132

LIST OF TABLES

Table Page

2.1. Different resonance lines and excimer continua of Ar, Kr and Xe.......... 14

2.2. Radiative lifetimes of excimer states.......... 24

3.1. Characteristic microdischarge properties in silent discharges... 34

3.2. Specifications of the microwave excimer lamp.......... 39

A.1. Kinetic model for xenon.......... 123

LIST OF FIGURES

FIGURE Page

1.1 Emission spectra of different excimers.................................. 4

1.2 Selection of wavelength in excimer lamps.............................. 5

1.3 Simplified potential energy diagram of molecular xenon........... 7

1.4 Different excimer lamp geometries...................................... 8

1.5 Flat panel excimer lamps (Osram Planon Lamp)..................... 10

2.1 Part of the potential energy diagram of xenon and corresponding excimer emission.. 16

2.2 Relation between mean energy of the electrons, reduced electric field E/n and the product of particle density n times gap spacing d for xenon.. 17

2.3 Schematic of excimer formation.. 19

2.4 Scheme of interactions between atomic and molecular xenon..... 20

3.1 Photograph of microdischarges in silent discharges................. 30

3.2 The life cycle of one microdischarge in silent discharges........... 33

3.3 Silent discharge excimer lamp... 35

3.4 Emission spectra of different silent discharge excimer lamps.. 37

3.5 a- Calculated efficiency of VUV generation of silent discharges in xenon as a function of the reduced field E/n.......................... 38

3.5 b- Calculated efficiencies of the three emission features of silent discharges in xenon as a function of pressure.............................. 38

3.6 Jet discharge excimer generation.. 41

4.1 Some typical hollow cathode geometries................................ 43

4.2 Different discharge modes.. 45

4.3 Current –voltage characteristics for hollow cathode and plane cathode geometries.. 49

4.4 Contour of constant potential at four different points, with dots superimposed to indicate representative ionization events.............. 50

4.5 Comparison of the electron energy distribution functions in a hollow cathode and in a positive column.................................... 52

4.6 Measured electron energy distribution function in hollow cathode discharge using retarding field analyzer.................................... 54

4.7 Microhollow cathode discharge excimer lamp......................... 59

5.1 Different hollow cathode discharge geometries....................... 61

5.2 MHCD experimental set-up.. 63

5.3 Discharge chamber.. 64

5.4 Cross section of the gas discharge gap, and electrical circuit...... 65

5.5 Experimental set-up for VUV spectroscopy.............................. 67

5.6 Picture of the real system... 69

5.7 Radiometer measurements... 77

6.1 VUV spectra of discharges in argon at pressures of 76 Torr, 320 Torr and 760 Torr with a cathode hole diameter of D = 200 μm........ 80

6.2 VUV spectra of discharges in argon at 76 and 600 Torr with a cathode hole of 100 μm.. 81

6.3 VUV spectra of discharges in argon at 700 Torr with different flow rate.. 83

6.4 VUV spectrum of discharges in xenon at 745 Torr with cathode hole of 200 μm 84

6.5 VUV spectra of discharges in xenon at 76 and 760 Torr with a cathode hole of 100 μm 85

6.6 Pressure dependence of the VUV emission spectrum of high pressure microhollow cathode discharges in xenon........................ 87

6.7 The increase of the peak value of the argon excimer line with increasing current for a cathode hole D = 200 μm 88

6.8 Temporal development of voltage and current of streamer-like discharges in argon at 896 Torr... 90

6.9 Voltage-current characteristics of microhollow cathode discharges in argon (600 Torr) and corresponding current-dependence intensities of the argon excimer radiation at 130 nm...... 91

6.10 Voltage-current characteristics of microhollow cathode discharges in xenon (745 Torr) and corresponding current-dependent intensities of the xenon excimer radiation at 172 nm....... 93

6.11 Voltage current characteristics of microhollow cathode discharges in xenon (435 Torr) and corresponding current-dependent intensities of the xenon excimer radiation at 172 nm....... 95

6.12 Decay of the excimer radiation intensity with time for discharges with non conditioned samples.................................. 96

6.13 Comparison of the decay of the excimer line in the two applied method for sample conditioning... 97

6.14 Measured efficiency of the xenon excimer radiation versus pressure... 99

6.15 Intensity of the xenon excimer radiation versus discharge current and corresponding efficiency.. 100

7.1 Pressure dependence of the xenon spectrum in silent discharge. 102

7.2 Comparison of the results of the experiment and the model........ 106

7.3 Inverse square law approximation error................................ 111

A.1 Calibrated deuterium lamp spectrum.................................. 127

A.2 Low pressure mercury arc spectrum.................................. 128

A.3 Spectral responsivity of the SED 185 deep UV detector........... 130

A.4 Curve fitting of the xenon excimer line................................ 131

CHAPTER I

INTRODUCTION

Excimer lasers have become a major research tool wherever high intensity ultraviolet radiation is required. Their wavelengths range from 158 nm of the fluorine laser to 351 nm of the xenon fluoride laser and average UV powers from a few watts to a few hundred watts. Their applications extend from photo-induced chemical reactions to micro machining.

In many of these applications neither monochromatic nor coherent radiation is required and the laser is simply used as a high intensity photon source. For such applications incoherent ultraviolet sources may provide an interesting alternative to lasers, especially when large areas or large volumes have to be irradiated. An additional reason for using UV lamps may be that the required power levels and reliability go beyond the capabilities of today's excimer lasers. Finally, a major advantage of replacing lasers by UV sources in large area processing is their much lower cost compared with lasers.

1.1 Conventional UV Sources

The most important UV source available is the low-pressure glow discharge in a mercury/ rare gas mixture. Under optimum conditions the plasma column can convert electrical energy into UV radiation with high efficiency: 60-70% of the electrical input power is radiated at 253.7 nm and roughly 10% at 184.9 nm. Because of this high efficiency the same discharge is also used for the generation of visible light in connection with suitable phosphors as wavelength converters. Fluorescent lamps replacing the incandescent light bulbs are based

---

Journal model for this thesis is *Applied Physics Letters*.

on the mercury vapor discharge. In the visible spectral range the combination of UV generation and phosphor is about four times as efficient as the incandescent lamp which reaches only 4% energy efficiency. Unfortunately these optimum discharge conditions can be maintained only at fairly low electrical power densities of less than 100 mW/cm^3 of plasma column and at low mercury vapor pressures of about 7.5 mTorr. The UV output of these lamps can reach 0.2 W/cm of the discharge column.

If a higher photon flux is required different discharge conditions must be chosen. Much higher UV intensities can be obtained from arc discharges, which are operated at medium pressure. In many medium pressure mercury arcs the 366 nm line is the strongest line which reaches efficiencies of about 4-6%. Additional lines appear at 313, 405, 436, 546 and 548 nm. These lamps are offered by many producers at electrical powers between 0.1 and 60 kW.

Higher photon fluxes are obtained from high-pressure arc discharges, which in most cases are short arcs in mercury, xenon or also mixtures of these gases. Typical powers lie between 75 W and 30 kW. Their spectrum is characterized by a wide spread continuum with some superimposed lines. Efficiencies at the strongest lines are at best of the order of 1%, which means that rather efficient filters are required if monochromatic radiation is needed. In addition, heat removal may become a serious problem. In principle, we have the choice between excellent efficiencies at very low UV intensities or higher intensities at considerably reduced efficiencies.

1.2 Excimer Lamps

Excimers are weakly bound complexes which do not possess a stable ground state (e.g. rare gas excimers: He_2^*,Ne_2^*,Xe_2^* or rare gas halides: ArF*, KrF*, Xecl*, XeF*). These excimer molecules disintegrate within less than a microsecond and during their decay give off their binding energy in the form of UV or VUV radiation.

Lamps, which utilize this effect, are quasi-monochromatic light sources generating UV and VUV in a very narrow band [Fig. 1.1 [1]]. As an example, Xe_2^* radiation peaks at 172nm and has a half width of 14nm. No other emission is observed between 150 and 400 nm. A wide selection of UV wavelengths can be obtained from different excimers as shown in Fig. 1.2 [2].

Excimer lamps do not produce infra red radiation. The lamps are therefore relatively cold and can reach surface temperature of 35-40^{0}C [3]. Heating of the irradiated material is therefore largely avoided, and the lamp can be used to process heat sensitive substrates. Low temperature processing is extremely important for future generation Si ultra large-scale integration (ULSI). In addition, lower temperatures allow greater exploitation of new materials, which have not been previously tried due to their high temperature incompatibility.

The fact that excimer lamps are non-coherent radiation source allows to scale the lamps to large size and to use them to irradiate and treat large areas. The noble gases, which have received particular attention, are xenon and argon. In the case of xenon, it is possible to use high quality quartz as discharge windows. Whereas, for argon, more expensive materials such as magnesium

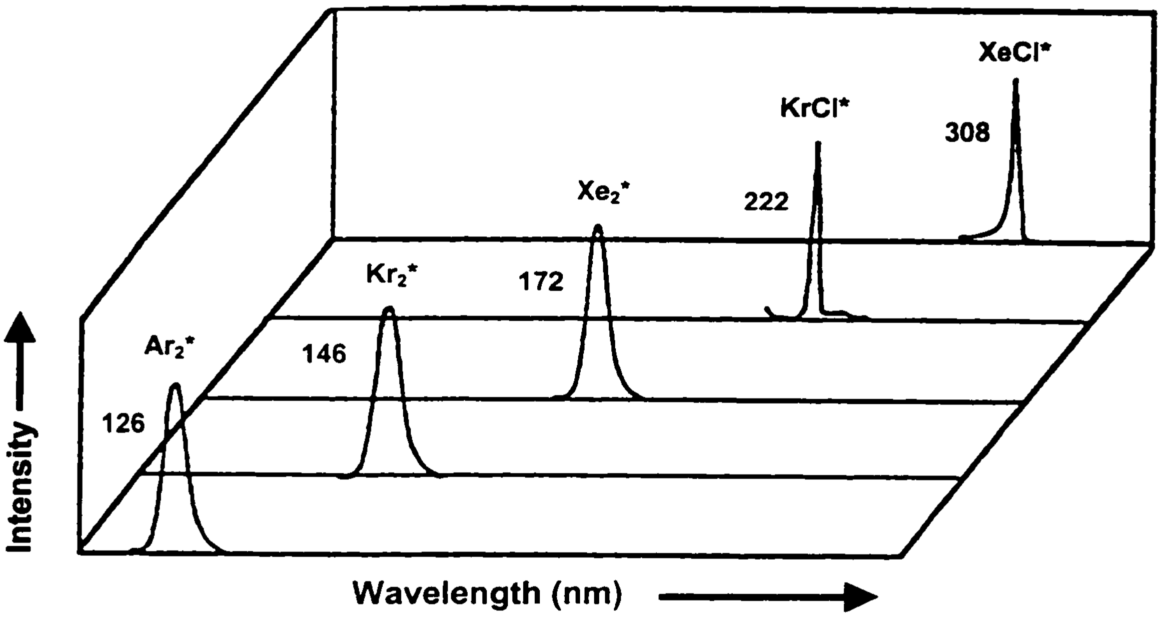

FIG. 1.1. Emission spectra of different excimers [1].

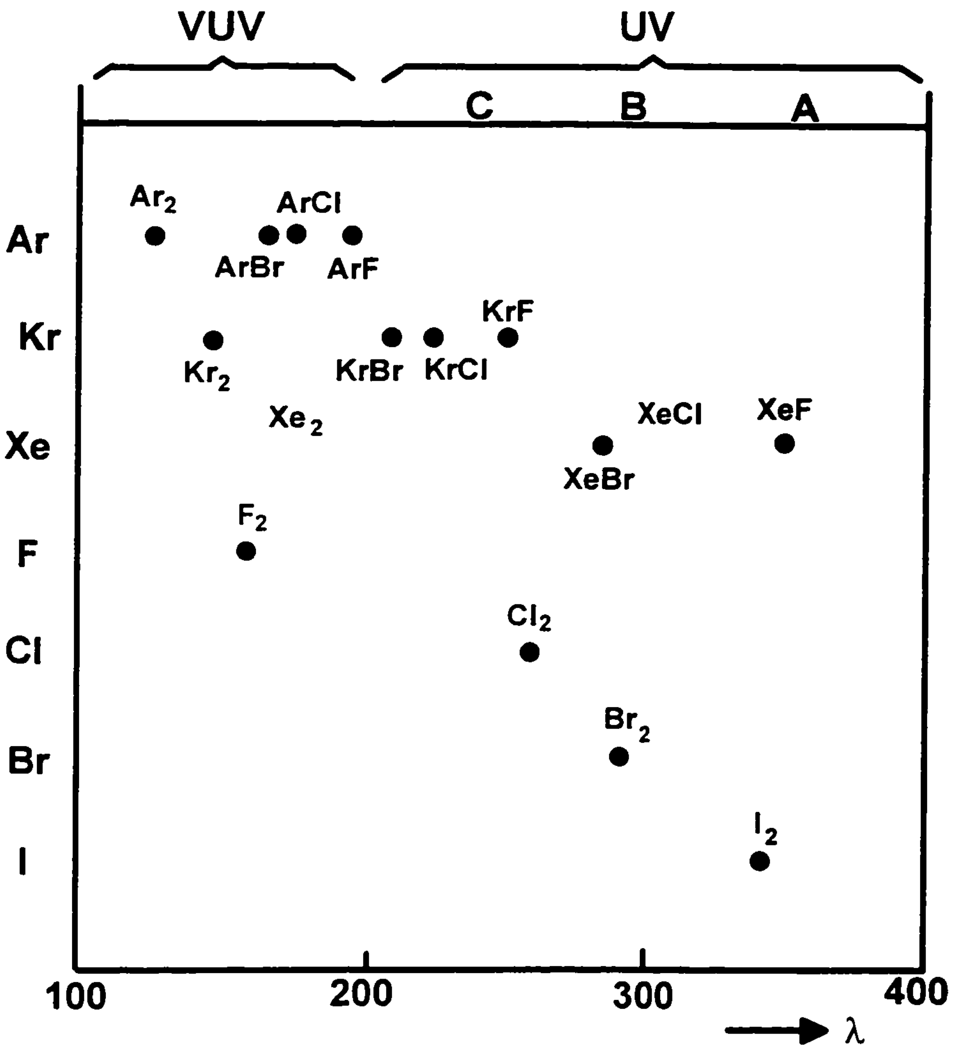

FIG. 1.2. Selection of wavelength in excimer lamps [2].

fluoride are required. Compared with xenon, argon is a relatively inexpensive gas, therefore, windowless lamps may be used. The substrate, which is being processed, can be placed in the same argon atmosphere that is used by the lamp [4].

Excimer lamps have a high efficiency, which may reach 30%[5]. The main reason for this high efficiency in a gas at high pressure is the absence of radiation trapping and absorption. Since excimers do not possess a stable ground state [Fig. 1.3 [6]], reabsorption of the radiation cannot occur.

Moreover, excimer lamps can be shaped as large radiating panels or cylinders, designed to radiate outside or inside. This property has advantages for the treatment of cylindrical objects or the irradiation of a medium flowing through a pipe. Fig. 1.4 [7] shows different excimer lamp geometries.

1.3 Application of Excimer Lamps

1.3.1 Mercury Free Flat Lamp for Lighting

So far, most LCD monitors have been illuminated by light guide systems with miniature tubular fluorescent lamps. In contrast, Excimer flat lamps are one centimeter thick, shaped like a tile and have precisely the same dimensions as the screen itself (15 to 20 inches). Hence there is no need for complex optical systems to distribute the light and the monitor is illuminated absolutely evenly. The lamp can supply high quality light for 50,000 hours [8]. Compared with miniature fluorescent lamps that have to be replaced after 20,000 hours because they are not bright enough. Light is generated in much the same way as in classic fluorescent lamps. A gas discharge produces VUV radiation, which is

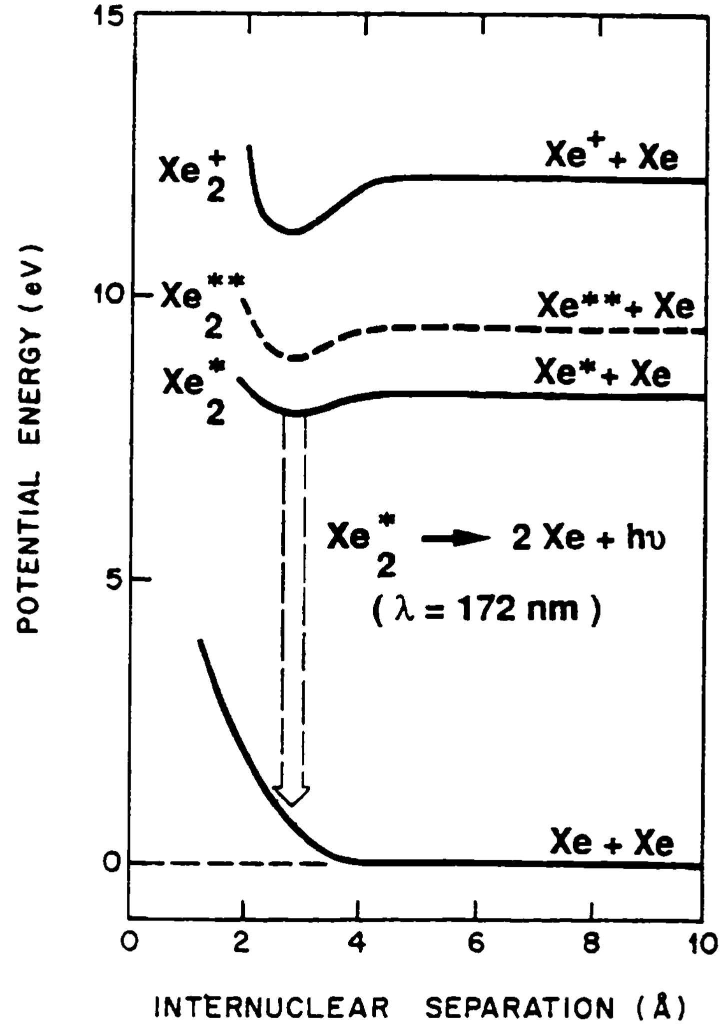

FIG. 1.3. Simplified potential energy diagram of molecular xenon [6].

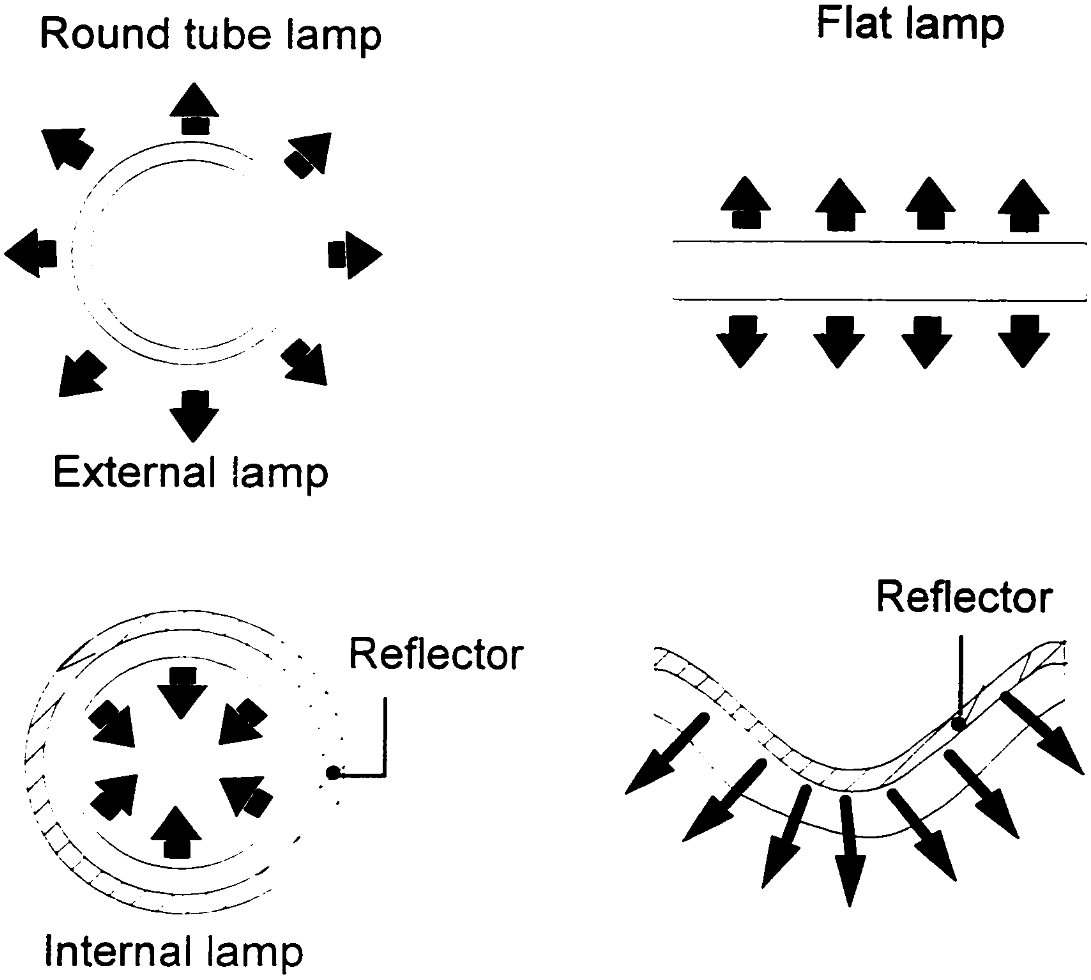

FIG. 1.4. Different excimer lamp geometries [7].

converted into visible light by means of phosphor. The difference is that the lamp is not filled with mercury vapor but with inert gas (xenon as an example). The absence of mercury means that there is no need for any special waste disposal arrangements. Additional benefit from using excimers is that the lamp instantly supplies its maximum luminous intensity at any temperature independent of ambient temperature. Conventional fluorescent lamps, on the other hand, operate at full efficiency only within a narrow temperature range and take some time to reach their optimum output. For the first time, this technology for generating light is commercially viable [9]. Fig. 1.5 shows a picture of a flat lamp based on excimer formation. This lamp will be available in the market by the end of this year. At 25 lm/W, the luminous efficacy of these systems is comparable to that of traditional back lighting devices for LCD monitors.

However, the luminous efficacy of this new lamp technology is only half as high as that of mercury based fluorescent lamps. The reason is that the phosphor is less efficient at converting VUV into visible light. Thus, the major challenge to researches is to develop new phosphors to make this technology more powerful and open up applications even in general lighting. It is expected that within few years this recent application of excimer formation will become the most important one as far as sales volumes are concerned.

1.3.2 Material Deposition

Excimer lamps emitting UV and VUV radiation were shown to be a very useful tools for the photo cleavage of precursor substances that lead to the deposition of metallic, dielectric or semi conducting layers. Substantial work has

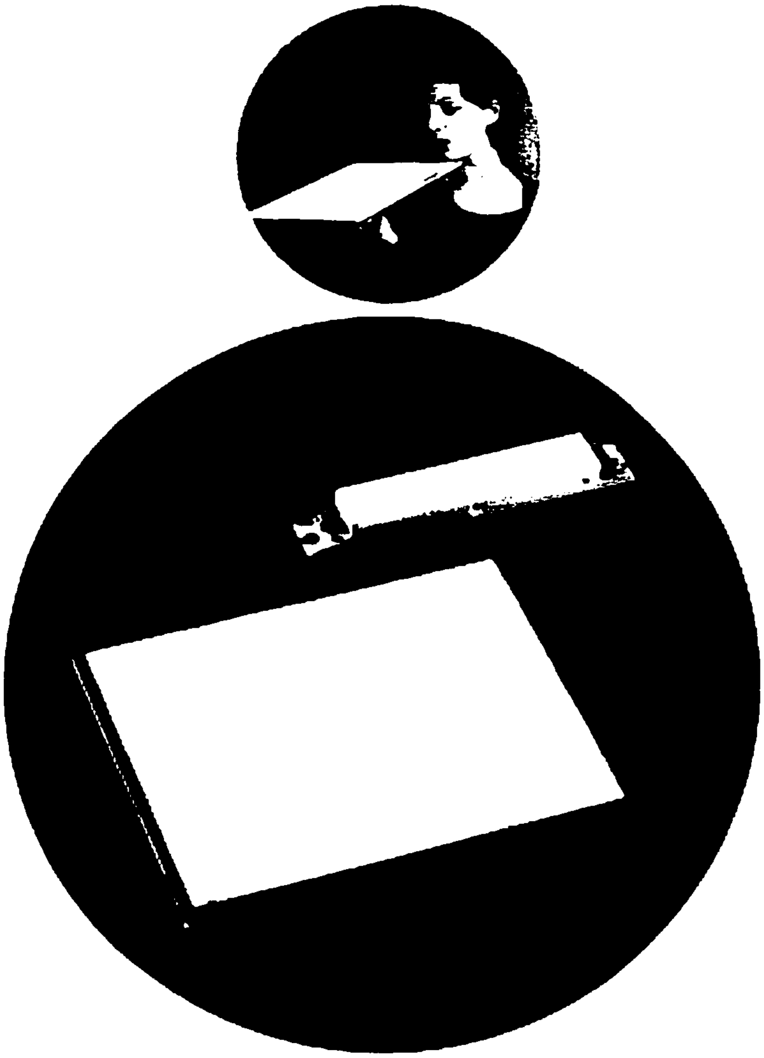

FIG. 1.5. Flat panel excimer lamps (OSRAM PLANON lamp) [8].

been reported on the mechanism of area selective deposition of copper structures following UV induced palladium nucleation from palladium (II) acetate precursor films [10-11]. This low temperature metallization has potential applications in microcircuits, multi chip interconnects and prototype. Few years ago, this process was brought to technical maturity in the Brite/EuRam PACE project focusing in Photo Assisted Catalysis of Electroless Plating (PACEP).

Photo induced deposition of insulating films has become an important application of excimer lamps. Low temperature deposition of good quality silicon dioxide and silicon nitride films was obtained by irradiating silane/nitrous oxide/ ammonia mixtures [12-13]. Also irradiating tantalum ethoxide sol-gel films with a xenon excimer lamp formed tantalum oxide films. Due to its high dielectric constant about 25 it is a promising candidate as a capacitor dielectric in high density dynamic assess memories (DRAMS) and in ultra large scale integrated (ULSI) devices.

1.3.3 UV Curing

UV curing is the polymerization of special paints, varnishes, adhesives and sealing or casting compounds as a result of their exposure to UV radiation. UV curing allows using paint in a fraction of a second and does not cause any solvent emissions. Typical applications include decorative and protective coatings on metal, wood and plastic material: sealing of hard wood and vinyl flooring, scratch resistant top coats on vinyl films, polycarbonate and molded parts like automotive headlamp reflectors. More sophisticated applications can be found in optical fiber coatings and in the electronic industry irradiating photo resists and conformal coatings used in the manufactory of printed circuit boards. In all these applications rapid polymerization is initiated by the UV induced cleavage of special photo initiator molecules resulting in free radicals that can start a chain reaction [14].

1.3.4 Surface Modification and Photo Etching

Industrial applications of metallized plastics in the automotive industry and in the fields of EM shielding require large area treatment of surfaces. Hence, controlled large area modification of polymer surface properties by the interaction of energetic photons with the surface is a field of considerable technical importance. VUV lamp open excellent possibilities for efficient large area surface treatment [15].

Excimer lamps have been demonstrated to be very useful for large area photochemical dry etching of Polytetrafluoroethylene PTFE [16] and Polyamide PI [17]. This suggests their application in micro machining polymer materials. Applications could include manufacturing of optical storage devices and certain processes in multi layer circuit fabrication like drilling through holes in thin polyamide and other polymer layers.

Also dry photochemical selective etching of InGaAs on InAlAs was demonstrated with a xenon excimer lamp [18]. An excellent selectivity of over 100 was achieved for this material system. Important applications are foreseen for the fabrication of electrical as well as optical devices using InGaAs/InAlAs hetero junctions, e.g. high electron mobility transistors (HEMT) for microwave applications.

1.3.5 Pollution Control

The availability of new intense VUV and UV sources prompted a number of investigations in the photodegradation of pollutants in gaseous and aqueous media [19]. Many of the common pollutants absorb strongly in the ultraviolet spectral range close to 200 nm. Their molecular absorption cross sections can be well in excess of 10^{-17} cm^2. This value is more than million times larger than that of water or air in this spectral range. Consequently selective photodegradation of micro pollutants at low concentration becomes possible [20]. In general, the VUV process is very simple and has the particular advantage that no chemicals need to be added. The process represents a real challenge to other photochemical water treatment processes. Treatment of contaminated surface water, ground water as well as wastewater containing biocidal or nonbiodegradable components is under investigation.

CHAPTER II

EXCIMERS

Excimers are weakly bound complexes (excited dimers, trimers) of molecules that under normal conditions do not possess a stable ground state. Examples are rare gas excimers: He_2^*,Ne_2^*,Xe_2^* or rare gas halides: ArF*, KrF*, Xecl*, XeF*. These excimer molecules disintegrate within less than a microsecond and during their decay give off their binding energy in the form of UV or VUV radiation. In most cases this radiation is confined to a fairly narrow wavelength region.

Table 2.1. Different resonance lines and excimer continua of Ar, Kr and Xe.

Rare Gas	Resonance line	First continum	Second continum
Ar	106.4	110	126
Kr	123.6	125	146
Xe	146.96	150	172

Rare gas excimers are well known for emitting bright continua and resonance lines in a wavelength range from 100 – 200 nm. Table 2.1 shows the different resonance lines and continua of Ar, Kr and Xe rare gases, created by discharge excitation. The resonance line arises from transitions from the $^3P_1$ excited states to the $^1S_0$ ground state. The second continuum results from transitions from the lowest vibrational level of the singlet $^1\Sigma$ and the triplet $^3\Sigma$ excimer states to the repulsive ground state. Transitions from higher vibrational levels of these states correspond to the first excimer continuum. In Fig. 2.1 [21] the potential energy diagram of xenon and its corresponding excimer emission is presented.

2.1 Theory of Excimer Formation

To form excimers, atoms and molecules must be excited. Excitation can be electronic, photonic or through collisions with ions or neutrals. The electron excitation rate in a gas discharge depends on the applied electric field, E, and the length of path through which the electron travels before it collides with a heavy particle. This length (free path) is inversely proportional to the total particle density, n, of the gas, which is proportional to the gas pressure. The energy acquired by the electron is proportional to the product of the field and free path length. Thus the relationship E/n or the reduced electric field strength, is the physical variable, which can be used as a measure for the average electron energy.

Fig. 2.2 [21] shows on the left hand side the connection between the reduced field E/n and the mean electron energy in xenon.

The formation of excimers by electron collision is basically described by:

$$e + RG \rightarrow e + RG^{*} \tag{2.1}$$

$$RG^{*} + RG + RG \rightarrow RG_2^{*} + RG \tag{2.2}$$

The three body collision is favored with higher pressures.

The excimer molecule is not very stable, decomposing within just a few nanoseconds to give up its excitation energy in the form of a UV photon.

$$RG_2^{*} \rightarrow 2RG + h\nu \tag{2.3}$$

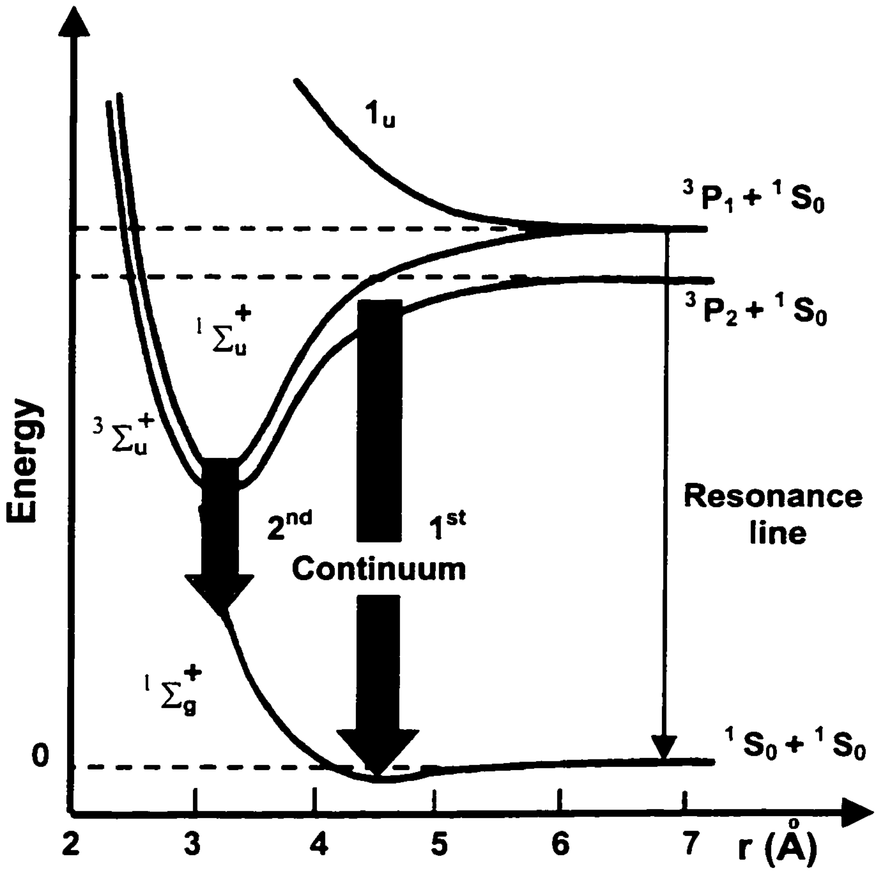

FIG. 2.1. Part of the potential energy diagram of xenon and corresponding Excimer emission [21].

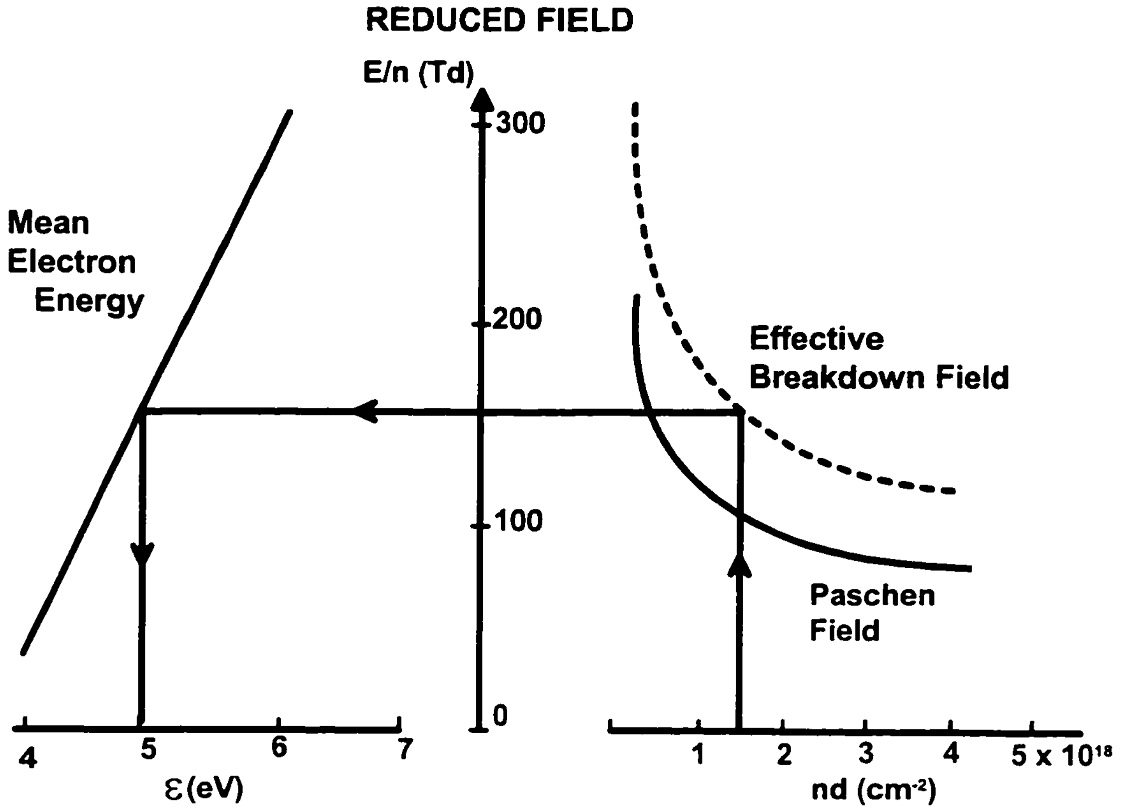

FIG. 2.2. Relation between mean energy of the electrons, reduced electric field E/n and the product of particle density n times gap spacing d for xenon [21].

This process is shown schematically in Fig. 2.3 [22].

In reality, higher lying excited states and ionic states are involved which is portrayed in Fig. 2.4 [5]. For better understanding excimers and to optimally generate them a detailed kinetic model for the excimer formation in rare gases will be explained in the following section.

2.2 Kinetic Model

Many papers devoted to the kinetics associated with the generation of rare gas excited states have been published during the last decade. The first kinetic model for rare gas excimer was formulated by Lorents [23]. Detailed application of this model with several improvements was made by Werner et al. [24]. Based on this model and different discussion of excimer formation, the mechanism for selectively populating the excimer levels can be viewed as a sequence of collisional energy exchange. While operating at high pressures allows for some simplification of the kinetic analysis (since collisions tend to vibrationally and electronically relax the population distributions to only a few states), these kinetics retain considerable complexity. The present understanding of these kinetics is incomplete and the relative importance of several collisional process remains controversial. In the following, a model based on different works [23-28] in excimer formation is discussed.

2.2.1 Production of the Excimer Precursors

Electrons with high energy are generated via gas discharges or e-beam. This high energy electrons ionize or excite the host gas in the reactions

$$e + RG \rightarrow RG^{*} + e \qquad (2.4)$$

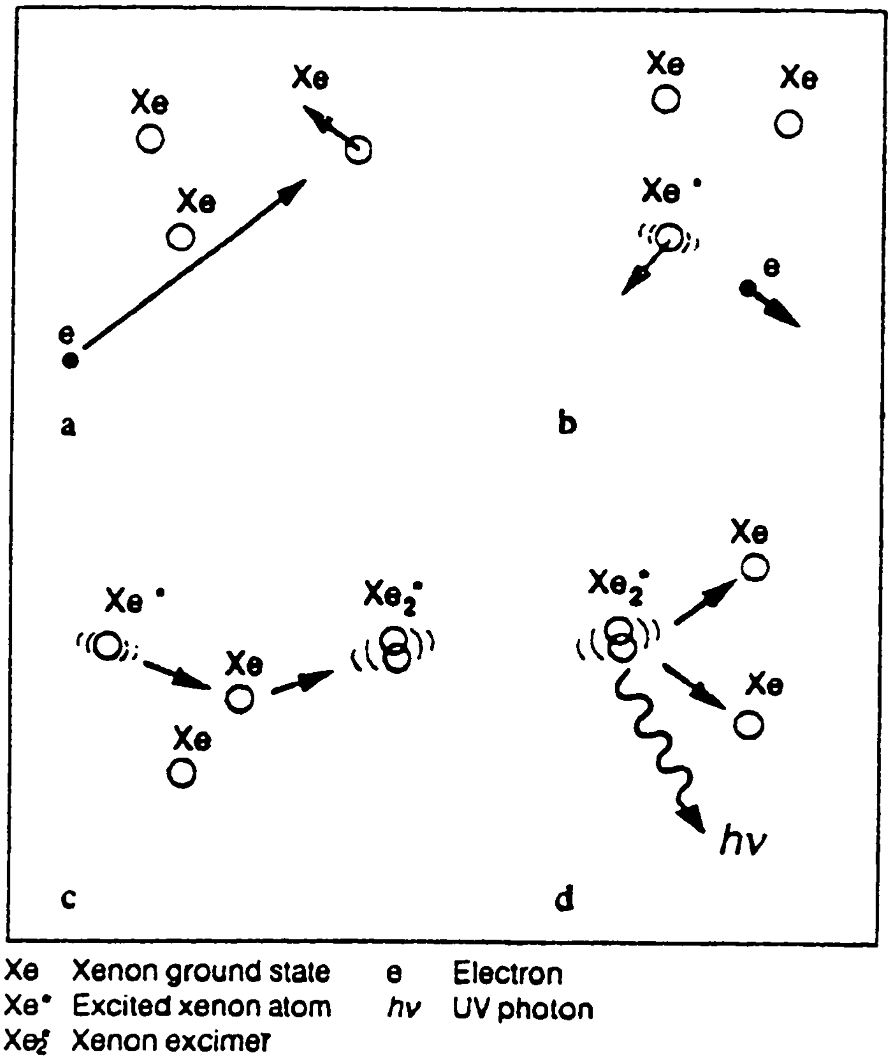

FIG. 2.3. Schematic of excimer formation [22].

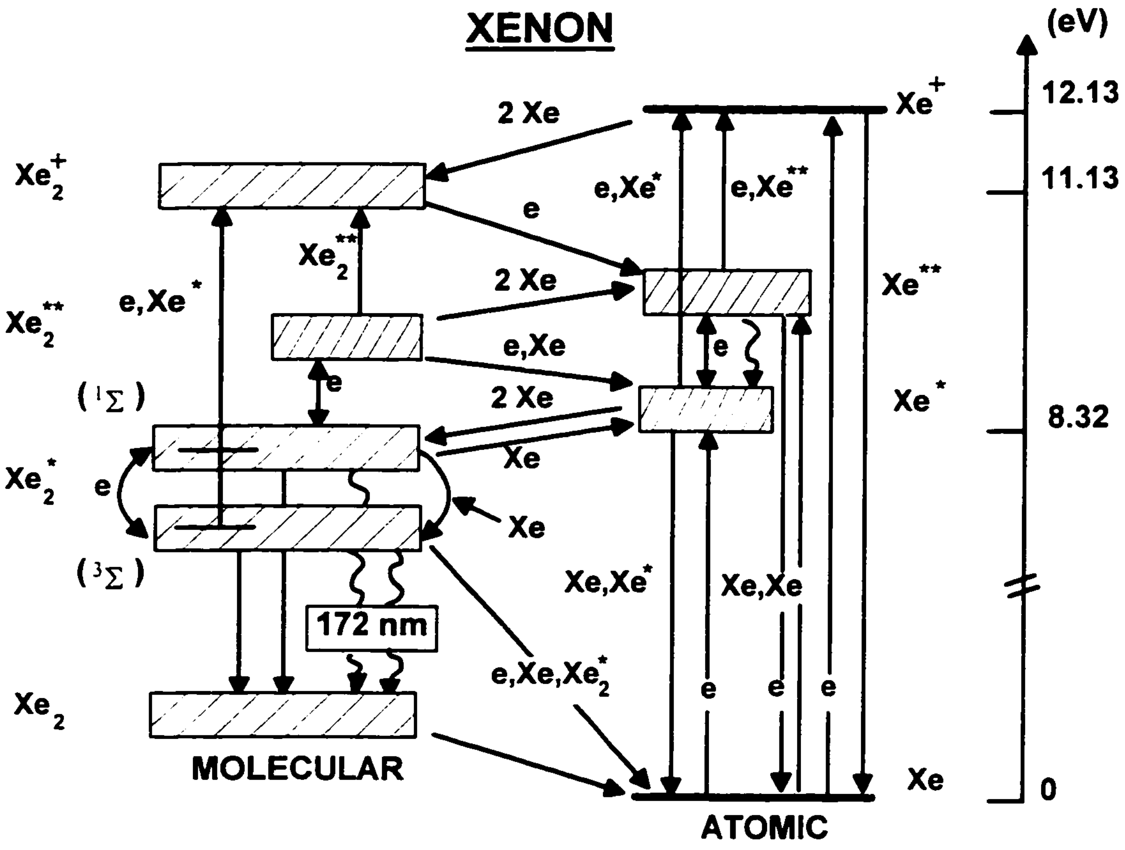

FIG. 2.4. Scheme of interactions between atomic and molecular xenon [5].

$$e + RG \rightarrow RG^{+} + 2e \qquad (2.5)$$

$$e + RG \rightarrow RG^{**} + e \qquad (2.6)$$

where RG is the rare gas atom, RG* is the rare gas excited states ($^3P_1$ & $^3P_2$ excited states), RG** is the higher lying states and RG^+ is the rare gas ion. The fractional conversion of electron energy to different species varies depending on the rare gas and on the excitation mechanism.

Excited rare gas atoms RG* are the precursors of the generation of excimer states. RG** and RG^+ will play a big role in populating the RG* state. At low pressures the dominant loss mechanism of the atomic ion RG^+ is collisional radiative recombination. At high pressures, however, the dominant loss mechanism for the atomic ion involves the formation of a diatomic molecular ion, via three body collisions:

$$RG^{+} + RG + RG \rightarrow RG_2^{+} + RG \qquad (2.7)$$

where the third body is necessary to remove the binding energy of the molecule.

Once formed, the diatomic ion may participate in two major loss processes. The first one involves direct electron capture followed by dissociation to a ground state and any number of excited atomic species. This process, namely dissociative recombination DR, may be presented by the reaction:

$$e + RG_2^{+} \rightarrow RG + RG^{**} \qquad (2.8)$$

A second loss process for the diatomic ion involves cluster ion formation via three body collisions with ground state atoms:

$$RG_2^{+} + RG + RG \rightarrow RG_3^{+} + RG \qquad (2.9)$$

As with the diatomic ion, cluster ions may be lost by DR process similar to reaction 2.8.

The RG** atoms relax via the reactions

$$RG^{**} + 2RG \rightarrow RG_2^{**} + RG, \qquad (2.10)$$

$$RG_2^{**} + (RG) \rightarrow RG^{*} + RG + (RG) \qquad (2.11)$$

to the RG* state, which is the precursor for the formation of the excimer state. Reaction 2.11 may proceed by means of spontaneous predissociation due to molecular curve crossings or by collisionally enhanced predissociation.

2.2.2 Excimer Formation

The process of three particle conversion of the excited atoms RG* into diatomic molecules

$$RG(^3P_1) + 2RG \rightarrow RG_2^{*}(^1\Sigma, v >> 0) + RG \qquad (2.12)$$

$$RG(^3P_2) + 2RG \rightarrow RG_2^{*}(^3\Sigma, v >> 0) + RG \qquad (2.13)$$

is the principal process producing diatomic molecules in the upper vibrational states. In order to efficiently generate excimers this process should be faster than the resonance radiative decay of the RG* states, which is the dominant process at low pressure.

$$RG^{*} \rightarrow RG + h\nu_0 \qquad (2.14)$$

where $h\nu_0$ is the resonance radiation

If the vibrational relaxation

$$RG_2^{*}(^1\Sigma, v >> 0) + RG \rightarrow RG(^1\Sigma, v \approx 0) + RG \qquad (2.15)$$

$$RG_2^{*}(^3\Sigma, v >> 0) + RG \rightarrow RG(^3\Sigma, v \approx 0) + RG \qquad (2.16)$$

is low, the molecules formed actively emit from the upper vibrational levels

$$RG_2^*({}^1\Sigma, v >> 0) \rightarrow 2RG + h\nu_1 \quad (2.17)$$

$$RG_2^*({}^3\Sigma, v >> 0) \rightarrow 2RG + h\nu_1 \quad (2.18)$$

where $h\nu_1$ is the first continuum radiation energy.

As the gas pressure increases, the vibrational relaxation rate grows, and process 2.12 and 2.13, to a greater extent, are followed by population redistribution to lower vibrational levels and by longer wavelength emission (second continuum)

$$RG_2^*({}^1\Sigma, v \approx 0) \rightarrow 2RG + h\nu_2 \quad (2.19)$$

$$RG_2^*({}^3\Sigma, v \approx 0) \rightarrow 2RG + h\nu_2 \quad (2.20)$$

where $h\nu_2$ is the second continuum radiation energy.

2.2.3 Excimer Decay Mechanism and Loss Processes

Although the radiative lifetimes of these two states ${}^1\Sigma_U^+(O_U^+)$,${}^3\Sigma_U^+(1_U, O_U^-)$ are appreciably different, both contribute to the fluorescence observations. A summary of lifetime data taken from the review of Lorentz is shown in table 2.2.

The inverse of the decay time can be found, for a complete population equilibrium between the triplet and singlet excimer states, from [29]

$$\frac{1}{\tau} = \frac{3}{4} \cdot \frac{1}{\tau_3} + \frac{1}{4} \cdot \frac{1}{\tau_1} \quad (2.21)$$

where ¾ and ¼ are the fractional populations of the triplet and singlet populations and τ_3 and τ_1 are the triplet and singlet lifetimes. Electrons are an important factor in establishing this equilibrium. In the presence of hot plasma electrons, the excimer states as well as their precursors will rapidly be mixed in reactions of the type

$$e + RG_2^\bullet(^3\Sigma) \rightarrow e + RG_2^\bullet(^1\Sigma) \tag{2.22}$$

For electron densities of 10^{15} cm^{-3}, super elastic electron collisions can also enhance electronic relaxation in both the atomic and excimer manifolds. The super elastic mechanism, however, can also destroy excimers by causing transitions to the ground state.

Table 2.2. Radiative lifetimes of excimer states

Excimer	$^1\Sigma_U$ **(ns)**	$^3\Sigma_U$ **(μs)**	**Ref.**
Ne_2^*	-	5.1	30
	2.8	11.9	31
	-	12 ± 6	32
	-	6.62	33
Ar_2^*	-	2.8	34
	-	3.7	35
	4.2 ± 0.13	3.2 ± 0.3	36
	-	4.0 ± 2.0	32
	-	3.22	33
Kr_2^*	-	1.7	35
	-	0.3	37
	-	0.36 ± 0.16	32
	-	0.35	33
Xe_2^*	5.5 ± 1.0	0.09 ± 0.05	36
	-	0.10 ± 0.05	32
	-	0.140 ± 0.45	32

An important loss mechanism of the excimer states involves photoionization by the generated UV photon. Such processes are energetically allowed, since the ionization potentials of the singlet and triplet are much less than the energy of the emitted photons.

The excited excimers species may also participate in destructive process of the form

$$RG_2^{\bullet} + e \rightarrow RG_2^{+} + 2e \qquad (2.23)$$

$$RG_2^{\bullet} + RG_2^{\bullet} \rightarrow RG_2^{+} + 2RG + e \qquad (2.24)$$

The former representing ionization by electron impact and the latter by Penning ionization. The Penning process represents a significant loss mechanism at high excimer densities.

An additional loss process that play an important role specially with increasing temperature is the quenching of excimers by neutral atoms

$$RG_2^{\bullet} + RG \rightarrow RG^{\bullet} + 2RG \qquad (2.25)$$

CHAPTER III

EXCIMER GENERATION MECHANISMS

The formation of excited excimer complexes has been extensively investigated. The necessary precursors for excimer formation, which can be excited atomic or molecular species as well as ions, can be generated by radiation (γ-rays, X-rays) by particle beams (electrons, protons, α particles) or by various types of gas discharges.

For basic research studies, excimer formation by electron beams or beams of other energetic particles is widely used. Accelerators, which can provide high particle energy, are bulky devices impractical for use in the design of a lamp. Discharges are potentially more efficient and powerful, and are simple to construct in small size.

3.1 Gas Discharges Excimer Formation

Basically, in rare gas discharges the low energy electrons suffer only elastic encounters with the rare gas atoms, in which they lose very little energy. Thus, as they move along the electric field they increase in energy until they reach the threshold for excitation of the first excited state of the rare gas atoms. Above this energy they experience inelastic collisions in which the rare gas atom is left in an excited state while the electron returns to a low energy.

For efficient excimer formation certain requirements have to be fulfilled. First of all, electrons of a suitable energy distribution are needed to create the necessary precursors by electron impact. A sufficient number of electrons in the high energy tail of the energy distribution is required. Secondly, the pressure has to be high enough for the three body reactions to occur faster than any decay or quenching processes that can deactivate the excited precursors. In practice [5], electron energies of about 10 eV and pressures of the order of 0.1-1 bar are required, conditions that can be met only in non-thermal discharges.

3.2 Non-thermal Plasmas

If energy is supplied to a plasma by applying a potential difference across it, the electric field will act upon the charged particles and impart energy to them. The electrons due to their light mass are immediately accelerated to higher velocities than the heavier ions in the time available between collisions. If the pressure is small enough or the field is high enough, the electrons and partly the ions will, on the average, have a kinetic energy, which is higher than the energy corresponding to the random motion of the molecules or atoms [38]. In this case, the plasma is non-thermal.

A very important parameter for all non-thermal plasma is the reduced field E/n; i.e., the electric field divided by the neutral gas density n. In discharge physics, this parameter has its unit “Townsend” (Td). 1 Td equals 10^{-17} V cm^2. The reduced field determines the electron energy in a plasma.

The reduced field also determines whether a plasma is thermal or not. Only for a very low E/n values (< 1 Td) does the electron energy come close to the kinetic energy of the heavy particles and thermal equilibrium can be expected.

The inherent advantage of non-thermal discharges over thermal discharges is the following: if one wants to excite only a small fraction of the gas atoms or molecules, only a non-thermal discharge can provide electrons or ions at the right energy. The bulk of the gas is more or less left untouched and the losses are thus kept at a minimum.

3.3 Generation of Excimers Using Non-thermal Discharges

Different discharges have been used to generate excimers including DC corona discharges [39], microwave discharges [40-41], supersonic discharges [42-43] and cooled capillary discharges [44]. However, the use of these discharges as excimer lamps is still in the experimental phase. To our knowledge the only used discharge in the excimer lamp industry is the silent discharge. The radiation produced from these discharges is not only used in VUV lamps but also in mercury free fluorescent lamps and plasma displays. Excimer lamps based on silent discharges have been commercially available several years ago in Germany, Japan and USA. Flat panel from these lamps will be introduced in the market for the first time by the end of this year (1998)[9]. In the following silent discharges will be described in details with a quick review of some examples from the other methods of excimer generation.

3.3.1 Silent Discharge

The silent discharge (dielectric barrier discharge) is a high-pressure non-thermal discharge. The discharge is characterized by the presence of at least one dielectric barrier in the current path between the electrodes and the discharge space. The barriers may consist, for example, of one or more glass layers, positioned up against one of the electrodes.

Since the current can pass the dielectric only in the form of a displacement current, it always requires a changing electric field to support it. Silent discharges are generally operated with alternating voltages. The charge, which accumulates on the dielectric during a half wave of this voltage is neutralized during the next half wave by charge carriers of opposite polarity. There is no charging of the dielectric when averaged over the time.

Although silent discharges can be operated over a wide pressure and frequency range, its typical applications require relatively high pressures (0.1-10 bar) and relatively low frequencies (50 Hz-1 MHz) with a voltage of few kV. As a matter of fact, it has been regarded as their main advantage that they provide an efficient and simple means of maintaining a non-thermal plasma at line frequency and atmospheric pressure.

3.3.1.1 Theory of silent discharge formation

At high pressures, the discharge develops into a multitude of randomly distributed microdischarges of nanosecond duration. Each microdischarge consists of a thin cylindrical current filament which spreads into a surface discharge at the dielectric [Fig. 3.1 [10]]. The plasma columns of the microdischarges can be characterized as high-pressure transient glow discharges. Excimer formation takes place exclusively in these microdischarges. Both the diameter and the duration depend on the gas and the pressure. The current flows entirely within the filaments. The exchange of energy between the accelerated electrons and the atoms and molecules occurs within the microdischarges.

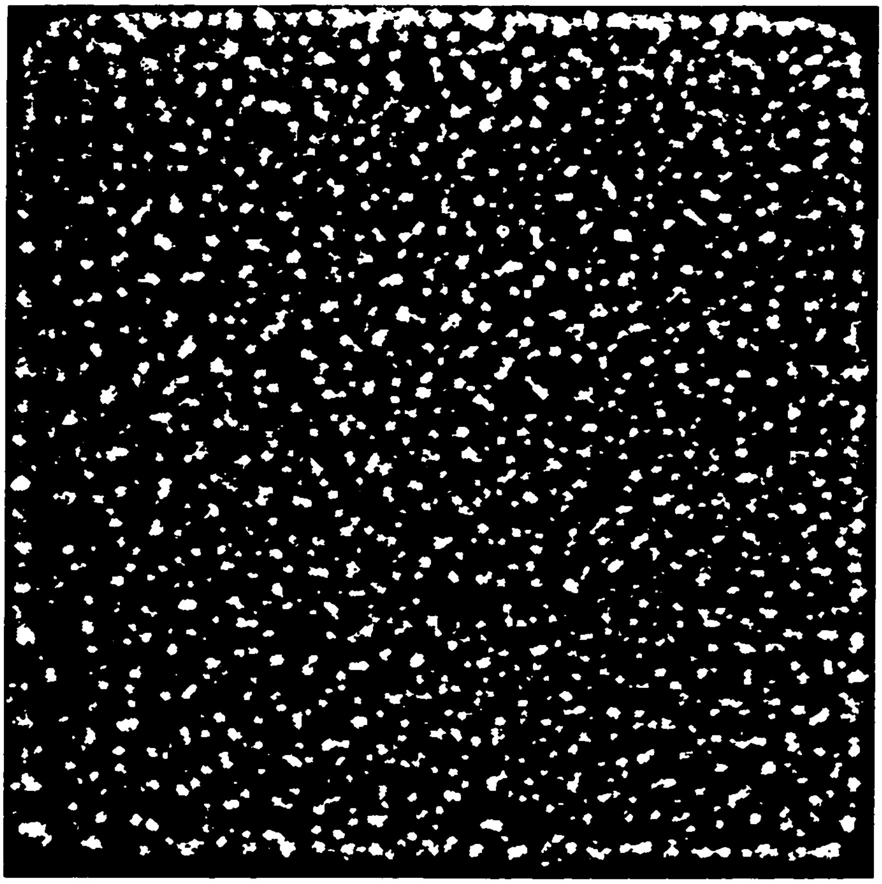

FIG. 3.1. Photograph of microdischarges in silent discharge [10].

The energetic electrons (some eV) excite the atoms and molecules and thus transform some of their kinetic energy into energy stored in the excited species. Due to the high electron energy, this energy exchange can be very efficient. It is not unusual that 90% of the kinetic energy or more is transformed into stored energy. Elastic losses are therefore very low, and initially very little energy is lost as heat. At lower pressures the diameters of the filaments increase and tend to become more numerous and the overall appearance is more diffuse. As the pressure is further lowered, there is a continuous transition from the filamentary structure of the silent discharge to the more diffuse appearance of the glow discharge.

3.3.1.2 Silent discharge characteristics

A great advantage, of the silent discharge over many other discharge types is that the average energy of the electrons can be influenced by changing the effective reduced electric field E/n [21]. It is mainly a function of the breakdown condition and, to some extent, depends also on the choking condition which is influenced by the properties of the dielectric. Breakdown in a gap bordered by dielectric barriers is determined practically by the same condition as between metal electrodes. It is given by the well-known Paschen relation stating that: for a given gas the stationary breakdown voltage in a homogeneous electric field depends only on the product of pressure p and gap spacing d. In a slightly more sophisticated way it can be stated that: the reduced field at breakdown and consequently the mean electron energy $<\varepsilon>$ depend on the product nd. Lowering either n or d causes an increase in E/n and $<\varepsilon>$.

High current densities in the filament in the range 100-1000 A/cm^2 are another important feature of silent discharges. This high current densities and the thin microdischarge channels depend to some extent on the gas properties but are mainly a consequence of the high pressure and the corresponding gas density n. By lowering the density the channel radius increases proportional to 1/n and more homogeneous discharges are obtained.

The third important parameter is the charge transported in an individual microdischarge. This charge depends on the gap spacing and on the thickness and permittivity ε_r of the dielectric barrier. For a given dielectric the charge Q is proportional to the gap spacing and practically independent of the pressure. For a fixed gap spacing, Q is essentially proportional to the capacitance of the dielectric barrier.

3.3.1.3 Microdischarges

Understanding the microdischarges [45] is the key to understand the silent discharge. Therefore it is very important to understand their physics; i.e. the electrical breakdown and their chemistry; the reaction of the excited species generated. Fig. 3.2 [45] shows a schematic illustration of the life cycle of one such filament. This figure shows how the initial electron current j_e (t) excites the species A (RG*). These excited species in turn react to form the products B (RG_2^*). Each process has its own life cycle and duration. The duration of these steps is of different orders of magnitude. The local breakdown is usually completed within second and the chemistry can last from nanoseconds to seconds.

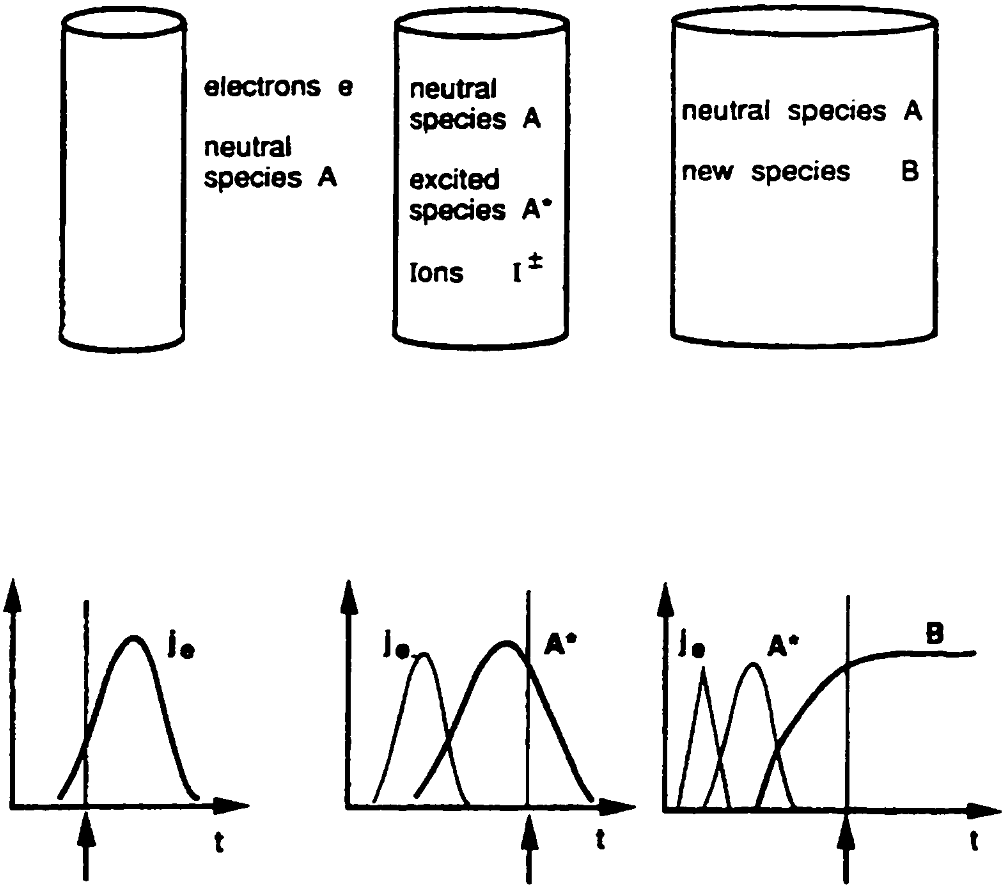

FIG. 3.2. The life cycle of one microdischarge in silent discharges [45].

For typical discharges at pressures of the order of 1 bar and gap spacing of the order 1 mm the main microdischarge properties are shown in table 3.1 [10]. It can be concluded from this table that each microdischarge column stays in the state of a weakly ionized plasma with a high electric field on the order of the breakdown field and correspondingly high electron energies. The kinetic temperature of the heavy particles (atoms, molecules, and ions) on the other hand stays close to room temperature, a typical situation for a non-thermal plasma. Most of the energy transferred to the electrons by the high electric field can be utilized for excitation, ionization and dissociation processes in order to initiate the desired plasma chemical reactions.

Table 3.1. Characteristic microdischarge properties in silent discharges.

Characteristic	Typical Values
Duration	1-10 ns
Filament radius	about 0.1 mm
Transported charge	100-1000 pC
Current density	100-1000A/cm^2
Electron density	10^{14}-10^{15} cm^{-3}
Mean electron energy	1-10 eV
Gas temperature	Close to average gas temperature

3.3.1.4 Excimer lamps based on silent discharges

A typical excimer lamp discharge configuration is shown in Fig. 3.3 [6]. A round stainless steel plate forms the ground electrode. Its temperature could be kept constant by a thermostat-controlled water circuit (not shown). A quartz plate

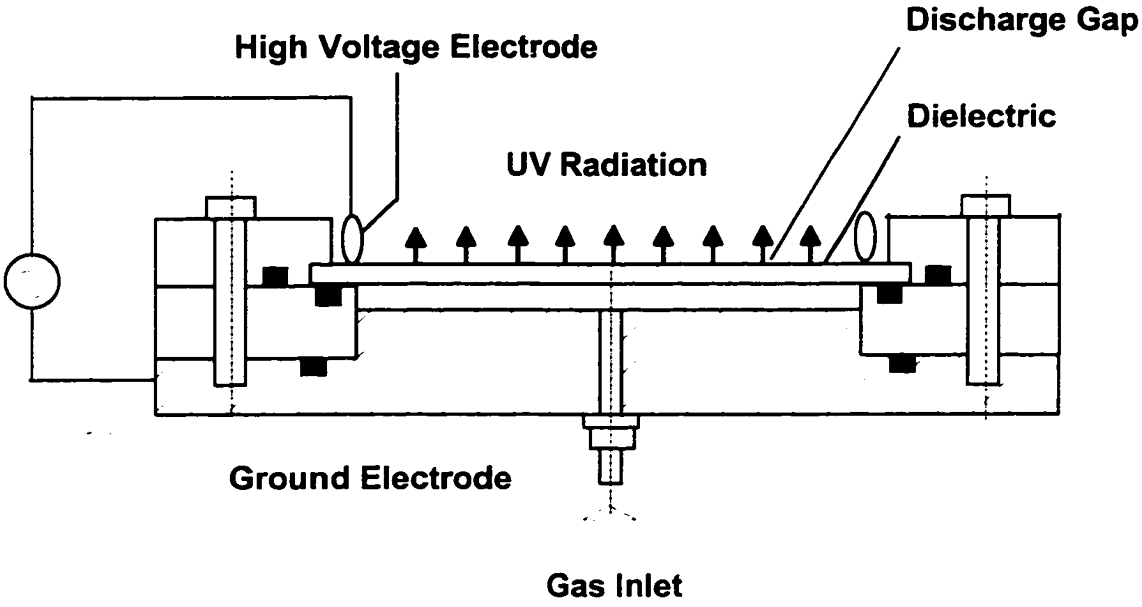

FIG. 3.3. Silent discharge excimer lamp [6].

of 10 cm diameter and 3mm thickness serves as a dielectric barrier. Since, the high voltage electrode has to be transparent to the UV radiation it is made of a fine wire mesh mounted in a metal ring.

A large variety of excimer forming mixtures has successfully been tried in dielectric barrier discharges. Fig. 3.4 shows representative excimer lamp spectra all of which show extremely clean spectra with narrow band excimer emission in only one wavelength region.

Modeling of these discharges [45] indicates that this excimer emission can reach an efficiency of 40-50%. Fig. 3.5 shows computation of the efficiency for different assumed electron densities at 1 bar and the pressure dependence of the different emission features neglecting radiation trapping of the resonance line. In a practical device typically 5-15% of the discharge power can be converted to UV or VUV radiation.

3.3.2 Other Mechanisms of Excimer Generation

3.3.2.1 Microwave discharge

In the microwave region (0.3-10 GHz) the wavelength of the electromagnetic field becomes comparable to the dimensions of the discharge vessel, which necessitates other coupling mechanisms. Most microwave induced plasmas are produced in a waveguide structure or resonant cavity. As the dimensions of the cavities diminish when the frequency increases, the maximum microwave frequencies used for discharge applications are usually below 3 GHz. A very common frequency is 2.45 GHz, which is also used in microwave ovens.

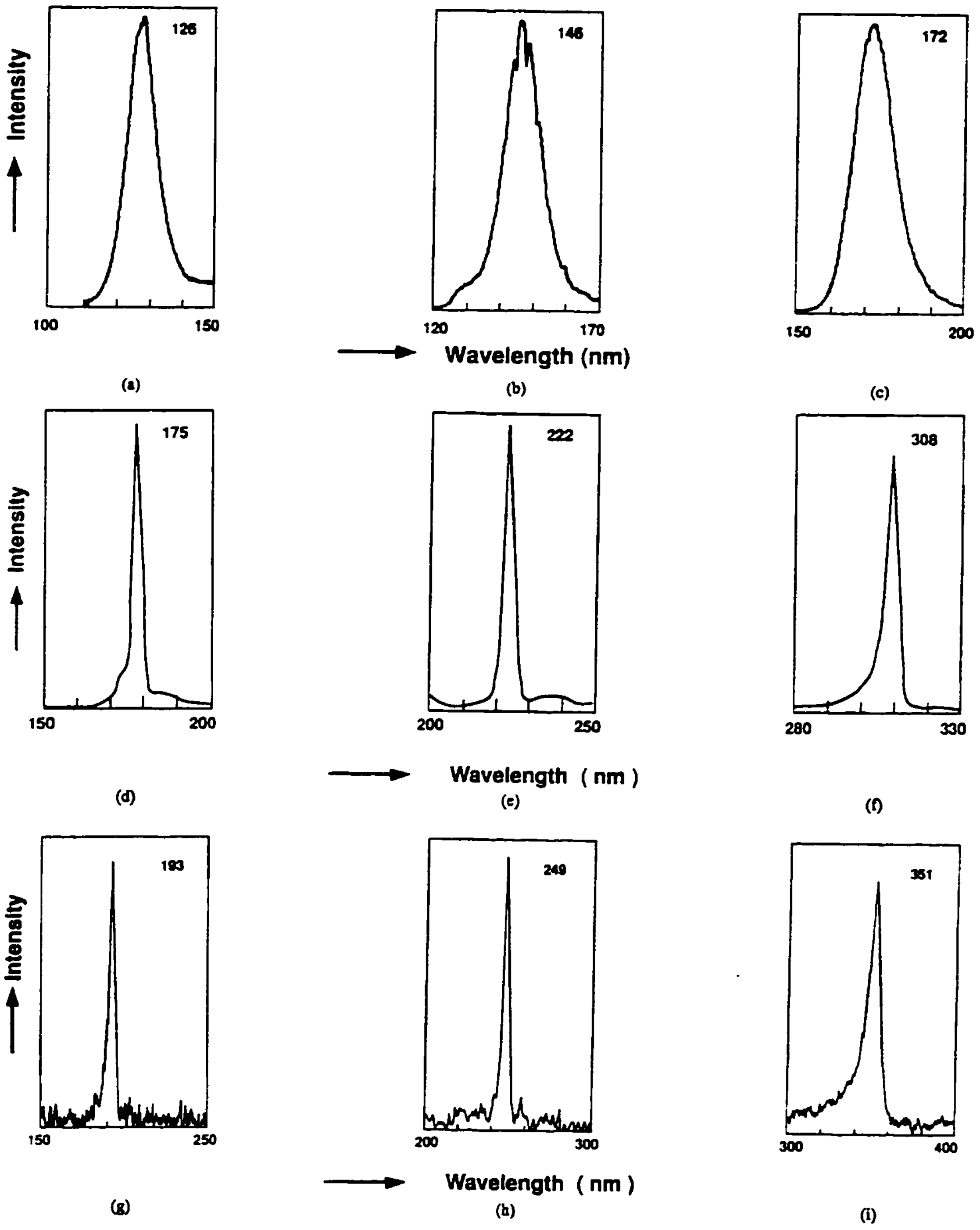

FIG. 3.4. Emission spectra of different silent discharge excimer lamps [6]
a-Argon b- Krypton c- Xenon
d- ArCl* e- KrCl* f- XeCl*
g- ArF* h-KrF* i- XeF*

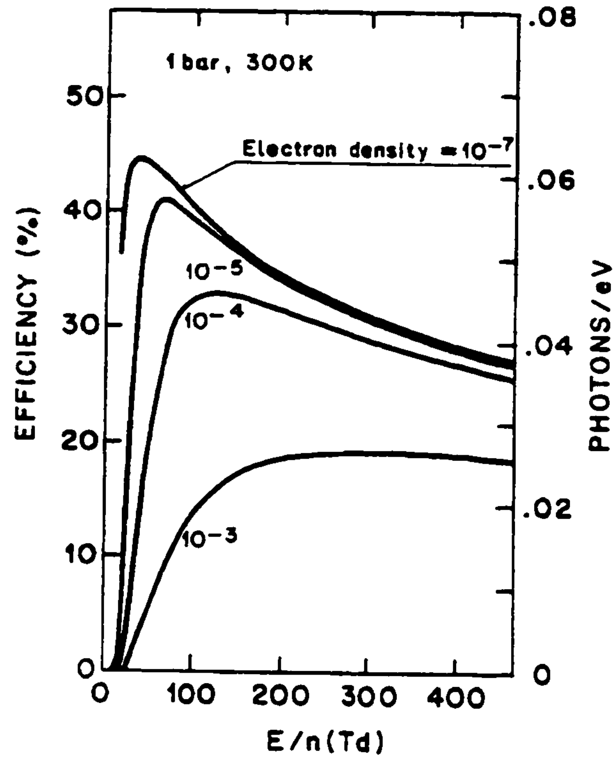

FIG. 3.5. (a) Calculated efficiency of VUV generation of silent discharges in xenon as a function of the reduced field E/n [45].

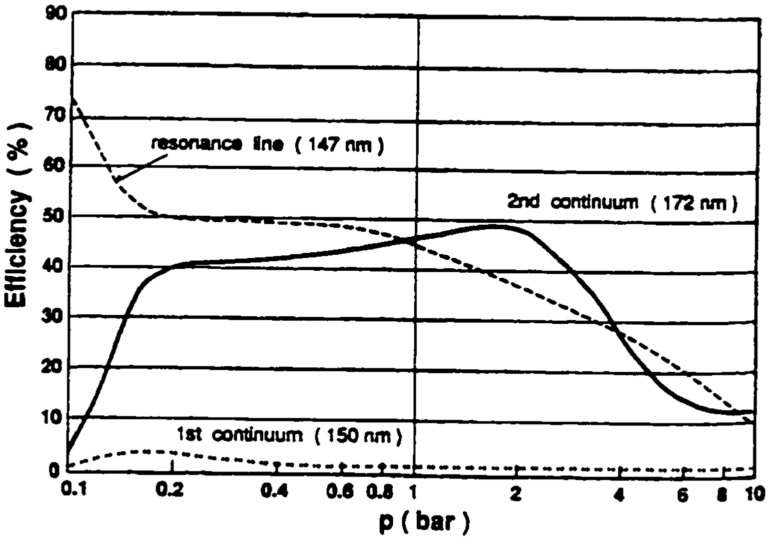

FIG. 3.5. (b) Calculated efficiencies of the three emission features of silent discharges in xenon as a function of pressure [45].

Since at these frequencies only the light electrons can follow the oscillations of the electric field, microwave plasmas are normally far from local thermodynamic equilibrium. They can be operated in a wide pressure range, starting from below 1 mbar to about atmospheric pressure. These discharges can produce large volume non-thermal plasmas of reasonable homogeneity.

Table 3.2. Specifications of the microwave excimer lamp.

Lamp size	Length	250
	Diameter	8
Radiation window size		100 x 250
Focused area		10 x 200
Microwave frequency	Continuous	2.45 GHz
	Pulse	3.05 GHz
Average microwave power	Continuous	0.6-10 kW[a]
	Pulse	70 kW
Pulsed microwave power	Peak power	35 kW
	Pulse width	1.2 μs
	Pulse frequency	1 kHz
Dimensions	Lamp house	276(w) x 150(h) x 460(d)
	Power supply	440(w) x 200(h) x 630(d)
Weight	Lamp house	14 Kg
	Power supply	50 Kg
Power requirement		AC 200 V(3ϕ),13 A
Cooling system		Forced air

[a] Full wave rectified average

All dimensions are in mm

The excimer lamp [46] is composed of a power supply unit, a ventilation unit and a lamp house containing two microwave generators and a discharge tube. The microwave power generated by two magnetrons is fed to a microwave cavity through waveguides and coupling antennas. The discharge tube is a sealed fused quartz containing excimer gas and air cooled during operation.

Reported conversion efficiencies from electrical power to optical power are from 0.5 to 2%. Table 3.2 shows the specification of the lamp system.

3.3.2.2 Jet discharge

In order to avoid the high pressure operation in discharges a new excimer production kinetics was proposed [42]. Rare gas excimers are produced by direct excitation of rare gas clusters (especially dimers). If sufficient rare gas clusters are prepared prior to the discharge, efficient excimer production will be possible. Clusters are generated in an adiabatically expanding gas, which was achieved by injecting a gas through a nozzle into a vacuum chamber (Fig. 3.6).

The excimer emission is strongly related to the cluster production. Changing supersonic jet parameters, such as the stagnation pressure and gas injection time, as well as the nozzle shape can control the intensity and pulse width of the excimer emission. The number density and size of clusters depend significantly on the nozzle shape and the stagnation pressure, which affect the characteristics of the excimer emission in a pulsed jet discharge. More than 70% of the clusters produced are dimers (n=2). These dimers play a big role, in addition to the three body collisions, in the formation of excimer molecules. These dimers can lead to excimer generation by either electron impact or excitation by excited rare gas as follows:

$$e + RG_2 \rightarrow RG_2^{*} + e \tag{3.1}$$

$$RG^{*} + RG_2 \rightarrow RG_2^{*} + RG \tag{3.2}$$

By using conical nozzle, a peak output power of 1.5 W at 174 nm in xenon was obtained with a power conversion efficiency of 3%.

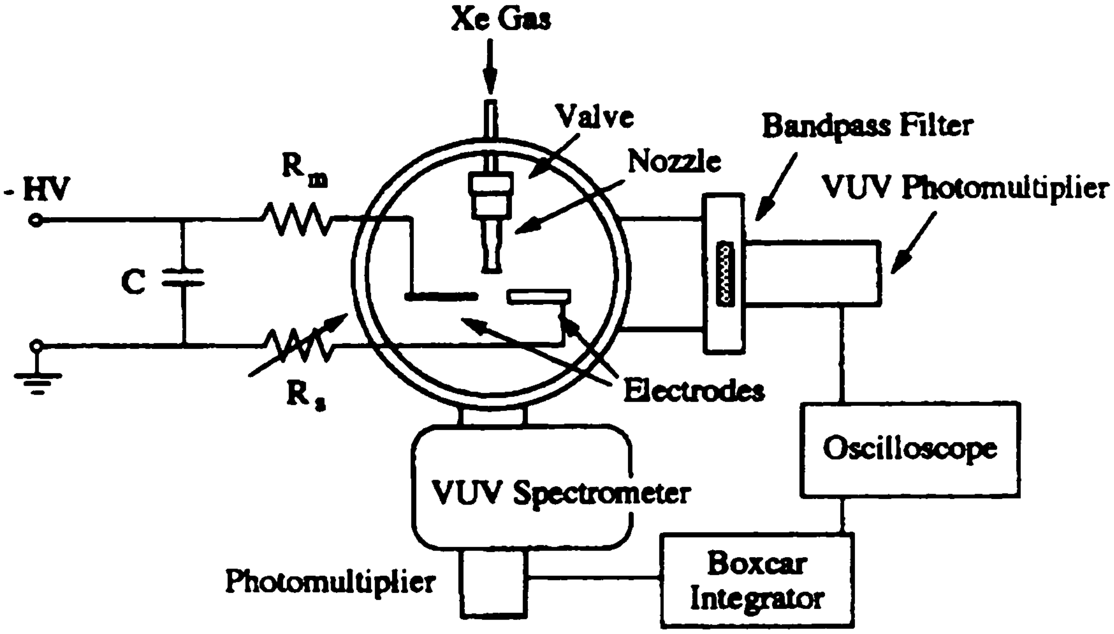

FIG. 3.6. Jet discharge excimer generation [42].

CHAPTER IV

MICROHOLLOW CATHODE DISCHARGES

Hollow cathode discharges (HCD) have been studied for many years, mainly for spectroscopic and laser purposes. Recently, there has been renewed interest in the HCDs. An example for the successful research on hollow cathode discharges is the invention and development of the so called Pseudospark, a transient high current discharge which evolves from a hollow cathode discharge.

The miniaturization of hollow cathode discharge geometries has been pursued mainly in the United States of America. A first study on discharge in submillimeter hollow cathodes has been published by White in 1969 [47]. The research group in the electrical department at Old Dominion University has, in the past four years reduced the dimensions of hollow cathodes, with the goal to expand the pressure range of hollow cathode discharges to atmospheric pressure.

4.1 Hollow Cathode Effect

If a plane cathode in a glow discharge is replaced with a cathode with a hollow structure, the negative glow may be found to be inside the hollow structure [48]. Such structure may be either cylindrical or slit shaped hole (Fig. 4.1). The anode may be arbitrarily shaped. In a specific range of operating conditions the negative glow is found to be inside the hollow structure of the cathode. Under such conditions, at a constant current the voltage is found to be lower and, at a constant voltage, the current is found to be orders of magnitude larger than for the plane cathode. This effect is called "Hollow cathode effect".

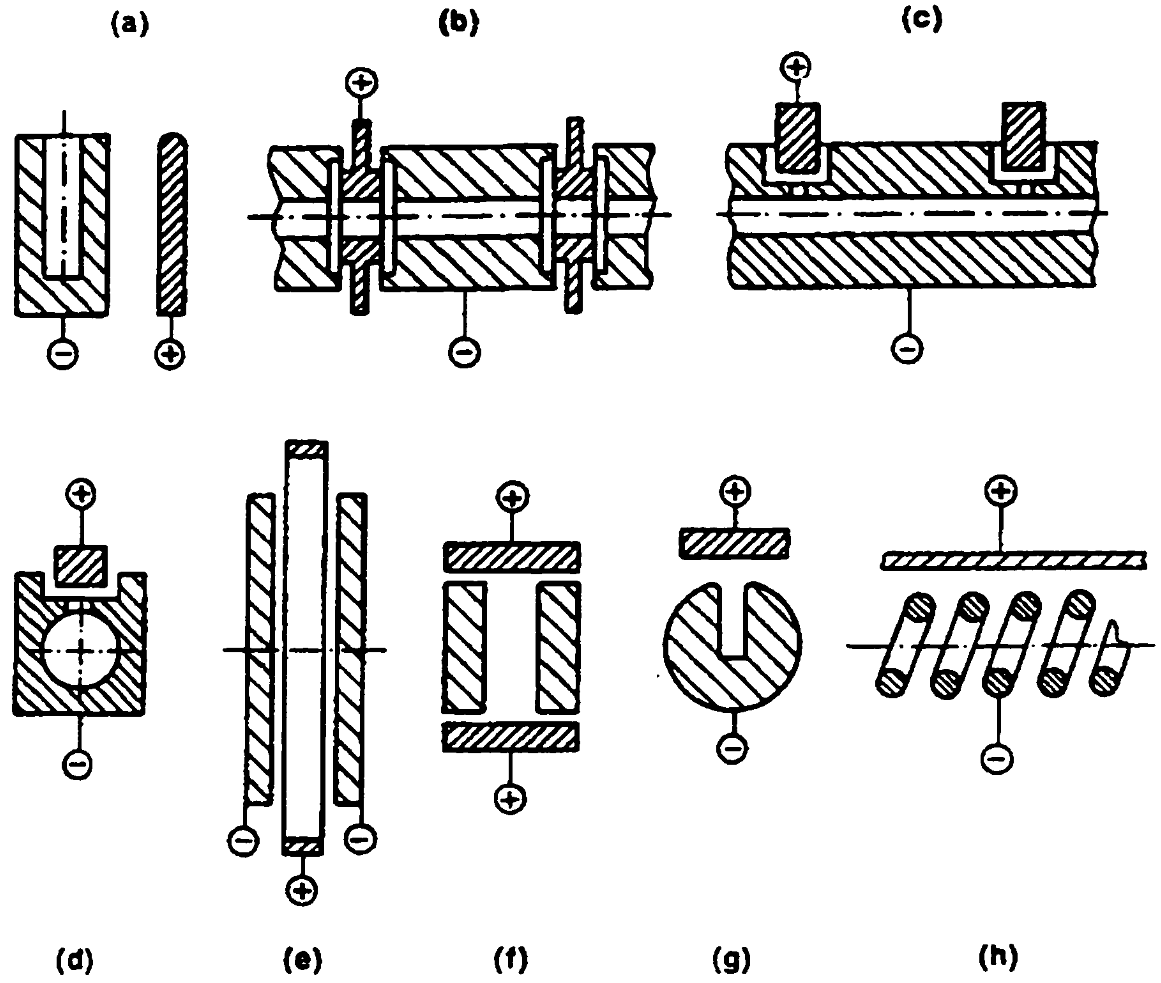

FIG. 4.1. Some typical hollow cathode geometries: a-, b-, c- cylindrical; d- spherical; e-, f- parallel plate; g- slit; h- helical [48].

The current density in hollow cathode discharges exceeds that of linear discharges by orders of magnitude for comparable discharge voltages. The main mechanism responsible for this current enhancement is assumed to be the "Pendel effect".

With sustaining voltages close to the breakdown voltage the current is significantly low and space charges will have a negligible effect on the electric field distribution (Vacuum field). This phase is similar to a Townsend discharge. Successive avalanches initiated by secondary electrons emitted from the inside surfaces of the hollow cathode by ion impact contribute to the buildup of the ion density. During this phase the geometrical field dominates over the space charge field. A sketch of the discharge in this phase is shown in Fig. 4.2a. It is assumed here that the pressure, p, times the electrode gap, d, is on the left-hand side of the Paschen minimum. The discharge therefore develops along the longer path between the anode and the outer face of the cathode to push itself to the minimum of the curve.

Increasing the voltage with constant pressure increases the current and subsequently causes the formation of space charges, which will affect the electric field distribution. A positive space charge will first be generated in the vicinity of the anode. With increasing voltages this space charge formation will occur closer and closer to the cathode. A virtual anode (positive column) is formed which eventually moves into the cathode hole. When the virtual anode enters the cathode hole, the electric field in the cathode plane assumes a strong radial component (cathode fall). Electrons emitted from the cathode through ion impact

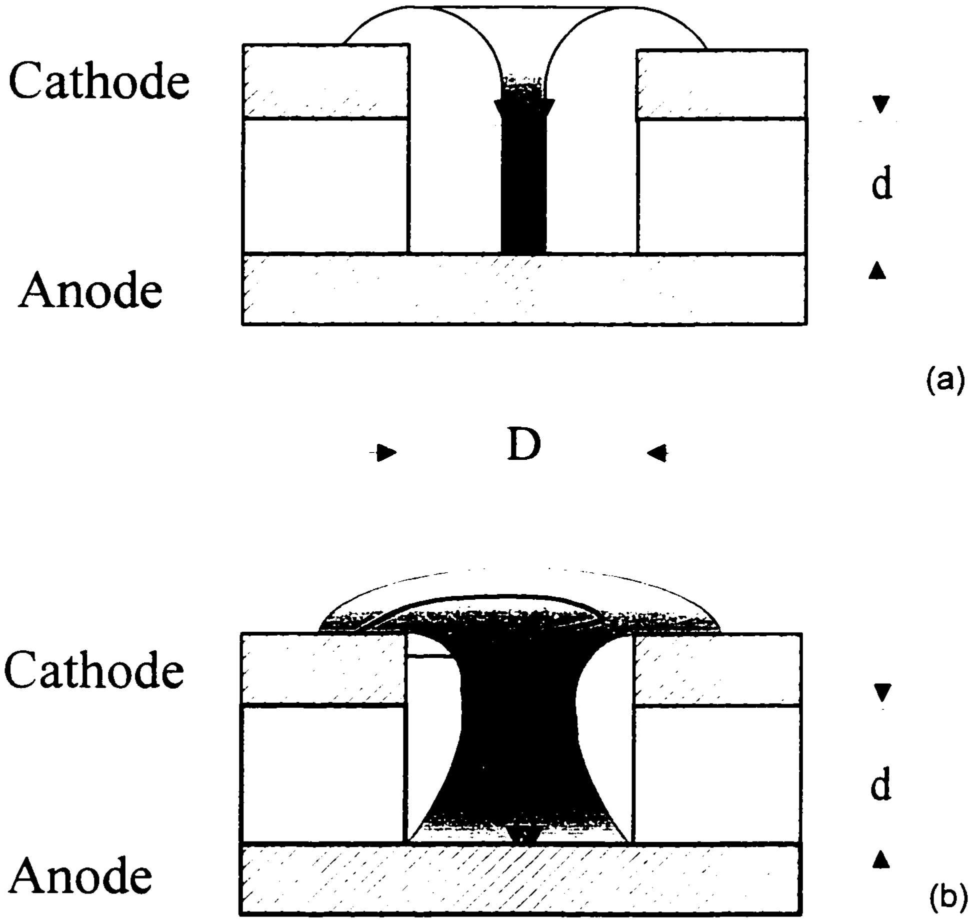

FIG. 4.2. Different discharge modes: a- Townsend discharge b- Hollow Cathode discharge.

will be accelerated radially towards the axis. Since the mean free path is on the order of the hole dimensions, they have the opportunity to pass through the axis region into the opposite cathode fall and then oscillate back and forth through the center, causing the sustainment of a plasma (virtual anode) on the axis. This effect which is called the "Pendel effect" is shown in Fig. 4.2b.

4.1.1 Different Mechanisms Responsible for the Hollow Cathode Effect

A systematic study and complete understanding of hollow cathode discharges does not exist at this time although a very large number of papers have appeared. One reason is that most experimental investigations have been carried out over a narrow range of operating parameters. Another reason is that it is difficult to compare the results obtained with different hollow cathode designs with respect to geometry, dimensions, material etc. operated with different gases and in different pressure ranges.

There are several mechanisms contributing to the hollow cathode effect:

1. Electrons emitted from the cathode surface inside the hollow structure, which are accelerated in the cathode fall mainly contribute to ionization in the negative glow. Those electrons which have crossed the negative glow without significant energy loss will be reflected at the opposite cathode (pendular electrons) and change the potential distribution of the cathode fall. These electrons also contribute to a further enhanced ionization rate in the negative glow. This effect significantly influences the electron energy distribution function in the hollow cathode plasma [49].

2. The cathode fall in a hollow cathode under high current density conditions can be significantly thinner than for a plane cathode, reducing the probability for charge transfer collisions. Therefore the average ion velocity at the cathode surface is increased, causing an increased secondary electron emission rate.
3. Neutral, energetic particles (metastables and photons) generated in the negative glow inside the hollow cathode have a much higher probability of hitting the surface of the cathode due to the hollow geometry, increasing the electron emission rate of the cathode [50]. Also more positive ions are lost in the negative glow of a planar electrode since the negative glow is essentially field free and the ion transport is dominated by diffusion [51].
4. The higher plasma density inside the hollow cathode makes multistep processes more likely [51]. Multi-step processes, known as cumulative ionization processes, contribute in the rise of discharge efficiency together with other mechanism.
5. The confined structure of the hollow cathode leads to a higher density of sputtered atoms of the cathode material with lower ionization potential and in rare gas discharges Penning ionization can occur [52].

At this time it is agreed that the pendular electrons play a dominant role in the hollow cathode geometry while all other effects can enhance this effect depending on specific operating conditions. A direct consequence of the pendular electrons is the reduction of the cathode fall thickness and an increase of the electric field at the cathode surface and as consequence higher ion energies at the cathode surface.

The influence of the other mechanisms can be influenced through variations of operating parameters such as fill gas and pressure, cathode material and cathode geometry. The individual processes contributing to the hollow cathode effect are quite well understood but the importance of any of these processes is not clear for a specific situation.

4.2 Discharge Electrical Behavior

A typical current voltage characteristic for the hollow cathode discharge is shown in Fig. 4.3. The curve H corresponds to hollow cathode discharges, the curve noted P has been calculated for parallel plate electrodes separated by the same distance of the hollow cathode discharges electrodes [53].

Contour of constant potential for four selected points along the characteristic H are illustrated in Fig. 4.4. At low currents the discharge exists only in the interelectrode volume. The situation is analogous to the plane-plane electrode configuration and the current voltage characteristics for both configurations are identical at these low currents (Townsend mode).

As the current increases, the plasma enters the cathode cavity and the voltage slightly decreases. However, the plasma is concentrated near the discharge axis and does not extend beyond the aperture diameter until the discharge current exceeds about 1 mA. Although an enhanced field exists in the hollow cathode effect is not important because the electrons can not be trapped and oscillate in the cavity (there are no opposite and adjacent sheaths).

The current increase beyond the point h8 is due to the rapid radial expansion of the plasma in the cathode cavity. Point h8 is the onset of the hollow

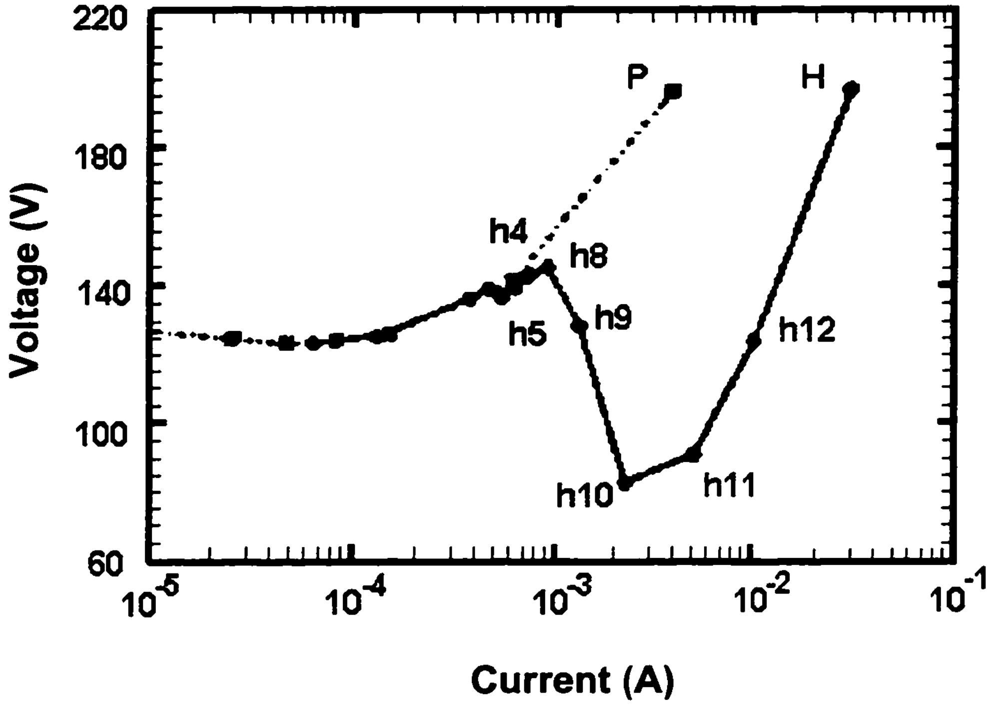

FIG. 4.3. Current–voltage characteristics for hollow cathode (full line) and plane cathode (dash-dot) geometries [53].

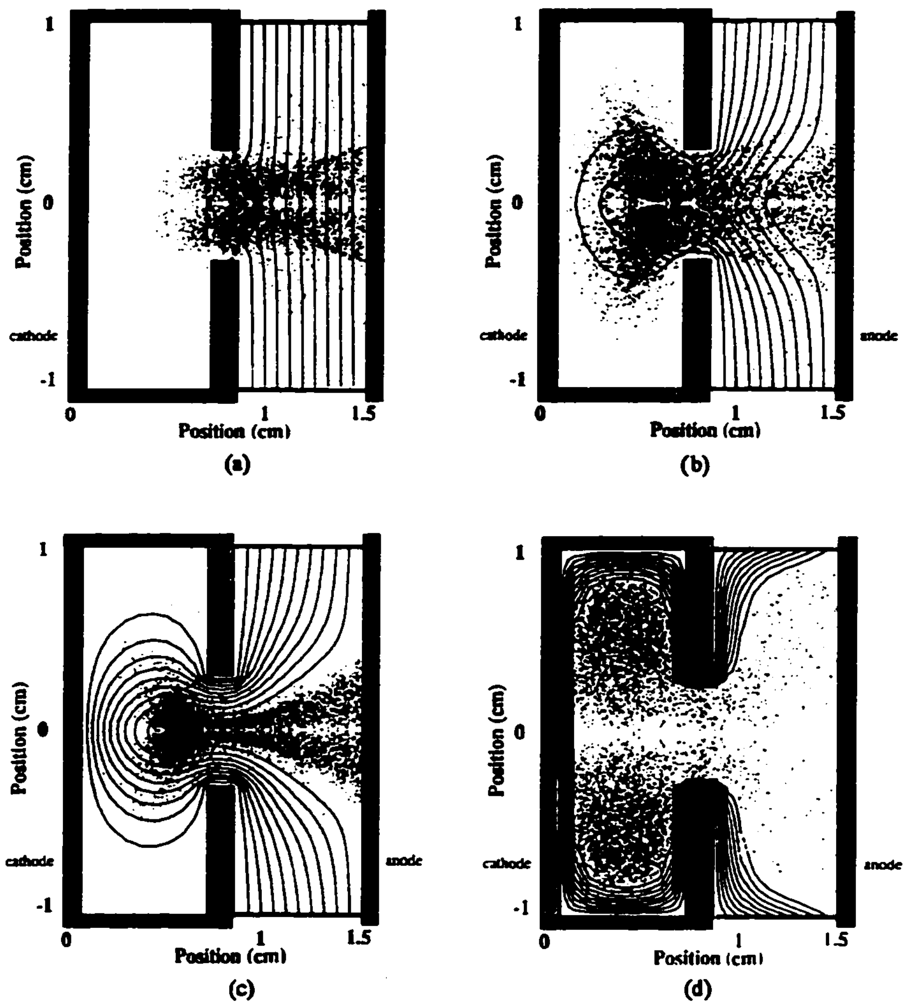

FIG. 4.4. Contour of constant potential at four different points, with dots superiposed to indicate representative ionization events: (a) Point h4 Townsend discharge (b) Point h5 Plasma enters cavity (c) Point h8 onset of hollow cathode effect (d) Point h12 Plasma expansion in the cavity [53].

cathode discharge. The sheaths expand progressively along the cathode inner surfaces and the fast electrons (secondary electrons emitted from the cathode surface or created by ionization in the sheath) are forced to oscillate between the opposite sheaths until they lose most of their energy in collisions with neutrals. The appreciable increase of the ionization efficiency due to pendulum electrons is accompanied by a considerable drop of the discharge sustaining voltage.

The plasma fills the whole volume of the hollow cathode at the point h10 and the sheath covers the entire cathode surface. This situation is similar to the abnormal glow in the plane-plane geometry. As the current increases, the plasma density increases and the sheath length correspondingly decreases. For points on the high current side of h10, a further increase in the current requires an increasing voltage and the I-V characteristic becomes again positive.

4.3 Electron Energy Distribution Function

To determine the electron energy distribution Borodin and Kgan [54] performed experiments using a Langmuir probe in a cylindrical hollow cathode. The results were compared with measurements performed in the positive column of a glow discharge (Fig. 4.5). These experiments show that the hollow cathode has more electrons in the high energy tail of the distribution (above ~` 16 eV) than the positive column, but also more electrons in the low energy regime (below ~ 4 eV). These results suggest the existence of two electron groups. These probe measurements, however, did not have the necessary sensitivity to measure the low density of the beam electrons.

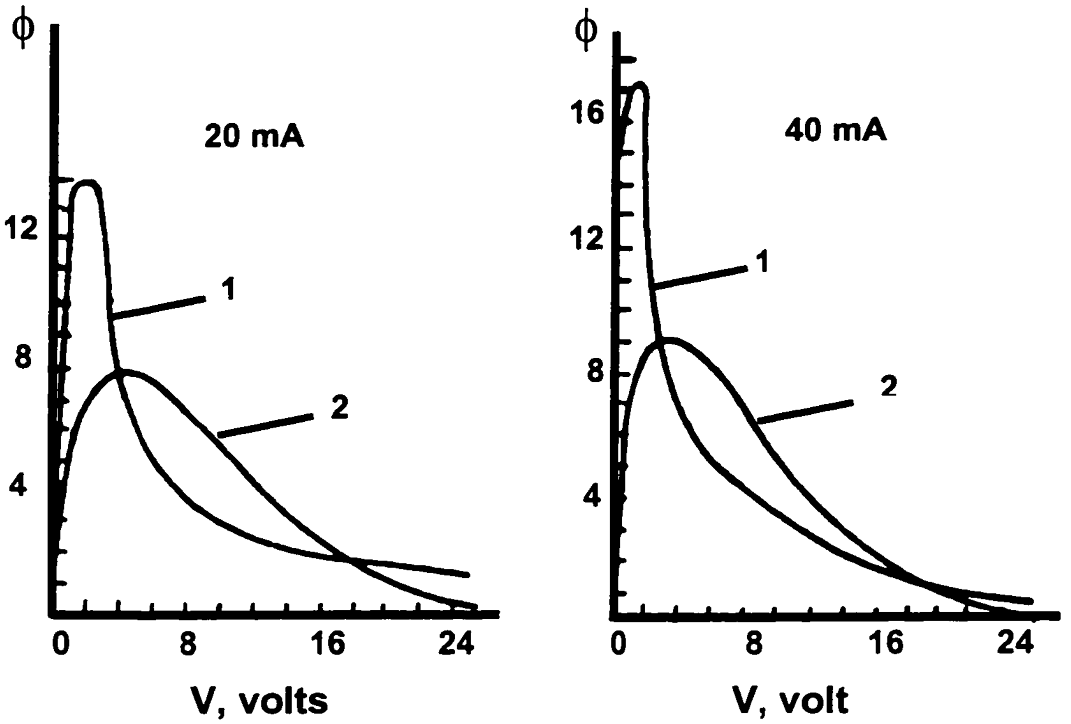

FIG. 4.5. Comparison of the electron energy distribution functions in a hollow cathode and in a positive column [54].

A full analysis of the electron energy distribution has been performed by Gill and Webb [49] using a differentially pumped retarding field analyzer. These measurements cover the full energy range from zero up to the maximum possible energy of the beam electrons. The high-energy tail is shown in Fig. 4.6. The energy distribution comprise three regions: (1) The peak with the highest energy represents the beam electrons with the full cathode fall energy. (2) Following an empty gap, we find electrons that have undergone one or more inelastic collisions and secondary electrons generated with high energies. (3) The low energy group consists of the electrons, after their energy relaxation.

Further studies have concentrated on the density of fast electrons and their dependence on the HCD operation conditions. Badareu et al. [55] suggested that an additional coupling exists between the different groups of the distribution function. The interaction of the beam electrons with the plasma of the negative glow generates waves from which the thermal electrons gain energy.

4.4 Scaling of Hollow Cathode Discharges

If we consider the hollow cathode a glow discharge between the inner surface of the cathode hole and a virtual anode on axis of the hole similarity laws for glow discharges indicates that the voltage scales with the product of pressure, p, and the cathode hole diameter, D, and with the ratio of current density, J, and the square of the pressure:

$$V = V(pD, J/p^2) \tag{4.1}$$

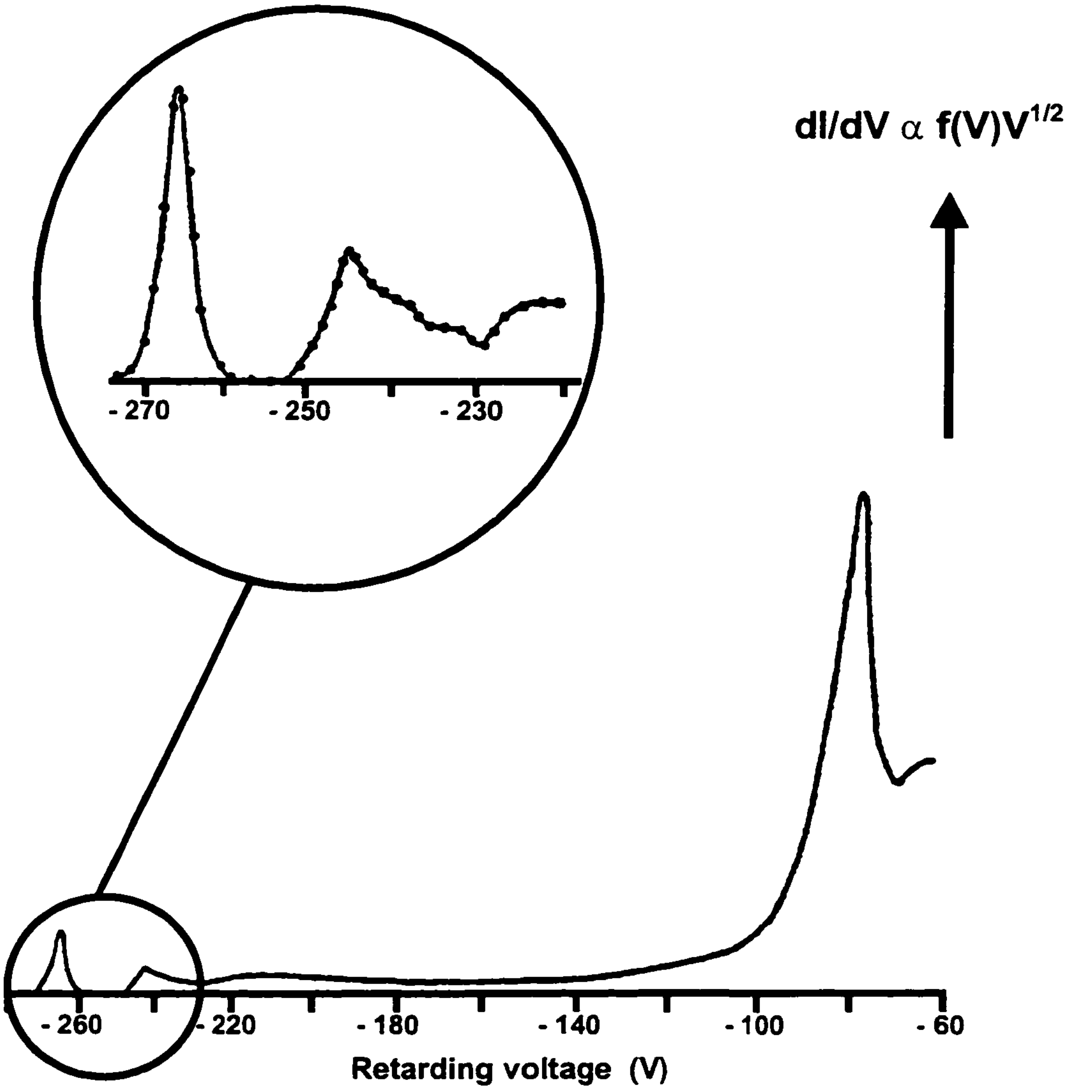

FIG. 4.6. Measured electron energy distribution function in hollow cathode discharge retarding field analyzer [49].

Allis [56] and white [47] found a slightly modified law is more consistent with experimental results:

$$V = V(pD, I/p) \tag{4.2}$$

where V is the sustaining voltage, and I is the discharge current. The range of operation for hollow cathode discharges ranges from pD values of fractions of Torr cm to approximately 10 Torr cm.

4.4.1 Lower limit of the Hollow Cathode Discharge

According to Helm [57], The lower limit in pressure for this effect to occur is determined by the loss of pendel electrons, which reach the opposite cathode wall and are removed from the discharge. This condition leads to an expression for the minimum value of gas pressure, p times the cathode hole diameter, D for which the hollow cathode discharge can be sustained [58]

$$pD = \ln f^{-1} \Big/ \left(\langle\sigma\rangle n_0\right) \tag{4.3}$$

with n_0 being the gas density at a pressure of 1 Torr , and f being a loss factor. The average collision cross section $\langle\sigma\rangle$ is defined as the integral of the energy dependent elastic and inelastic cross sections over the electron accelerating cathode fall, the negative glow, and the electron decelerating cathode fall at the opposite cathode wall, divided by the cathode hole diameter. It was found that for Argon the critical value for pD is 0.026 Torr cm.

4.4.2 Upper Limit of the Hollow Cathode Discharge

The upper limit in pD is given as 10 Torr cm in [59] (without a discussion of the physical process determining this limit), and was found to be approximately 5 Torr cm in experimental studies performed at the PERI laboratory [60]. A model describing the upper limit in pressure for hollow cathode discharge operation is discussed in the following [60].

When the current in the hollow cathode discharge is increased the discharge becomes an abnormal glow discharge, where any increase in current is only possible by increasing the cathode fall voltage: the slope of the current-voltage characteristic turns positive again [53]. The pD value for the transition from the hollow cathode discharge to the abnormal glow discharge (which is identical to the upper limit in pD for hollow cathode discharges) can be estimated by assuming that the pendulum motion of the electrons ceases to exist when the sum of the lengths of the two opposite cathode falls and the negative glow becomes greater than the cathode hole diameter. The cathode fall thickness for plane cathodes is, according to Aston[61]:

$$d_{an} = B^* / p + B / J^{1/2} \tag{4.4}$$

where B* and B are constants depending on gas and electrode material, and J is the current density. The width of the negative glow corresponds to the range of electrons that have been accelerated by a potential difference equal to the cathode drop. For argon, and a potential drop of 200 V, the length of the negative glow is l_0 = 1 cm at a pressure of p_0 =1 Torr [62]. Assuming that this distance scales linearly with 1/p, the condition from the upper limit in pD for hollow cathode discharges reads

$$pD = 2B^* + 2pB / J^{1/2} + l_0 p_0 \tag{4.5}$$

For argon (and an aluminum cathode), B* is 0.054 Torr cm, and B is 0.0034 cm $A^{1/2}$[61].

For high pressure the second term becomes dominant. For a current density of 10 A cm^{-2} the second term exceeds the sum of the first and third for pressures greater than 535 Torr. Only for pressures far below this value is the upper limit for hollow cathode discharge operation dependent on pD. With the data given above, up to pressures where the value of the second term is less than 10 %, the upper limit of pD is 1.1 Torr cm, a value small compared to the experimentally obtained upper limit for hollow cathode discharge operation (5 Torr cm). However, we need to consider that this value relies on empirical data, obtained for different cathode material than those of experimental measurements. From a practical point of view, the upper limit for HCD is expected to be ~ 5 Torr cm. Thus, increasing the pressure requires a reduction in the cathode hole diameter D leading to the development of "***Microhollow Cathode discharges (MHCD)***"

4.5 Microhollow Cathode Discharge Excimer Lamps

The non-Maxwellian characteristics of the electron energy in low pressures hollow cathode discharges, with large concentrations of electrons with energies well over 10 eV, have been discussed in a previous section. A non-thermal electron energy distribution is also expected for high-pressure hollow cathode discharges. If this assumption holds true, high pressure operation of hollow cathode discharges, using small diameter hollow cathodes would make these discharges promising candidates for excimer lamps and plasma reactors for detoxification of gases. The theoretically predicted [53], and experimentally observed [58, 60] resistive behavior of such discharges over a large range of current would allow their use in simple, unballasted arrays. Fig. 4.7 shows a schematic of a Microhollow Cathode Discharge Excimer Lamp.

Possible advantages of using microhollow cathode discharge (MHCD) arrays as excimer lamps are:

- Low voltage requirements (less than 1 kV).
- Pulsed or DC operation.
- Homogeneity of emission (determined by the dense arrangement of hollow electrode discharges).
- Higher power density of MHCD arrays compared to barrier discharges.
- Low cost.

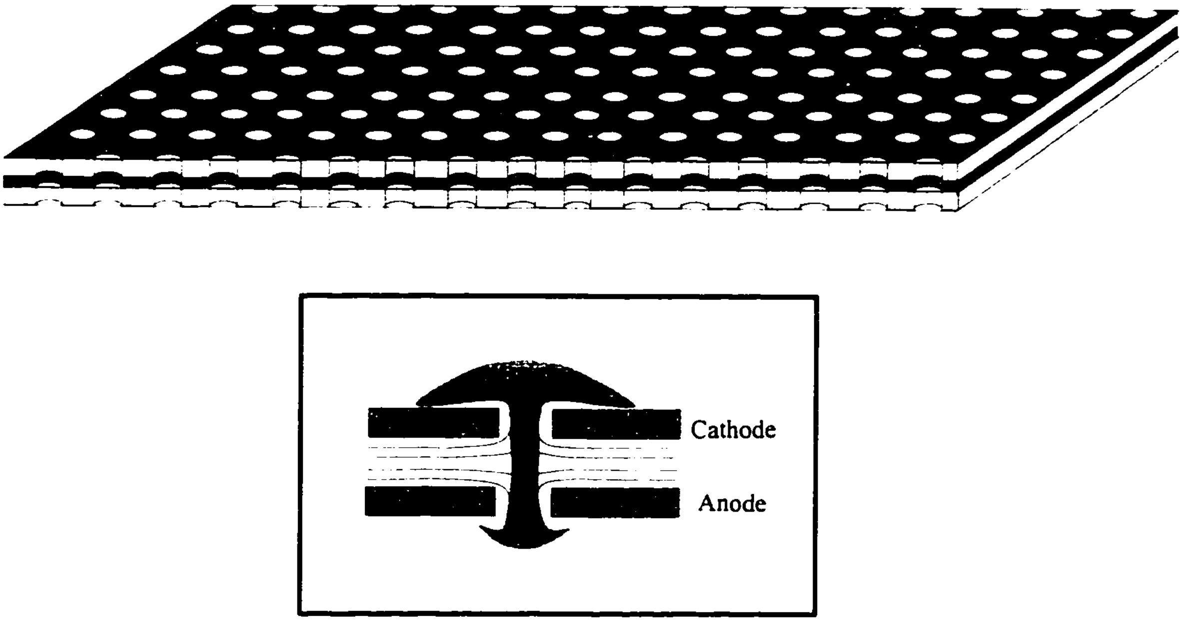

FIG. 4.7. Microhollow cathode discharge excimer lamp.

CHAPTER V

EXPERIMENTAL SET-UP AND PROCEDURES

5.1 Electrode Geometry

Measurements were performed on Microhollow Cathode discharges (MHCD) in flowing argon at 380 sccm and in xenon without flow. The cathode consists of a perforated Molybdenum film with a hole of 200 μm or 100 μm in diameter and a thickness of 100 μm. The Molybdenum anode is a disc shaped with a diameter of 1 cm. For experiments with hollow electrodes, we used an anode identical to the cathode. The cathode is separated from the anode by a 200 μm mica spacer. DC voltages of up to 1000 V were applied.

This electrode geometry is a simplified version of hollow cathode discharge geometries where the cathode contains a hole, Fig. 5.1a and has been used in previous studies [58]. A second version of a hollow cathode geometry, a geometry used in experiments on pseudosparks [63] is shown in Fig. 5.1b, where the cathode forms a cavity. This geometry can be reduced to a two plate configuration by removing the bottom plate and the cylindrical part of the cathode. Since the shape of the anode is only of minor importance for the physics of the hollow cathode discharge [48], the anode opening can be closed or opened, resulting in the geometry used in our studies (Fig. 5.1c). The hollow cathode is now reduced to the circumference of the cathode opening and the area on the cathode plate adjacent to it. The electrode geometry has been chosen due to its simplicity. Variable parameters are the electrode spacing and hole diameter. This assumes that the electrode material and dielectric play minor

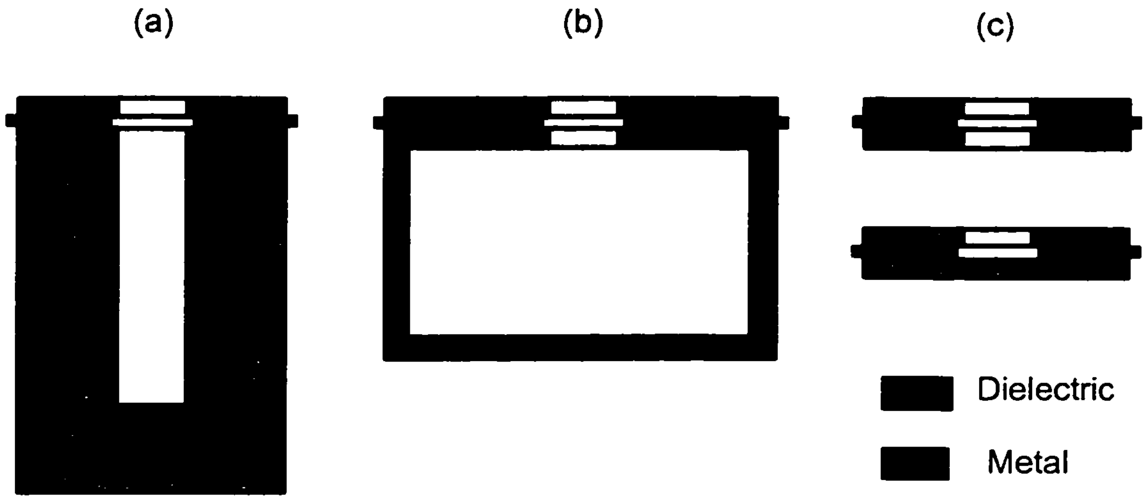

Fig. 5.1. Different hollow cathode discharge geometries.

roles in the physics of the discharge. Another advantage of this geometry is the fact that arrays of micro electrodes can easily be fabricated by means of laser drilling or etching methods. For this study only the hole diameter has been varied.

5.2 MHCD Experimental Set-up (Fig. 5.2)

5.2.1 Discharge Chamber

A schematic of the gas discharge chamber is shown in Fig. 5.3. This chamber is a combination of CF flanges and QF hardware. All dielectric parts are made of macor. The hollow cathode-anode sample is held together by macor plates using nylon screws.

The top window of the chamber is MgF_2 with high transmittance in the VUV range (~ 80% at 172 nm & ~55% at 126 nm). This window separates the gas discharge from the vacuum monochromator. The bottom window is regular glass and is used to monitor the discharge in the hollow electrodes experiment.

5.2.2 Electrical Circuit

The electrode geometry and the dc electrical circuit are shown in Fig. 5.4. The voltage V_0 is supplied by a Hipotronics, variable HV DC power supply from 0 to –5 kV. A resistor of 1 kΩ is used as current viewing resistor for the discharge. A resistor of 100 kΩ limits the current in the discharge. V_1 reads the voltage across the current viewing resistor. The discharge voltage is calculated by subtracting the reading of the two multimeters V_1 and V_2. In order not to affect the discharge with the multimeter resistance, V_2 was measured using a high voltage probe Tektronix P6015 1000X.

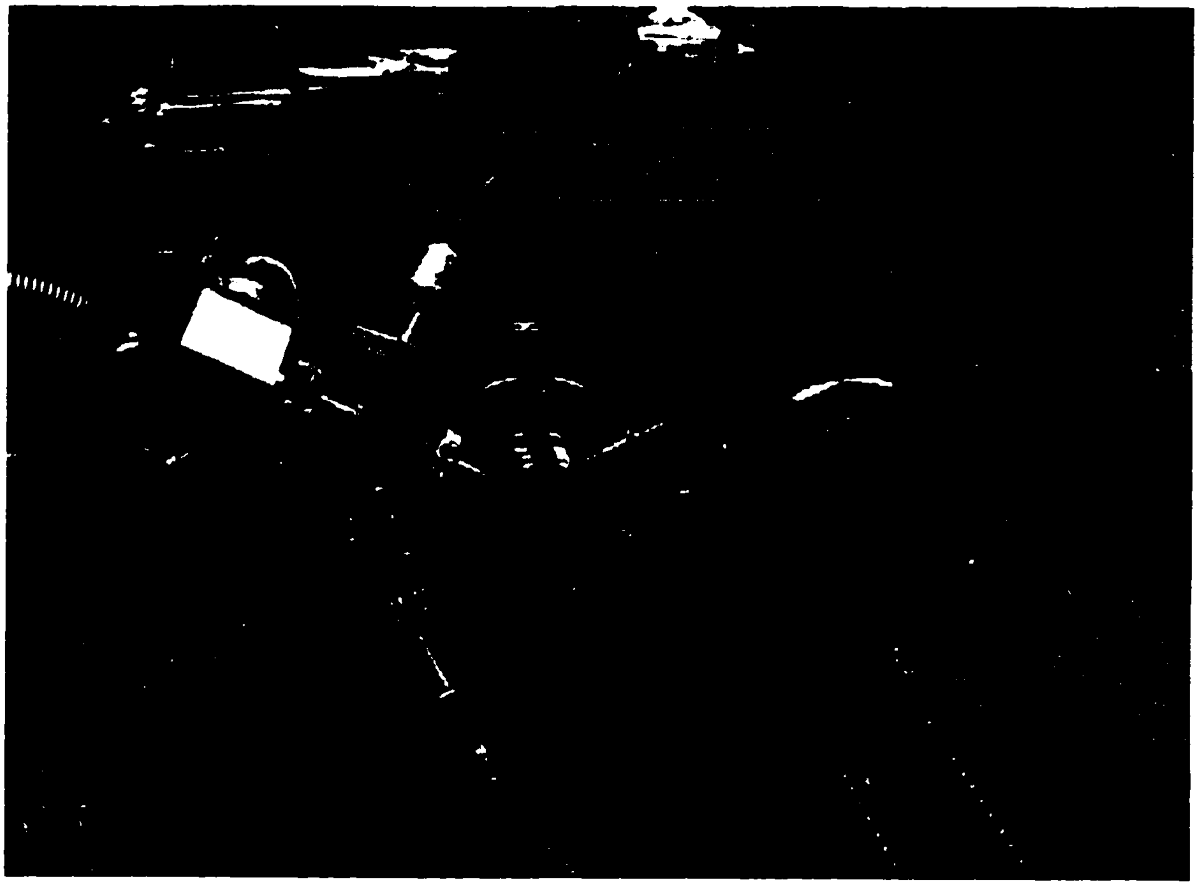

FIG. 5.2. MHCD experimental set-up.

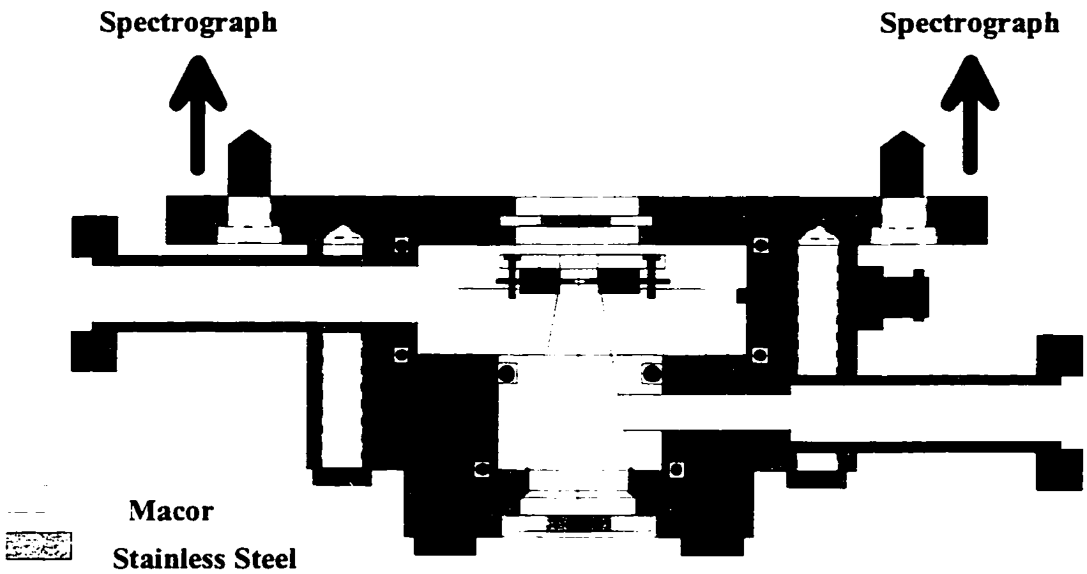

Section Elevation

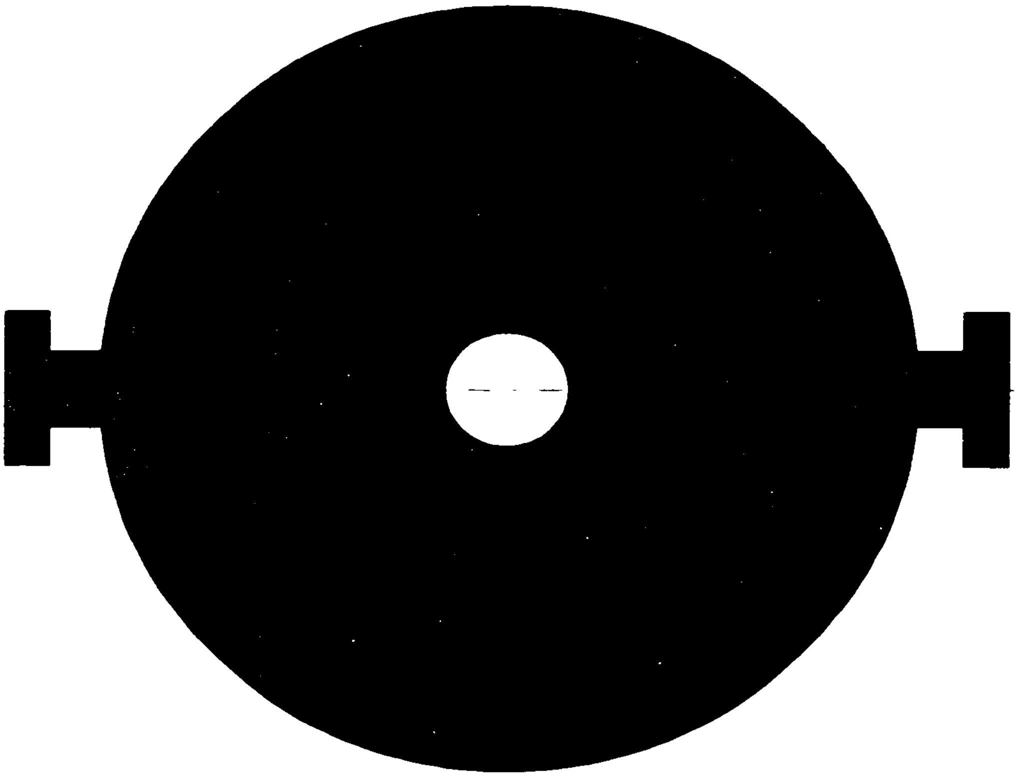

Plan

FIG. 5.3. Discharge chamber.

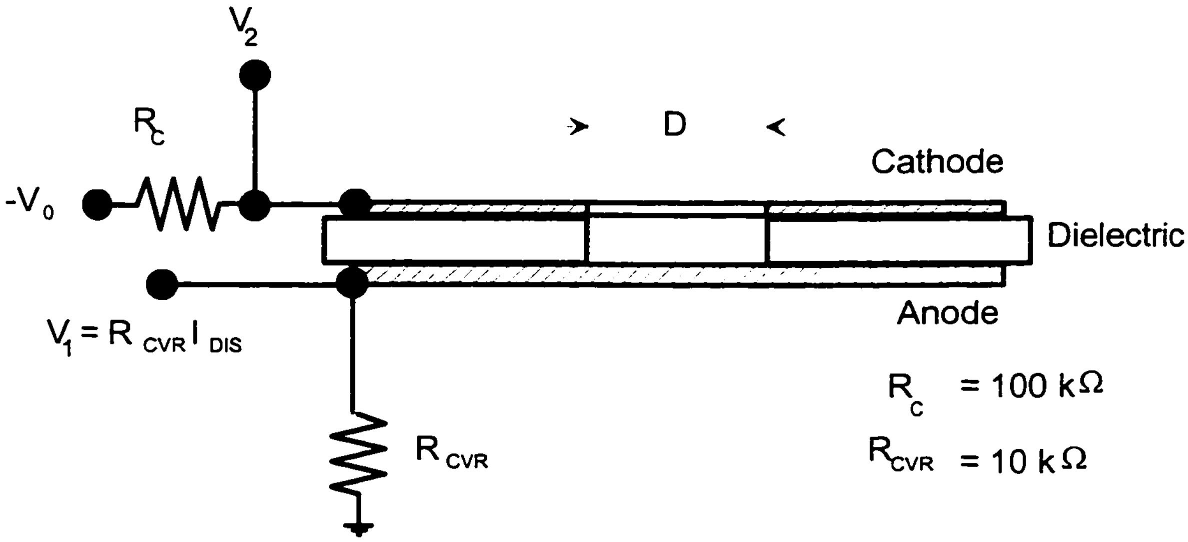

FIG. 5.4. Cross section of the gas discharge gap, and electrical circuit.

5.2.3 Vacuum System

A two stage mechanical vacuum pump Alcatel was used to evacuate the chamber to the mTorr range before each experimental run. In the xenon experiments the chamber was then filled with the gas at the required pressure. For argon, where we operated in flowing gas, the pump valve and the needle valve were used to control the argon flow and consequently the pressure.

Through the course of the experiments in xenon it was found that high purity environment is required for optimum results. In order to improve the vacuum system, a turbomolecular pump was added. The discharge chamber, before each experiment, was evacuated to a pressure of $5*10^{-5}$ Torr and then filled with high purity (99.95%) xenon.

After evacuating the chamber, the residual gas pressure was measured by a Bayard-Alpert ion gauge. This gauge is able to measure pressures down to 10^{-10} Torr. The pressure of the gas in the chamber was kept in the range between few Torrs and atmospheric pressure. A diaphragm manometer was used to measure the gas pressure. This manometer is unaffected by gas composition.

5.3 Experimental Set-up for VUV Spectroscopy

Spectral measurements have been performed using a 0.5 m Mcpherson monochromator, model 219. As shown in Fig. 5.5 the discharge chamber with a MgF_2 window was mounted directly to the inlet of the monochromator. The exit of the monochromator is connected to a modified 650 Mcpherson detector assembly with an R375 Hamamatsu Photomultiplier (PMT). Using an A/D

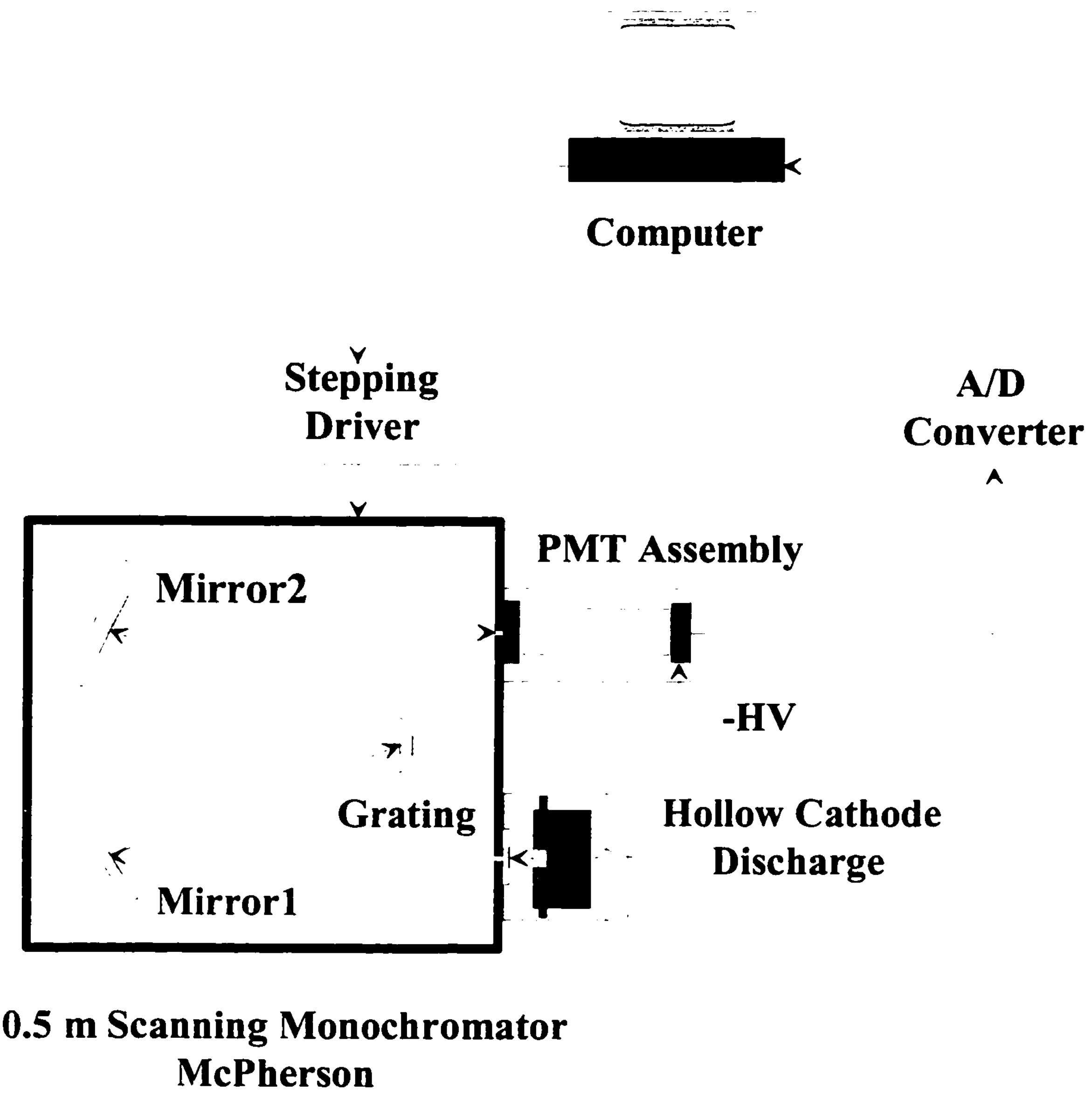

FIG. 5.5. Experimental set-up for VUV spectroscopy.

converter and a stepper drive scan controller, the complete scanning process is computerized. Fig. 5.6 shows a picture of the real system used in our experiment.

5.3.1 McPherson Model 219 Vacuum Spectrograph/ Monochromator

The McPherson model 219 is a 0.5 meter scanning monochromator / spectrograph. It is designed to operate in the wavelength range from 105 to 16,000 nm by interchanging SNAP-IN gratings. The optical system is a modified Czerny-Turner type. It employs two concave mirrors and a plane grating. The collimating mirror is 3" in diameter and has a 0.5 meter focal length. The focussing mirror is 6" in diameter and has a 0.5 meter focal length with a 4" focal plane. The grating is a 50mm x 50 mm ruled area on a SNAP-IN blank. All experiments are made with a 600 G/mm grating blazed at 150 nm. All optics in the monochromator are magnesium fluoride coated to increase their efficiency in the VUV range.

The entrance and exit slits are bilaterally adjustable in the range of 10 microns to 2 mm. With slit openings of 600 μm, our instrument resolution was ~ 2nm full width at half maximum (FWHM).

5.3.2 Modified Model 650 Detector Assembly

The model 650 detector assembly is designed for use with McPherson VUV monochromator and was modified to accommodate a PMT Hamamatsu R375. The R375 has a multialkali photocathode with a synthetic silica window. The synthetic silica transmits ultraviolet radiation down to 160 nm.

FIG. 5.6. Picture of the real system.

In order to extend the spectral response of our detection system to the low VUV a sodium salicylate scintillator is used in connection with the PMT. The VUV radiation leaving the exit slit of the monochromator hits the sodium salicylate coated vacuum tight window, causing it to fluoresce. The fluorescent light (at a wavelength of approximately 420 nm) passes through an air gap, the window of the photomultiplier and strikes the photocathode surface. For exciting radiation between 40 and 340 nm, the absolute quantum efficiency of sodium salicylate is 65% [64]. The detector responsivity cut-off is at 850 nm. Higher than 340 nm, the scintillator can be considered as a window that transmits incident light. The combination of sodium salicylate scintillator and photomultiplier tube is sensitive to radiation from 30 nm to 850 nm and is reasonably linear in the VUV range between 100 to 200 nm.

5.3.3 McPherson Model 789A-3 Stepper Drive Scan Controller

The model 789A-3 scan controller provides high resolution stepper motor scanning system. With an interface to the computer, this scanning system is used to automate the MHCD spectroscopy. Through the RS232 interface, the computer gives signals to control the stepper motor motion and hence moving the grating with different angular positions that correspond to different wavelengths. An AD500 P4 KEL-AM A/D converter takes the output of the PMT to the computer.

5.3.4 Computer Program Overview

To assure maximum repeatability, the monochromator drive mechanism is always scanned from lower to higher wavelength values. The system is designed for incremental scans, wherein the grating drive moves from one position to the next in a group, with data acquisition performed when each desired position is reached. The data, as it is acquired at each increment, is plotted on an autoscaling graph in the appropriate operating mode. When the scan finished, the information is saved to a file for later viewing with any post processing software package. Typical scanning step in our experiment was 1 nm.

5.3.5 Vacuum Provision

The entire system including the monochromator, the space between the source and the entrance slit, and the space between exit slit and detector was evacuated. For evacuation, a turbomolecular pumping station Leybold TOSS 50 was connected to the pumping port of the monochromator. Measurements were performed at a system pressure of 4.5×10^{-6} Torr.

In order to protect the system, specifically the grating and the optical parts, from the oil vapor an assimilation trap CWTR-100 Kurt J.Lesker is being used which prevents oil vapor from reaching the spectrograph. A vacuum sentry series 145 HPS protects the vacuum system from oil back streaming in case of a power failure.

5.4 Spectral Calibration

Before any spectra measurement on the microhollow cathode discharge, the spectroscopic system was calibrated using a mercury lamp (UVP Pen Ray). Pen ray lamps are low pressure, cold cathode UV lamps made of double bore quartz tubing. Their output is characterized by narrow, discrete and intense lines in the range from 180 to 600 nm. These lines were used to calibrate the monochromator with respect to wavelength. No intensity calibration was made at this point. The mercury lamp spectrum, as it appeared in the spectral output of our system, was recorded and compared with the spectrum of the lamp, provided by the manufacturer. Accordingly, any shift on the mercury lines was added or subtracted from any spectral measurement in our experiment.

Before any experiment, a zero adjustment for the monochromator was made. The zero of the instrument is defined as the dial reading when the grating is at its zero order and works as a mirror. At the real zero, the detector should read the highest signal. Thus, by scanning the measured discharge spectrum around the dial zero the reading corresponding to the real zero can be identified. Measured shifts in this value were taken into account in all recorded spectra.

5.5 Sample Conditioning

Conditioning of the discharge samples is a critical step in getting stable and reproducible results from the discharge. Two conditioning techniques were applied. In the first method, the sample was conditioned by running the discharge at low pressures (<100 Torr) in argon with low currents (<2 mA) for half an hour and then evacuated to 45 mTorr for at least two hours before filling with the gas.

Recently, we have developed a better sample conditioning and cleaning procedure. This new method which is described in the following resulted in an increased excimer radiation from xenon discharges by at least one order of magnitude. The sample was conditioned by running the discharge at low pressure (< 100 Torr) with high current in xenon (> 3 mA) for half an hour. Then, the discharge is turned off and the chamber was left evacuated overnight to 5 x 10^{-5} Torr.

5.5.1 Effect of Sample Conditioning

When the discharge run first at low pressure plasma cleaning of the cathode is achieved. This effect can be explained as follows: when an ion strikes the cathode, its energy is sufficient to extract an electron from the cathode, which neutralizes the ion, and may release a second electron, giving secondary emission. However, its energy is also to release an atom of the cathode from the surface, so that the actual material of the cathode is being continuously eroded by the bombarding ions. This phenomenon is called cathodic sputtering. The rate of sputtering of molybdenum is inversely proportional to p^n where n is larger than 2. It is clear that ion bombardment provides a means of continually removing the cathode surface and exposing fresh material beneath. Molybdenum is an active absorber of impurity gases and the sputtered atoms are in a highly reactive conditions. The effect of sputtering molybdenum is therefore to absorb reactive gases at a far higher rate than the inert gases. By evacuating the system after this run impurities are removed with the sputtered metal and the cathode surface is cleaned and a new surface is exposed. Now impurities are removed from the system. As a result, the energy deposited in the discharge mainly goes to the formation of the xenon excited state and excimer formation.

5.6 Absolute Measurements

In order to determine the absolute values of the excimer radiation two methods were used. The first one was based on comparing the discharge emission with that of calibrated UV sources (Mercury vapor lamp with line emission at 184.9 nm and a Deuterium lamp with continuum emission from 160 to 400 nm), the second one on radiometric techniques.

5.6.1 Calibrated Sources

For measurements with calibrated sources, the lamps were mounted directly to the inlet of the monochromator in the same way as the discharge chamber, and the same MgF_2 window was used as that in the chamber.

The relation between the photomultiplier reading, $R_D(\lambda)$, for emission at a wavelength, λ, within a wavelength interval, $d\lambda$, and the radiant power of the discharge, $P_D(\lambda)$, is as follows:

$$\frac{dR_D(\lambda)}{d\lambda}d\lambda = K(\lambda)P_D(\lambda)d\lambda \qquad (5.1)$$

where $K(\lambda)$ is a coefficient which represents the transmission of the spectrograph, the detector-scintillator sensitivity and the ratio between the total radiant power and that incident on the spectrograph inlet slit.

A similar relation holds for the calibrated source:

$$\frac{dR_S(\lambda)}{d\lambda}d\lambda = K(\lambda)P_S(\lambda)d\lambda \qquad (5.2)$$

where $P_S(\lambda)$ is the radiant power of the calibrated source.

For our spectrograph grating blazed at 150 nm, the transmission of the instrument between 150 and 200 nm varies within only a few percent. The scintillator response is also almost flat over the spectral range between 150 to 200 nm. It is therefore reasonable to assume that K is a constant in the wavelength range from 150 to 190 nm [65], which is the range of xenon excimer emission. The photomultiplier reading is related to the radiant power of the source at a given wavelength, λ_0, in a wavelength interval, $\Delta\lambda$, which is determined by the resolution of the spectrograph:

$$R_{D.S}(\lambda_0) = KP_{D.S}(\lambda_0)\Delta\lambda \tag{5.3}$$

The wavelength, λ_0, of the calibrated source was selected to be 170 nm for the deuterium lamp and is given as 184.9 nm for the mercury lamp.

It is assumed that the calibrated source is a point source, and that the emission is isotropic. Then the radiant power, P_S (λ_0), at a distance, r', from the source is related to the calibrated irradiance of the source by:

$$P_S(\lambda_0) = 4\pi r'^2\, H(\lambda_0) \tag{5.4}$$

From eqs. 5.3 and 5.4, K can be calculated, and consequently the absolute value of the excimer emission, P_D, at a given wavelength, λ_0, can be obtained.

The total radiant power P_T of the discharge is obtained by integrating over the entire profile of the excimer line:

$$P_T = \int_{\lambda_1}^{\lambda_2} P_D(\lambda)d\lambda \tag{5.5}$$

where λ_1 and λ_2 are the lower and upper bound of the excimer emission, respectively. The discharge efficiency is defined as the ratio of the total radiant power to the input electrical power, which is the product of discharge current and voltage at a given pressure.

As a first calibration source, we have used the pen ray mercury lamp. This lamp is calibrated at a wavelength of 253.7 nm. The intensity value of the 184.9 nm mercury line was obtained by comparing the signals at the two wavelengths and taking the spectral transmission of the system into account. The ratio of the intensity of the 253.7 nm to the 184.9 nm line was found to be 25, which is in agreement with values provided by the manufacturer [66]. The absolute value of the intensity of the mercury line at 184.9 nm was then calculated, and used to determine the radiant power of the excimer emission using eqs. 5.3 and 5.5.

Similar experiments were performed with a deuterium lamp (Oriel BJ2775) with a calibrated spectrum from 160 nm to 400 nm [67]. The radiation in these lamps is a result of an electric arc discharge inside the deuterium gas. The deuterium emission at 170 nm was used as standard to determine the radiant power of the microhollow cathode discharges excimer radiation.

5.6.2 Radiometer Techniques

A second method used to obtain absolute radiant power values is based on radiometric measurements. A calibrated radiometer (IL1400) with a calibrated detector (SED185) was used. The onboard computer interrogates each detector for units, calibration and range information, automatically displaying a calibrated reading in the correct optical units. The SED detector is an Au metal photocathode 8 mm in diameter with a quartz window. Its responsivity covers the range between 160-240 nm with a peak at 185 nm. The detector was mounted on top of the discharge chamber at a distance r = 2.5 cm from the discharge. An air gap of 6.5 mm separated the detector from the discharge window (Fig. 5.7). Considering the discharge as a point source, the irradiance reading of the radiometer was converted to a power reading W by multiplying it by 4 πr^2. This power reading is related to the radiant power, P_D, of the discharge:

$$W = \int_{\lambda_1}^{\lambda_2} P_D(\lambda)T(\lambda)D(\lambda)e^{-\alpha(\lambda)z}d\lambda \qquad (5.6)$$

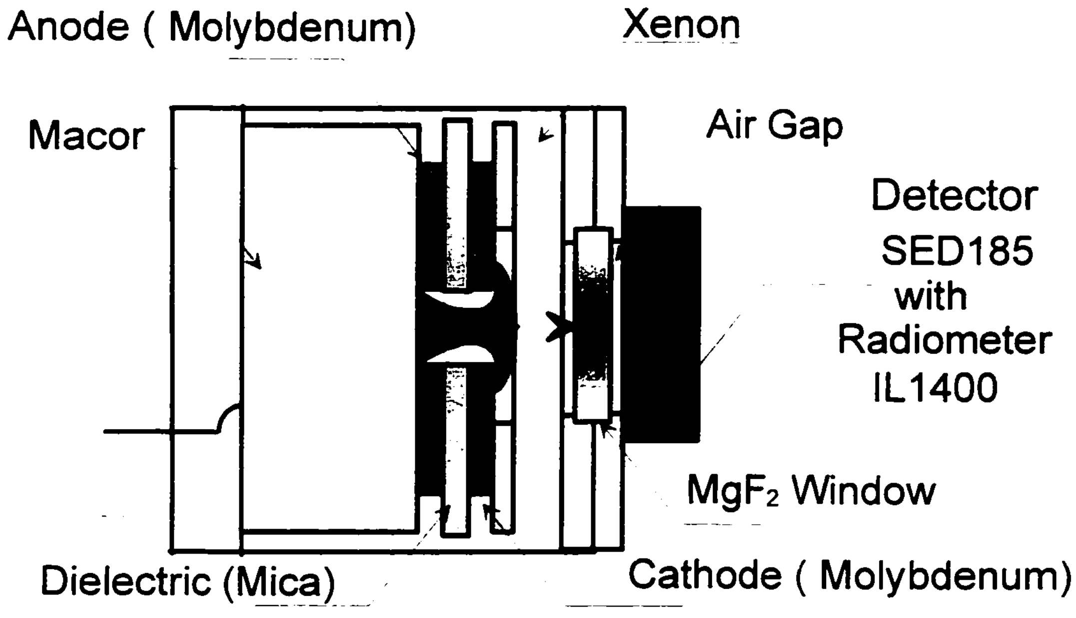

FIG. 5.7. Radiometer measurements.

where $T(\lambda)$ is the transmittance of the MgF_2 window and is ≈ 80% in the range between λ_1 and λ_2, $D(\lambda)$ is the detector responsivity, $\alpha(\lambda)$ is the absorption coefficient of air, and z is the air gap length. Only the oxygen absorption in the air gap was considered. Absorption of nitrogen is known to be negligible. Water vapor absorption in the air gap was not considered in our calculations.

In order to solve for $P_D(\lambda)$ in the integral equation (equ. 5.6) a fitted function for the relative spectral distribution, $P_R(\lambda)$, was used:

$$W = P_o \int_{\lambda_1}^{\lambda_2} P_R(\lambda)T(\lambda)D(\lambda)e^{-\alpha(\lambda)z}d\lambda \tag{5.7}$$

where P_0 is a conversion factor from relative power values to absolute ones. Integrating over the excimer line profile provided the value of P_0 and consequently the total radiant power:

$$P_T = P_0 \int_{\lambda_1}^{\lambda_2} P_R(\lambda)d\lambda \tag{5.8}$$

CHAPTER VI

RESULTS

6.1 Spectral Measurements [68-71]

All data was taken with an increment of 1 nm wavelength. The spectra were not corrected for detector response or for window transmittance.

6.2.1 Argon

In experiments with hollow electrode discharges we concentrated on the emission of argon in the spectral range between 100 and 200 nm. The spectra of discharges operated at 76 Torr, 320 Torr and 760 Torr, respectively, with a 200μm cathode hole are shown in Fig. 6.1.

At low pressure (76 Torr) the spectrum is over the range 100-200 nm dominated by Ar II lines, mostly transitions between states having a $3s^2$ $3p^4$ (^3P) ionic core [72]. In order to exactly identify these ionic transitions, higher resolution, and consequently smaller wavelength increments, is needed. At high pressures all of these lines have disappeared and the main spectral feature is the excimer line. The peak of the excimer line was observed at 130 nm.

The argon spectrum for discharge operation with hollow cathodes of 100 μm diameter at pressures of 76 Torr and 600 Torr is shown in Fig. 6.2. At low pressure (76 Torr), the spectrum over the range of 100-200 nm is dominated by Ar II lines. At high pressures, these lines disappear and the excimer line dominates the recorded spectrum.

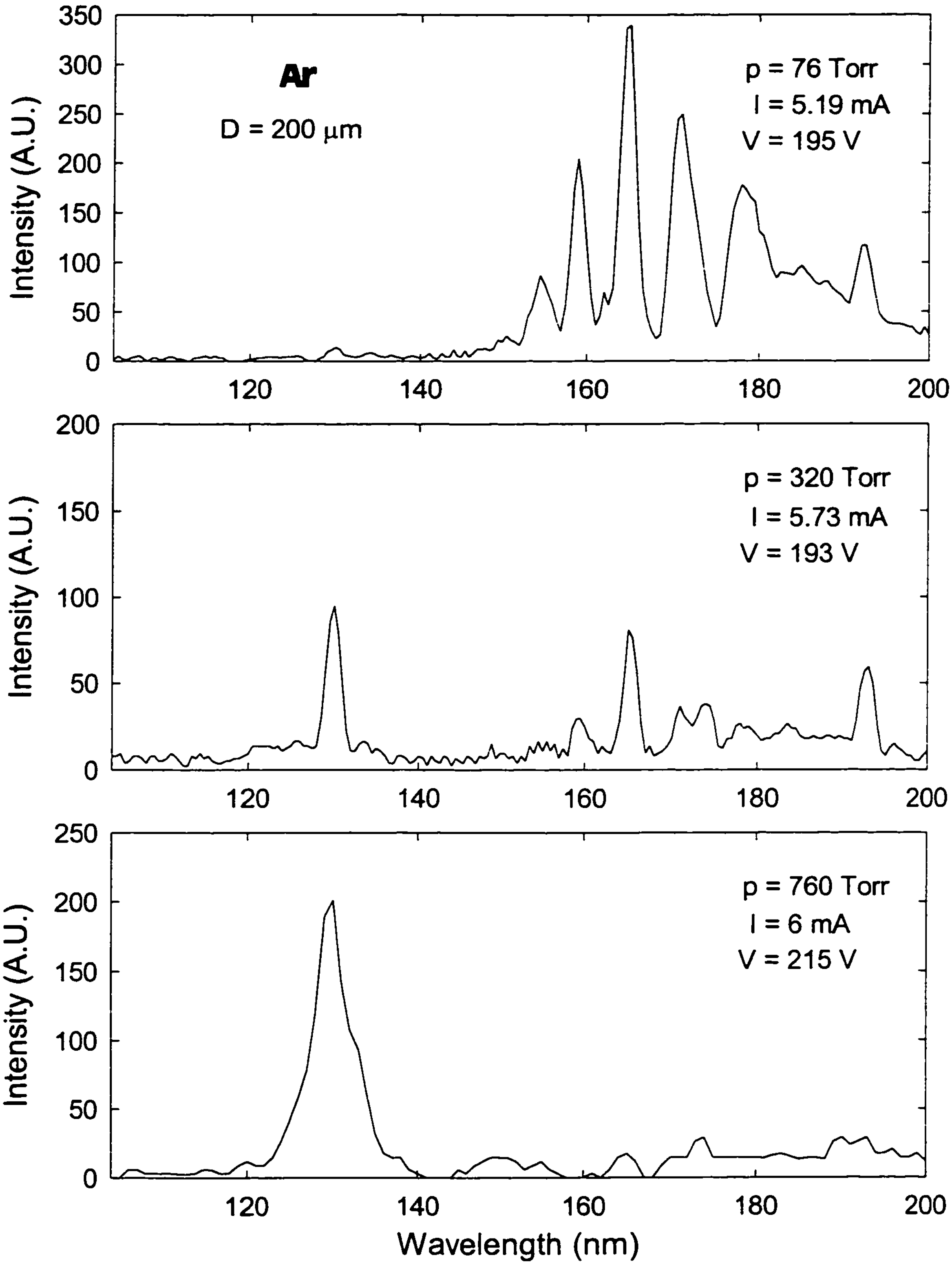

FIG. 6.1. VUV spectra of discharges in argon at pressures of 76 Torr, 320 Torr and 760 Torr with a cathode hole diameter of D = 200 μm.

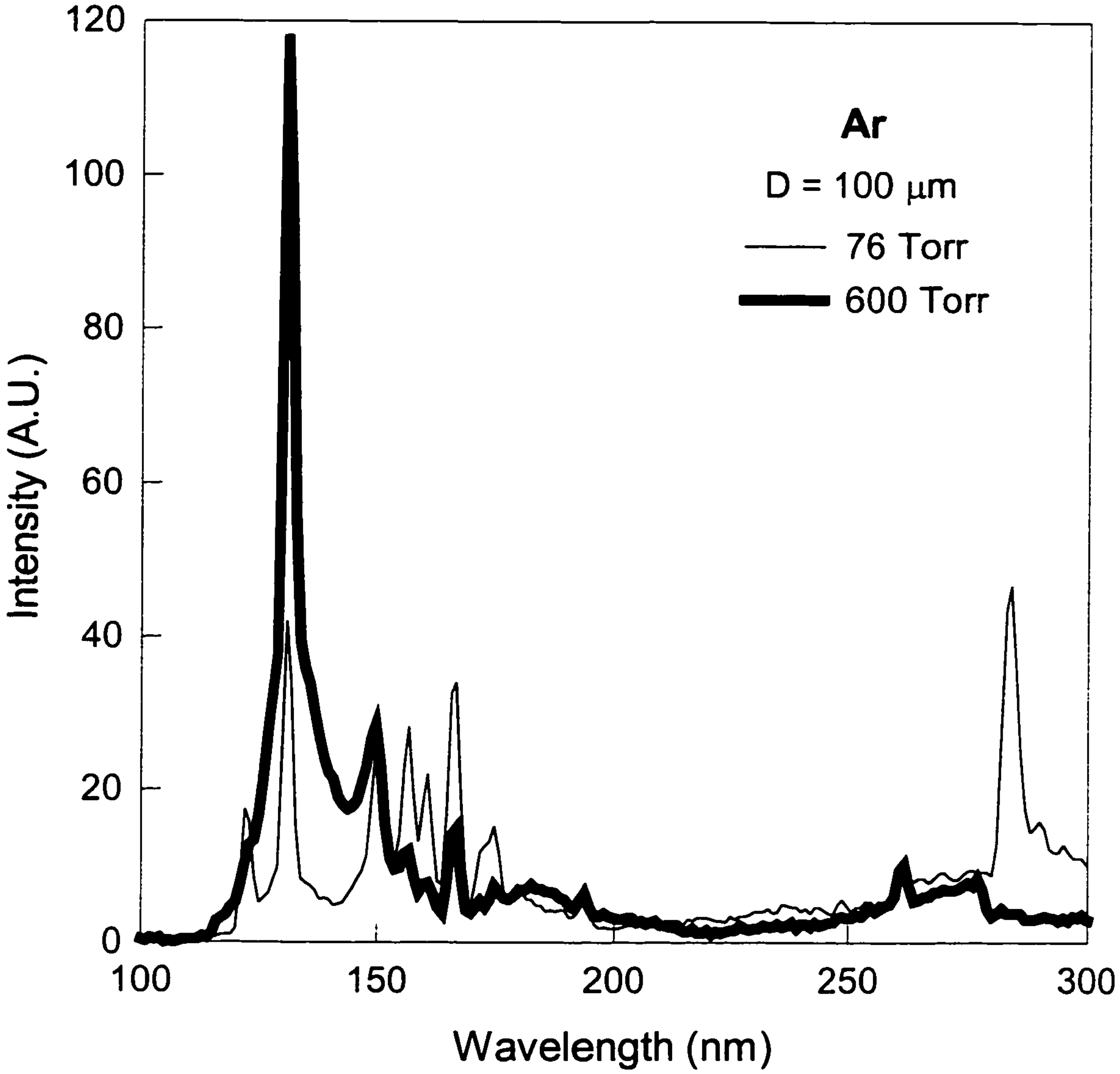

FIG. 6.2. VUV spectra of discharges in argon at 76 and 600 Torr with cathode hole of 100 μm. The sustaining voltage for the lower-pressure discharge was 221 V and the current was 5 mA. For the higher pressure discharge the voltage was 200 V, and the current was 5.4 mA.

The argon discharge was operated in flowing gas, at 380 sccm. Operating the discharge without flow caused a reduction of the intensity by more than an order of magnitude (Fig. 6.3).

6.1.2 Xenon

Experiments in static xenon, with a cathode hole of 200 μm, showed similar emission characteristics as argon. The spectrum of hollow electrode discharge in xenon at 760 Torr is shown in Fig. 6.4.

The spectra of xenon at pressures of 76 Torr and 760 Torr for a 100 μm cathode opening are shown in Fig. 6.5. Most of the lines seen in the xenon spectrum at low pressure are Xe II lines. The line at 315 nm was identified as a molybdenum (electrode material) line. It is also visible in the argon discharge spectrum. In addition, oxygen and nitrogen lines appear in the spectrum resulting from gas impurities. At atmospheric pressure the main feature in the xenon spectrum is the excimer line. However, there is some residue of the impurity lines in the spectral range between 220 and 270 nm. The sustaining voltage for xenon discharges in this measurement was twice as high as for argon discharges, 400 V for xenon versus 200 V for argon.

By careful cleaning and conditioning of the electrodes, as explained in the previous chapter, the forward voltage in the discharge was reduced from 400 V to 220 V with an observed increase in radiation, especially at low pressure. The highest recorded intensity in this experiment was one order of magnitude higher than the corresponding intensity in the experiment without conditioning the electrodes. The xenon spectrum obtained with 100 μm hole in the two electrodes

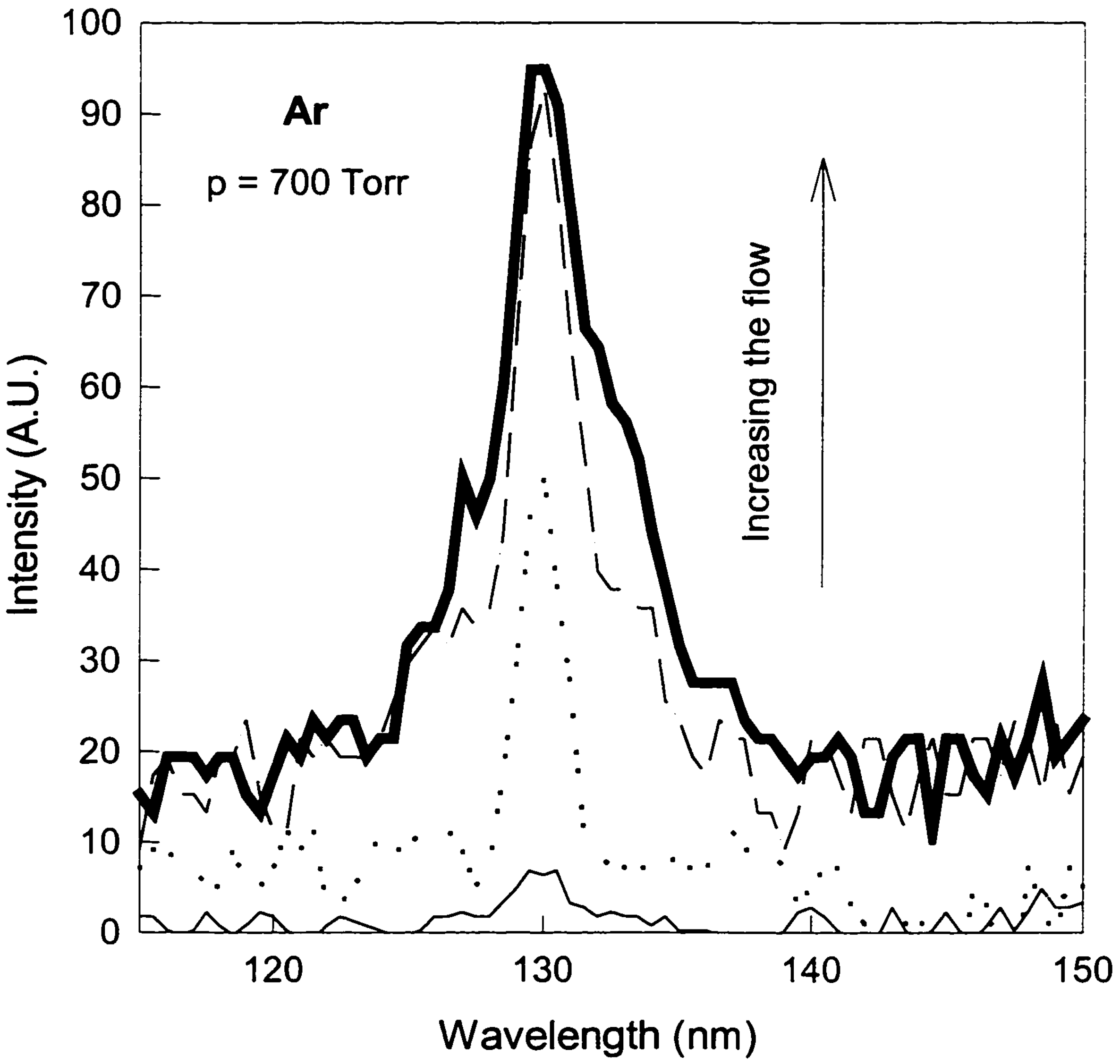

FIG. 6.3. VUV spectra of discharges in argon at 700 Torr with differen flow rate. The lowest curve is static and the highest is 380 sccm.

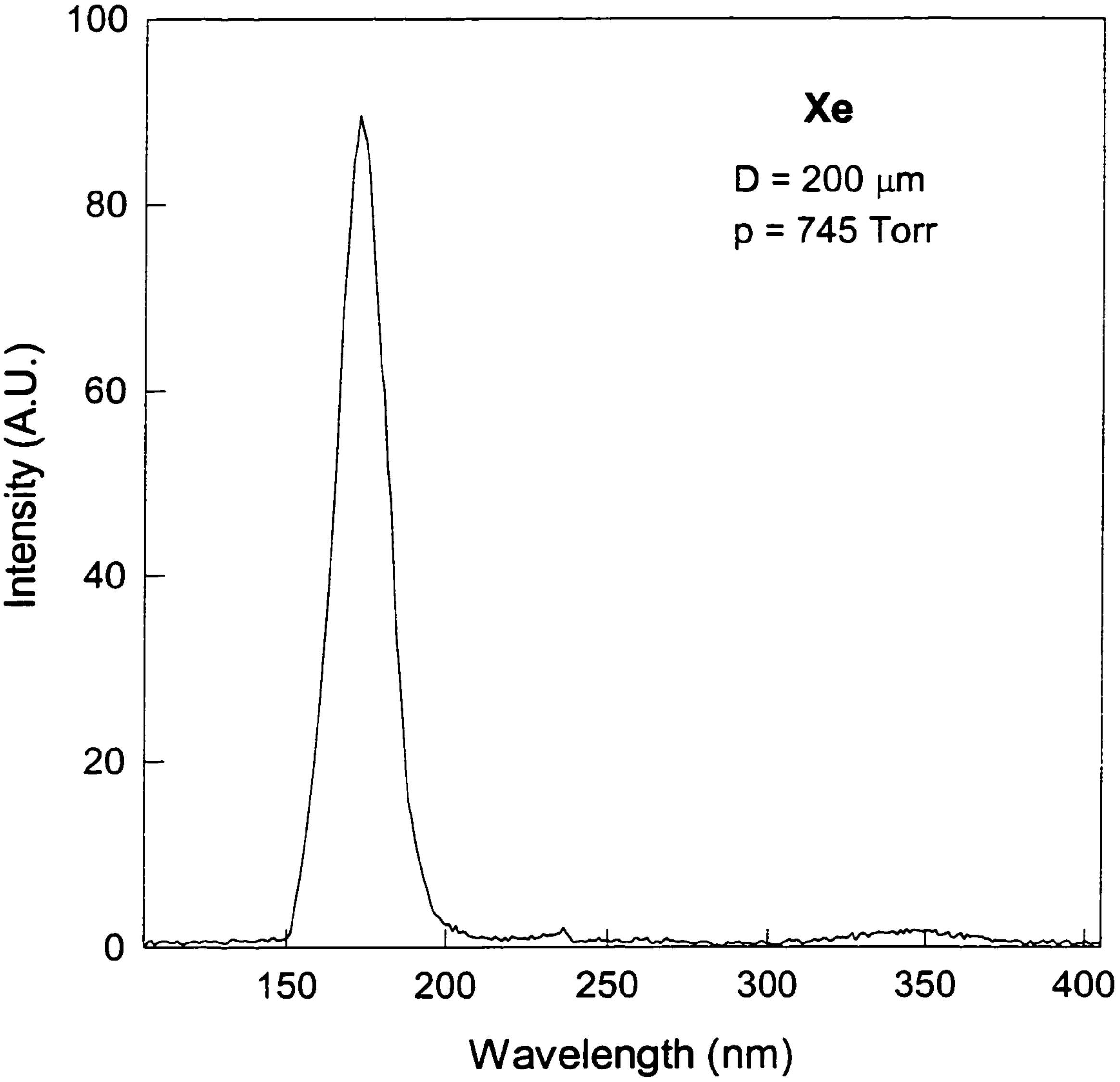

FIG. 6.4. VUV spectrum of discharge in xenon at 745 Torr with cathode hole of 200 μm. The sustaining voltage was 289 V and the current was 5.75 mA.

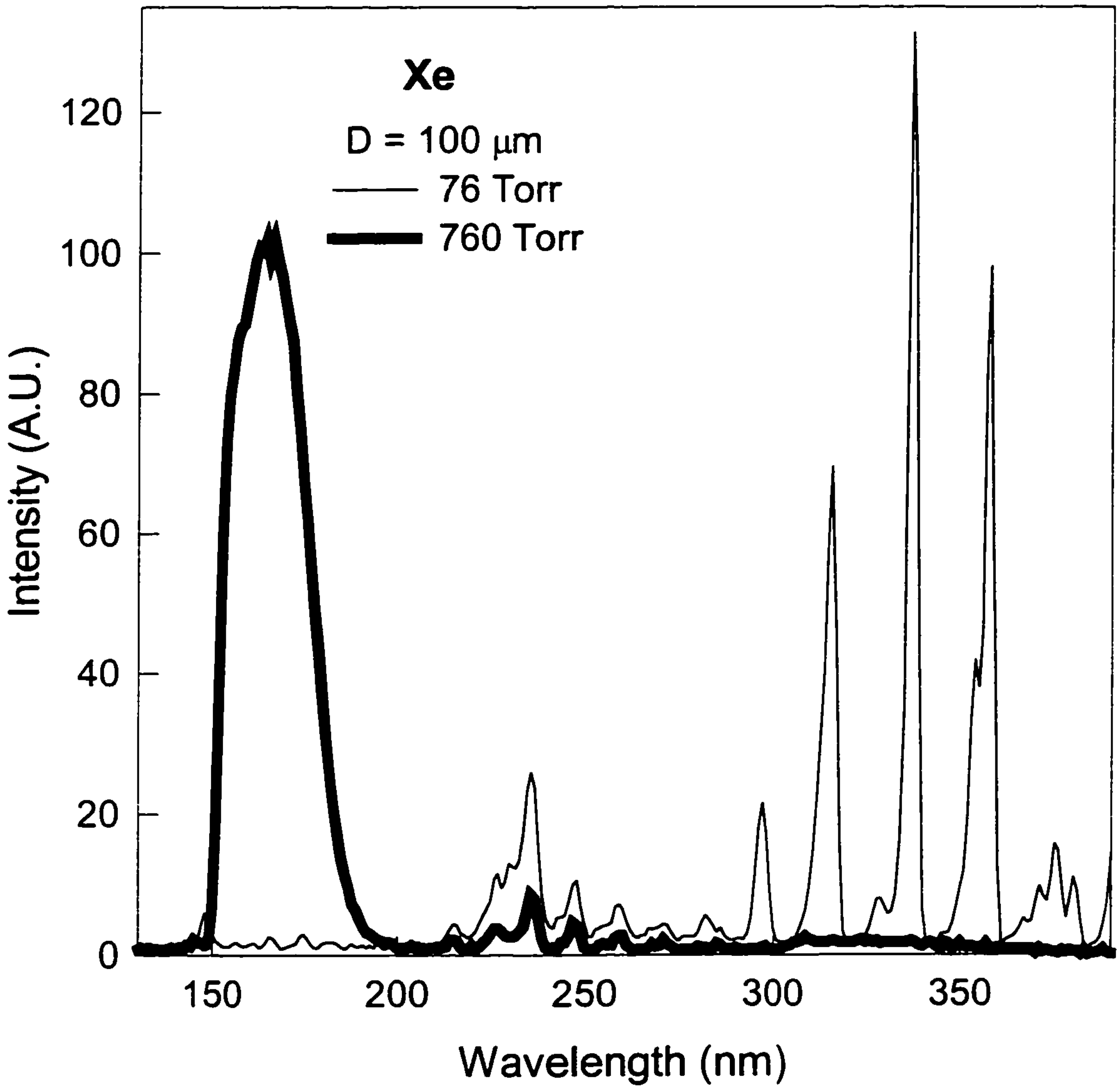

FIG. 6.5. VUV spectra of discharges in xenon at 76 and 760 Torr with a cathode hole of 100 μm. The sustaining voltage for the lower pressure discharge was 427 V and the current was 4.75 mA. For the higher-pressure discharge the voltage was 395 V, and the current wa 4.8 mA.

is shown in Fig. 6.6 for various pressures. At 40 Torr, the 147 nm xenon resonance line dominates the emission spectrum. There are some indications of the first continuum, which extends from the resonance line towards longer wavelength. The second excimer continuum peaking at 172 nm appears at higher pressures. At pressures greater than 300 Torr, it dominates the emission spectra up to the longest recorded wavelength of 800 nm. Similar results were obtained using a blind anode, i.e. the anode hole is closed.

6.2 Electrical Measurements [68-71]

6.2.1 Argon

The emission of the Argon excimer radiation is, besides on the gas pressure, also strongly dependent on the discharge current. The current voltage characteristic of the argon hollow electrode discharge is shown in Fig. 6.7. It has a positive slope over most of the current range from 1 to 6 mA, except for intervals at 3 and 5 mA. The intensity of the excimer line is shown to increase with current, stronger in the range of a negative differential resistivity range of the discharge, than in the positive differential resistivity range. At currents exceeding approximately 2 mA asymmetric glow like and, at higher currents, filamentary discharges reaching out of the cathode hole are observed superimposed to the symmetric hollow cathode and abnormal glow discharges. When this breakdown in discharge symmetry occurs, the current begins to fluctuate, and eventually, at high average currents, current spiking occurs. This effect is more pronounced at high pressures; I-V curves and spectra results are not as reproducible as low pressures.

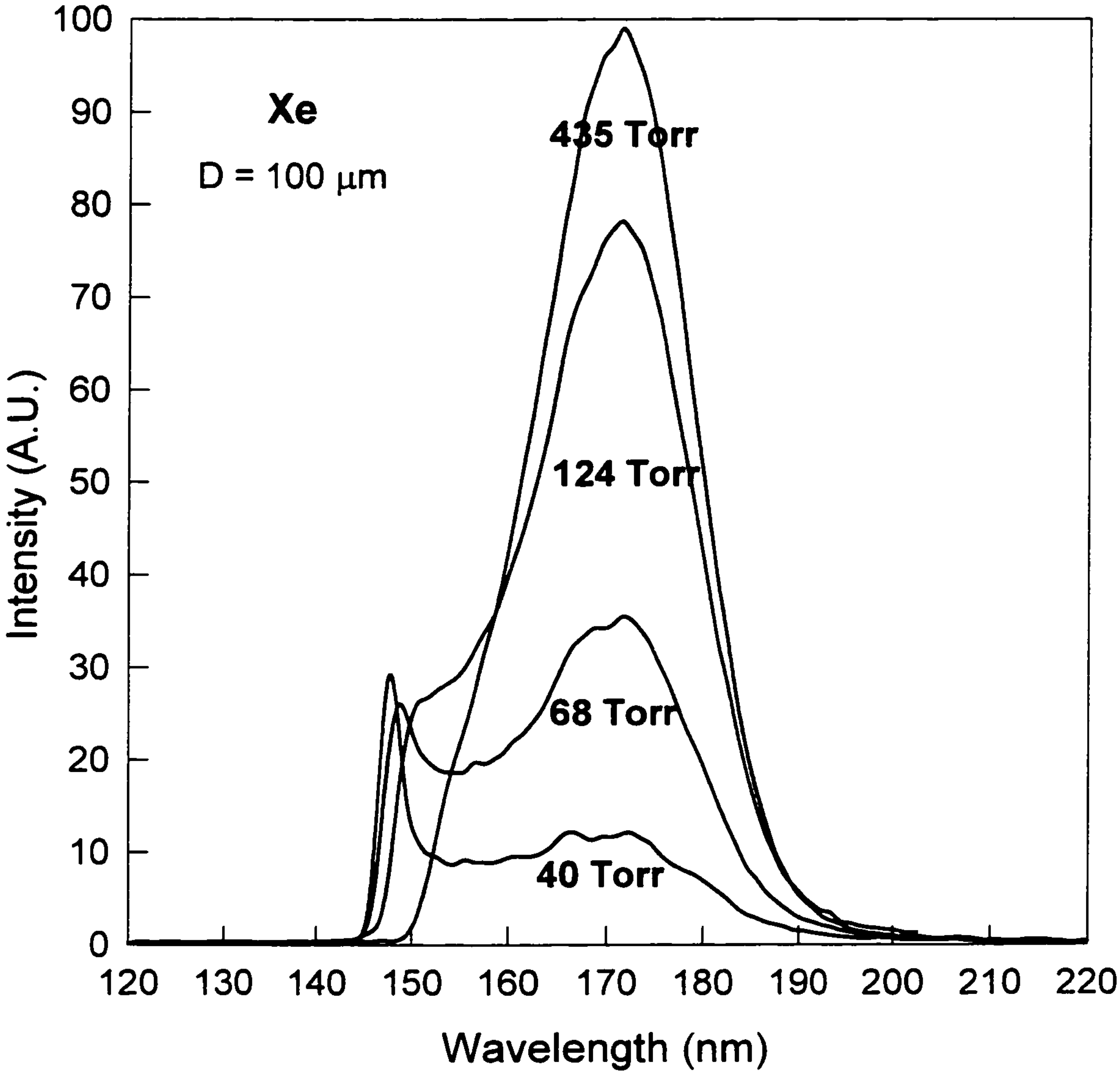

FIG. 6.6. Pressure dependence of the VUV emission spectrum of high pressure microhollow cathode discharges in xenon. The discharge voltage for any of these measurements was between 215 and 235 V, and the current was kept at 3 to 3.3 mA.

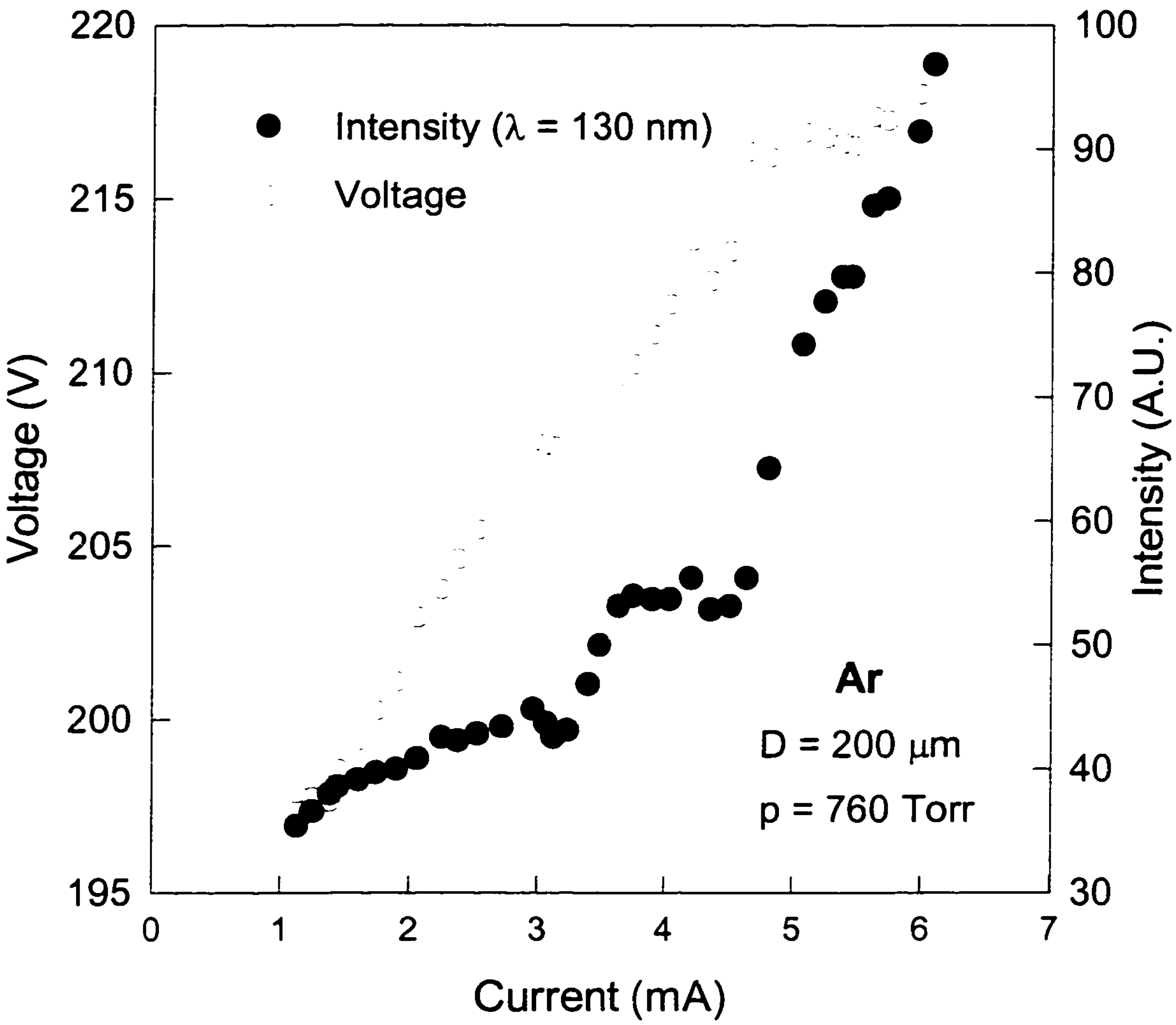

FIG. 6.7. The increase of the peak value of the argon excimer line with increasing current for a cathode hole D = 200 μm. Strongest changes are in current regions where the current-voltage characteristic has a negative slope, indicating the onset of streamer-like discharges.

In order to determine the temporal development of the discharge at high average current, the current voltage traces were recorded by means of digitizing scope (Tek 2232) with a bandwidth of 100 MHz. In the mode where the glow like discharges become apparent, the current shows small fluctuations, with amplitudes of a few per cent of the dc current. The fluctuations, which have an average frequency of 500 kHz, increase with increasing average current. When the current is increased beyond a certain value, which for 200 μm discharges at a pressure of 896 Torr is 4 mA, the dc driven discharge shows a pulsating behavior. This is the range where we see consistently filamentary discharges. The pulse rate is on the order of several hundred kHz with peak currents of up to several hundred mA (Fig. 6.8). The amplitude is proportional to the temporal spacing of the preceding pulse; the pulse width is inversely proportional to the amplitude. Shortest pulse widths of 20 ns were observed by means of a 500 MHz digitizer (Tek 7912 AD) at peak currents of more than 0.5 A.

By reducing the cathode hole diameter to 100 μm we were able to extend the current up to 7 mA (a value which was not exceeded because of concerns about thermal damage of the electrodes) and pressures up to atmospheric and still operate the discharge in a dc mode in argon.

The emission of the argon excimer radiation for a 100 μm cathode opening showed also a dependence on the discharge current. The sustaining voltage, V, of the argon microhollow cathode discharge and the intensity of the excimer radiation for the 100 μm hole are plotted versus the discharge current, I, in Fig. 6.9. Typical sustaining voltages are 200 V.

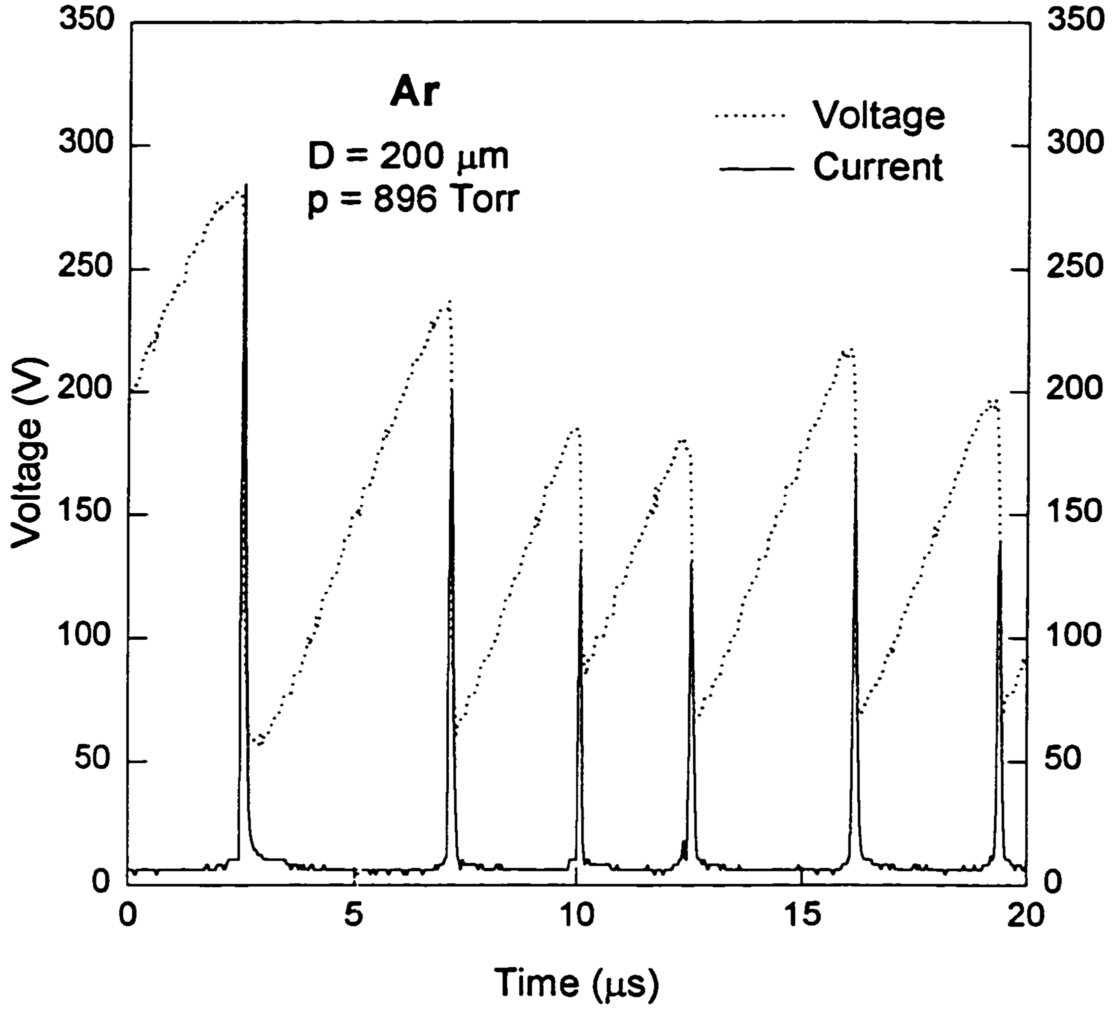

FIG. 6.8. Temporal development of voltage and current of streamer-like discharges in argon at 896 Torr, at an average current level of 4 mA.

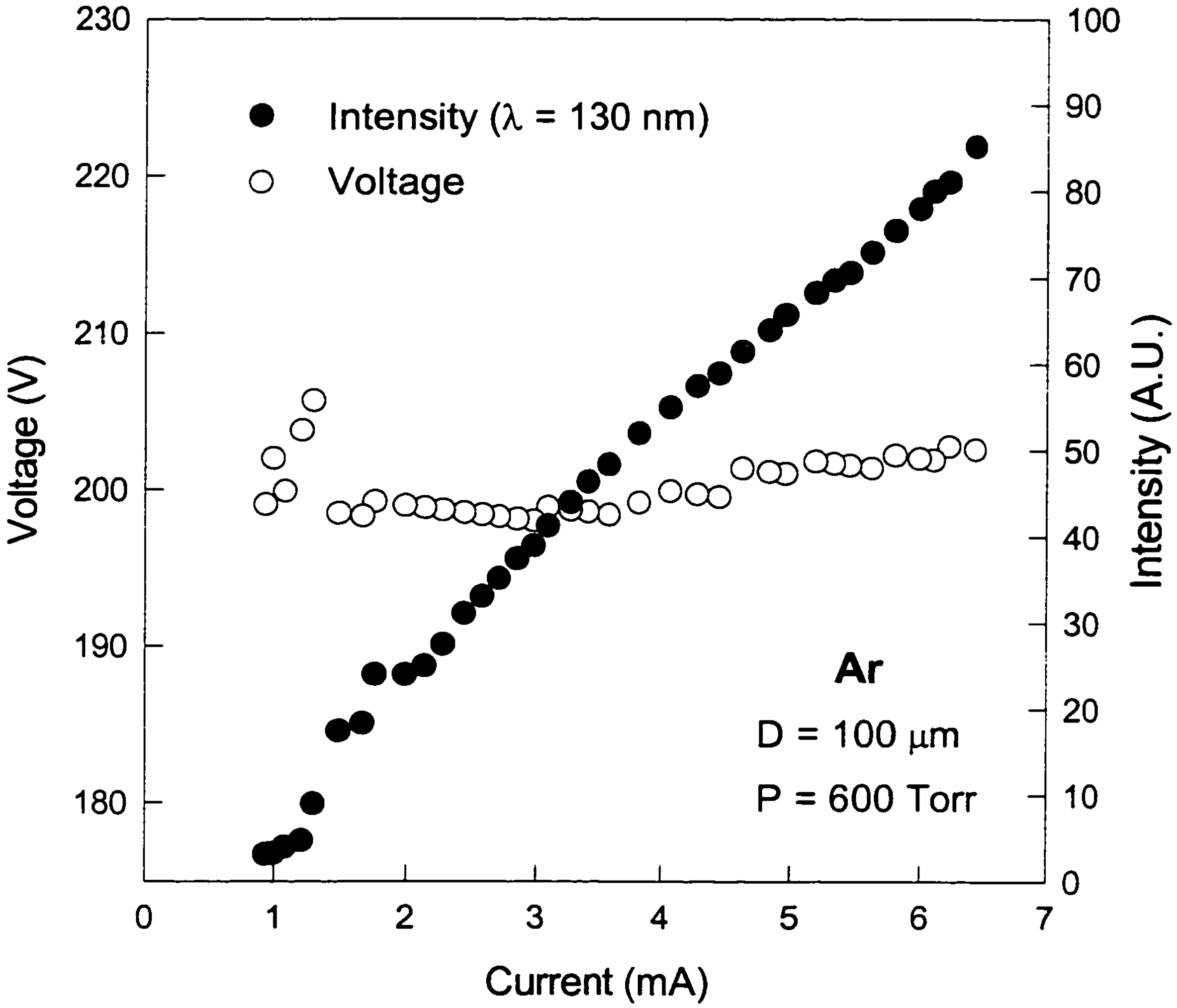

FIG. 6.9. Voltage-current characteristics of microhollow cathode discharges in argon (600 Torr) and corresponding current-dependenc intensities of the argon excimer radiation at 130 nm.

The plot shows two distinctive regions. At low current, the I-V characteristic has a positive slope and the intensity increases slowly with the current. At higher currents, the I-V characteristic is either flat, has negative slope or slight positive slope. In this region, an increase in the current increases strongly the intensity. In the current range of zero and positive differential resistivity the intensity of the excimer line, measured at 130 nm, increases linearly with current. Regions of strong negative differential resistivity, as the one seen in Fig. 6.9 at a current of 1.3 mA, are correlated with a nonlinear increase in excimer emission.

In all argon experiments, the excimer intensity, the current and the discharge voltage were found to be constant with time. The reason for these constant values is that argon was flowed in the system.

6.2.2 Xenon

For a 200 μm cathode opening, temporally resolved measurements at the peak of the xenon excimer line showed that the emission is strongest at the time of the current spikes. However, the emission between the current spikes is still reasonably high. The dependence of excimer emission on current voltage characteristic of the discharge is shown in Fig. 6.10. The intensity of the excimer radiation increases with current whenever the discharge is in a mode with negative differential resistivity. Unfortunately, in this range and at high current the discharge become unstable and results are not as reproducible as in the stable discharge operation. In ranges with positive slope of the current voltage characteristics the intensity increases only slightly when the current is increased.

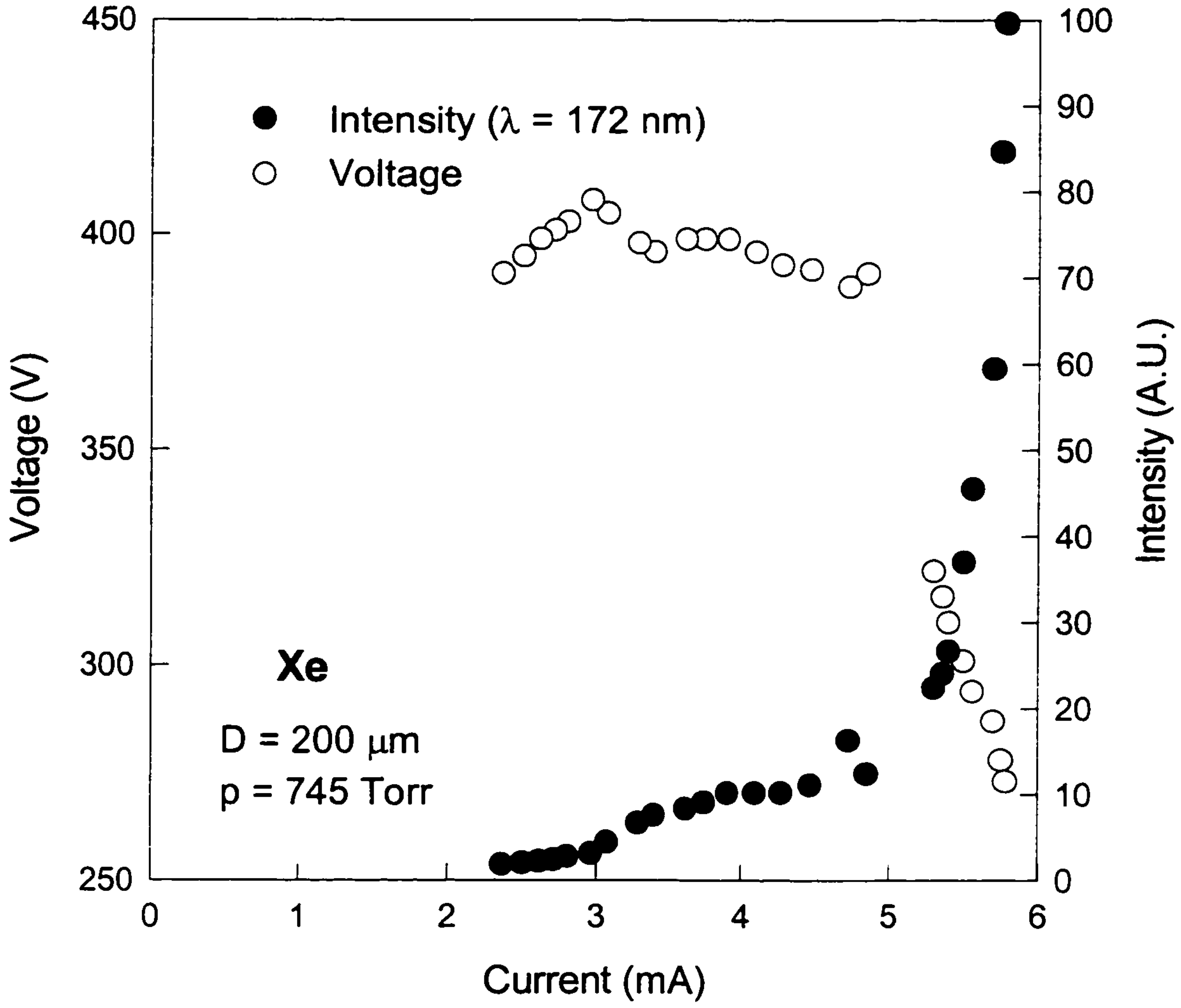

FIG. 6.10. Voltage-current characteristics of microhollow cathod discharges in xenon (745 Torr) and corresponding current-dependent intensities of the xenon excimer radiation at 172 nm.

For currents higher than 4.7 mA the discharge voltage was found to increase with time with a decrease in current even when the supply voltage was kept constant. This change was accompanied with a decrease in excimer radiation. This fact can be attributed to impurities, which play a big role specifically in static environment.

Similar to argon, stable discharges in xenon were obtained in all pressure and current ranges with 100 μm hole diameter cathodes. A reduction in the forward voltage of the discharge from 400 V to 200 V was achieved by cleaning the electrodes. The electrical characteristics of these discharges along with the dependence of excimer intensity on the current are shown in Fig. 6.11.

6.3 Lifetime Measurement

Without electrode conditioning, the excimer radiation intensity was found to drop after 3 minutes from igniting the discharge to approximately 10% of its original value as shown in Fig. 6.12.

Conditioning the electrodes drastically reduced this decay. Running the discharge in argon at low current for half an hour and then evacuating the chamber to 45 mTorr before filling it with gas did this conditioning. After a period of 3 hours of running the discharge in xenon, the radiation intensity was still more than 50% of its original value. Further improvement was attained by running the discharge in xenon at high current and then evacuating to 5 x 10^{-5} Torr. The drop in radiation intensity from xenon discharges was less than 5% over the same time period (Fig. 6.13).

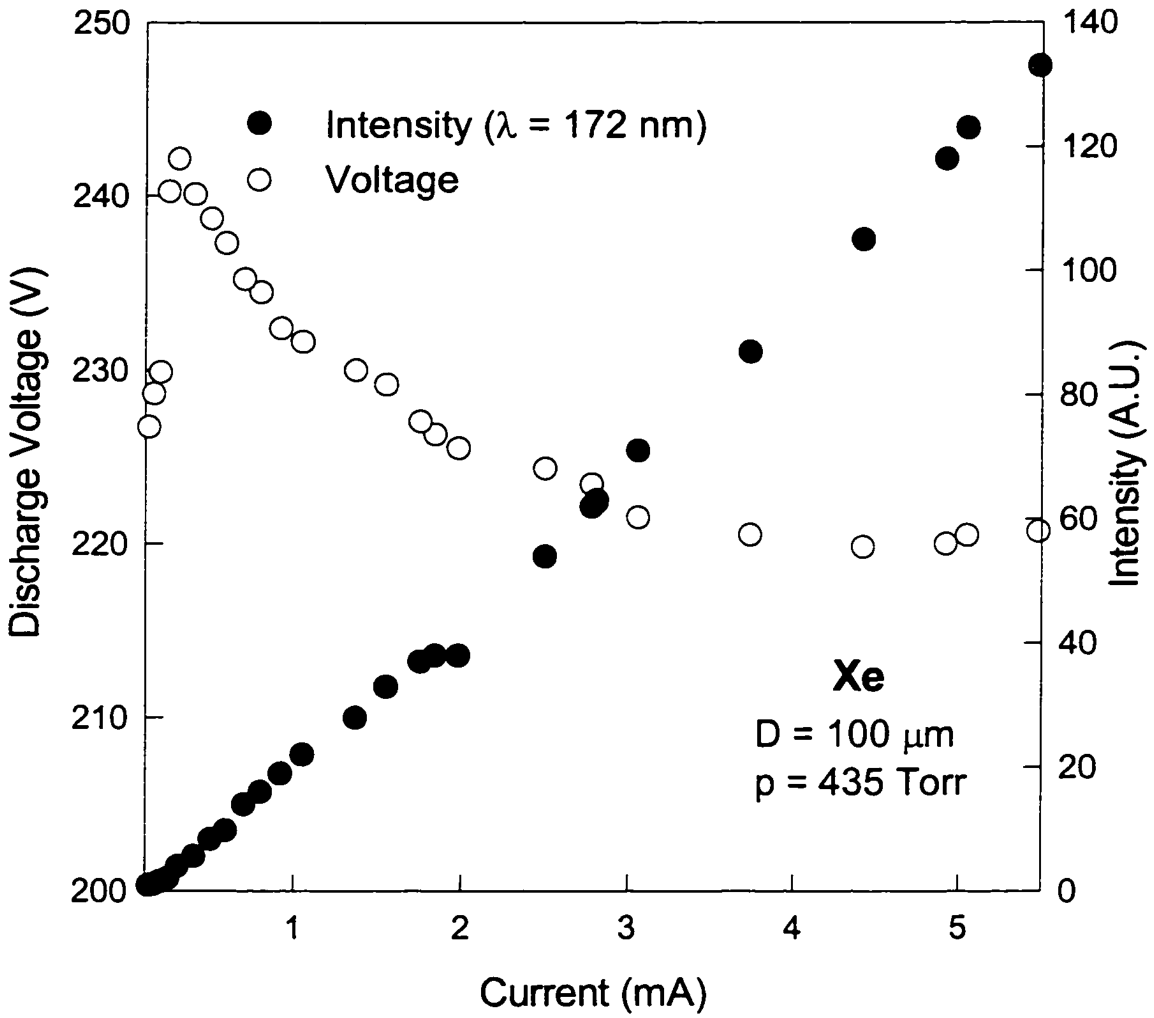

FIG. 6.11. Voltage-current characteristics of microhollow cathod discharges in xenon (435 Torr) and corresponding current-dependent intensities of the xenon excimer radiation at 172 nm.

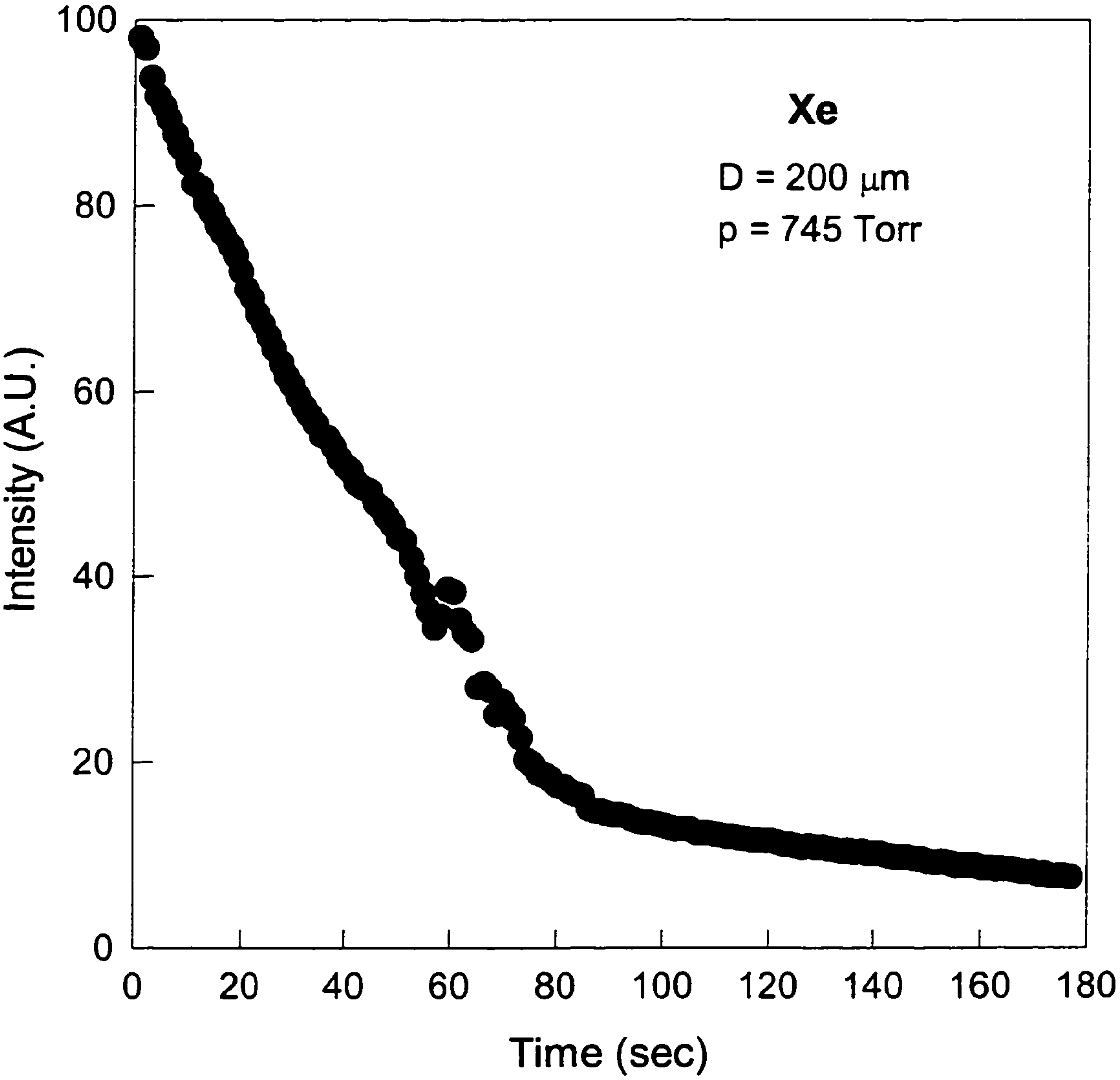

FIG. 6.12. Decay of the excimer radiation intensity with time for discharges with non conditioned samples.

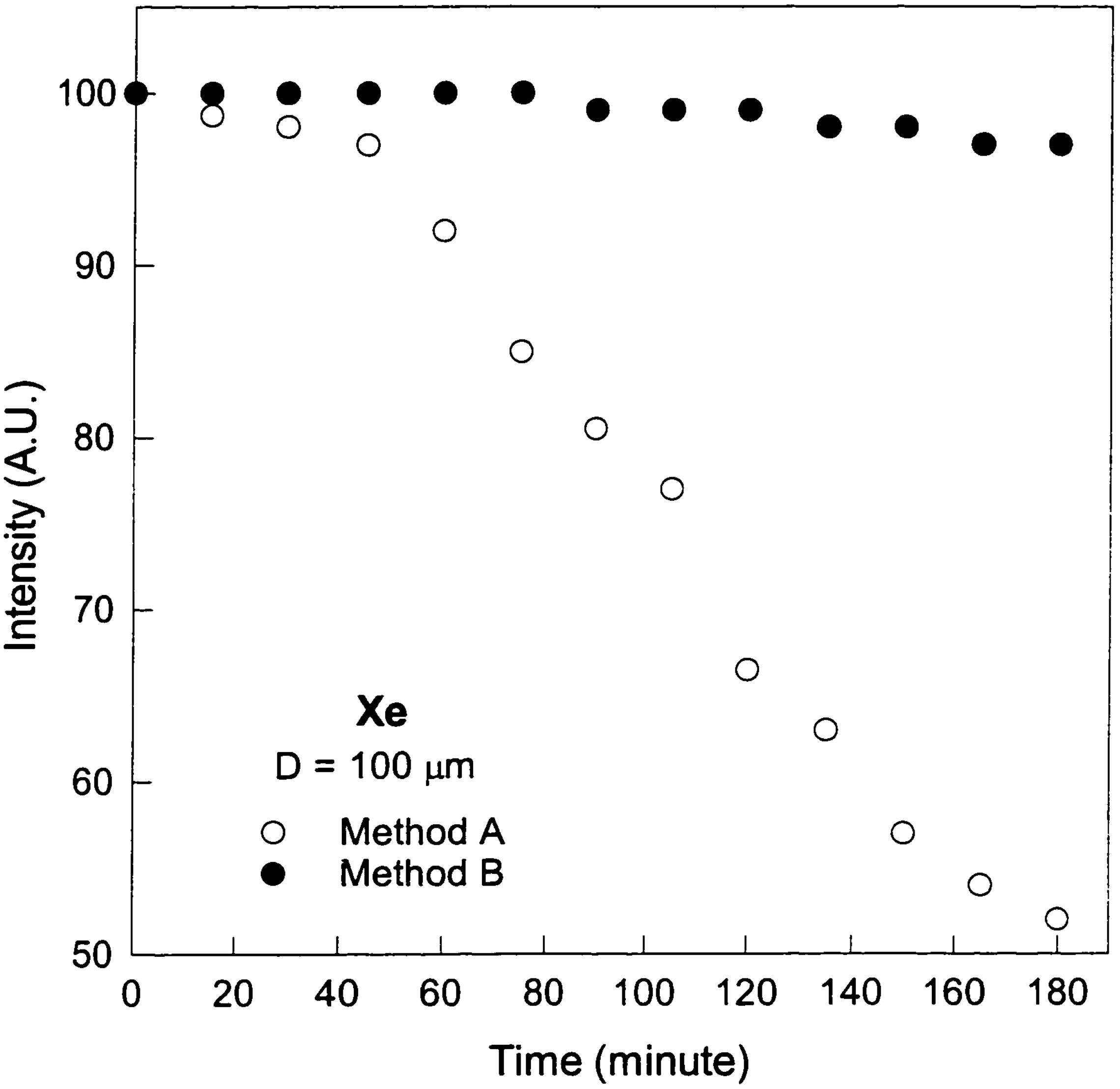

FIG. 6.13. Comparison of the decay of the excimer line in the two applied method for sample conditioning. In method A, the sample was conditioned by running the discharge at low pressure argon and then evacuating the chamber to 45 mTorr for two hours. In method B, the sample was conditioned in xenon at low pressure and higher curren and then evacuated overnight to 5 * 10^{-5} Torr.

6.4 Absolute Measurements [73,74]

The conversion efficiency η (ratio of input electrical power to output optical power) versus pressure obtained by using calibrated sources or radiometer technique, respectively is shown in Fig. 6.14. η increases with pressure and reaches a maximum at 400 Torr; then drops with further increase in the pressure. Using the mercury lamp as standard, this value was found to be 7.5%.

The efficiency of the discharge obtained with the Deuterium lamp is slightly higher than that obtained with the mercury standard, e.g. 9% versus 7.5% at 400 Torr. For radiometer measurement, the efficiency showed a similar pressure dependence as obtained by means of a calibration source method, however, it is lower. At 400 Torr e.g. it is 6%.

From previous results it is known that the emission of the xenon excimer radiation is, besides on the gas pressure, also dependent on the discharge current. For a discharge at 435 Torr the discharge efficiency and the intensity of the excimer radiation are plotted versus discharge current, I, in Fig. 6.15. These results were measured using the radiometer technique. Typical sustaining voltages are 220 V. Radiation intensity increases linearly with the current and the efficiency strongly increases with current up to 1mA and then stays in the range between 5.5% and 7% for higher currents. This allows linear control of intensity with current.

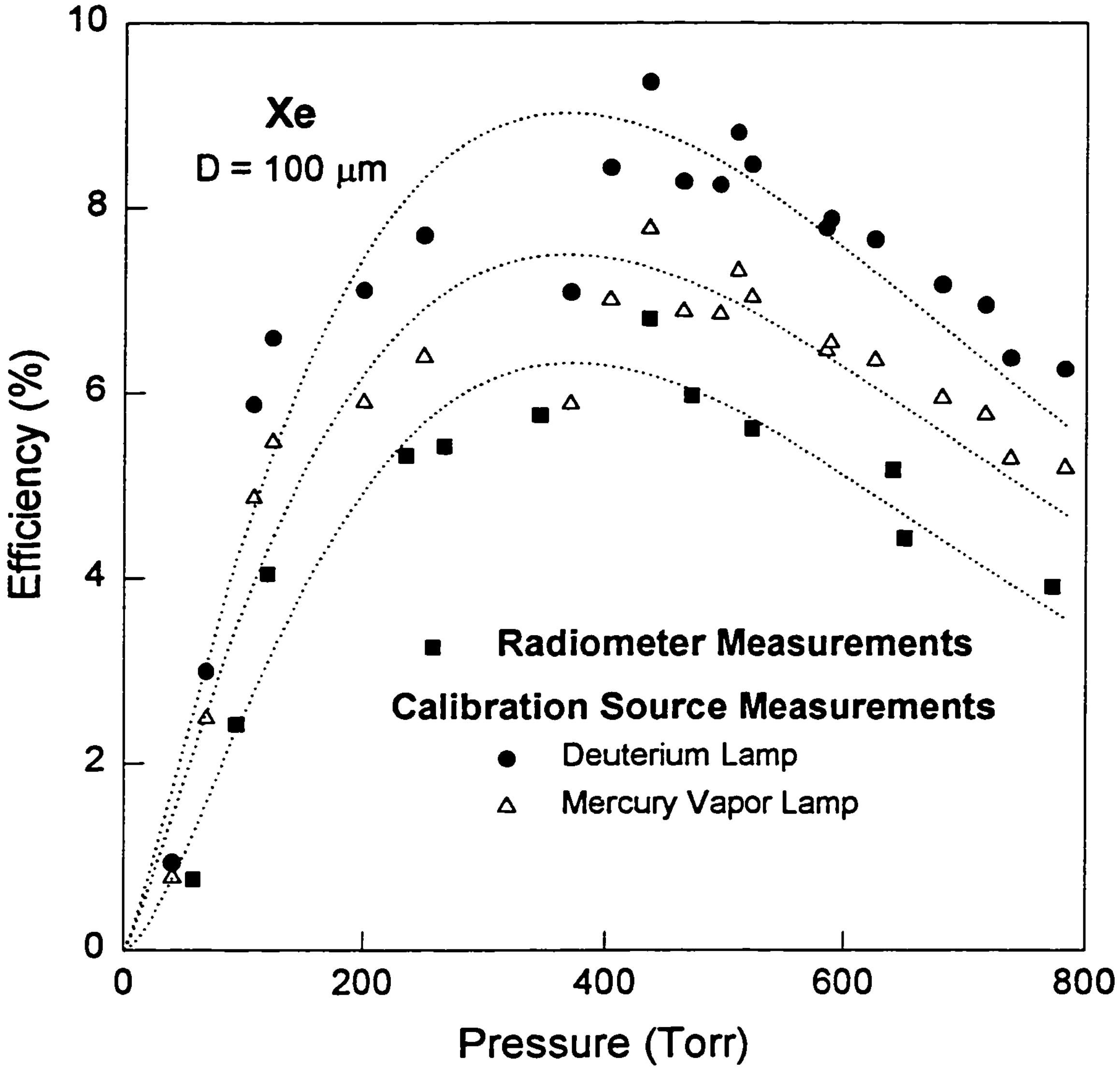

FIG. 6.14. Measured efficiency of the xenon excimer radiation versus pressure. The discharge current in these measurements was kept at 3 to 3.5 mA.

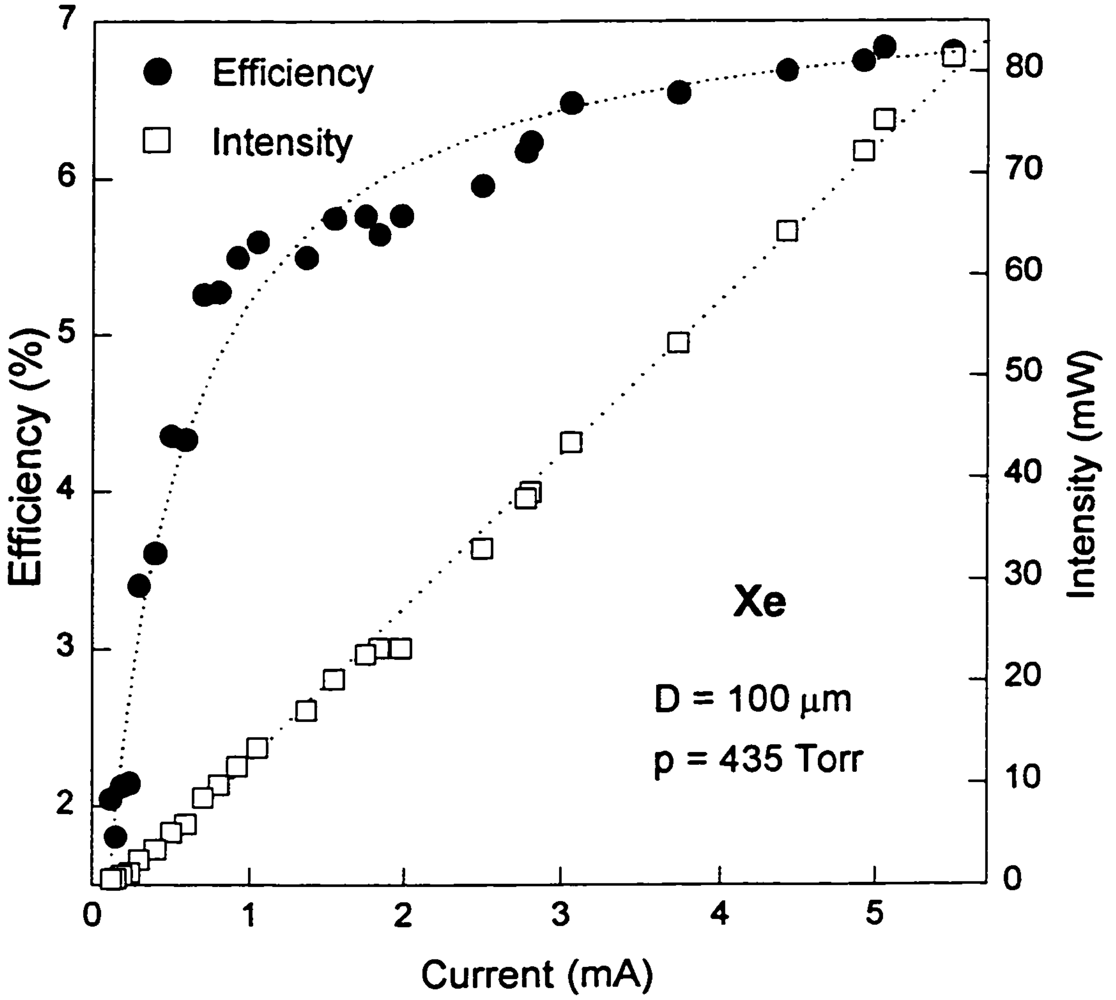

FIG. 6.15. Intensity of the xenon excimer radiation versus discharge current and corresponding efficiency. The efficiency was measured using the radiometric technique.

CHAPTER VII

DISCUSSION

7.1 Pressure and Current Dependence of Excimer Emission

Spectral behavior of excimer radiation in MHCD in xenon (Fig. 6.6) shows a similar pressure dependence as that in silent discharges (Fig. 7.1 [14]). At low pressure, the 147 nm line dominating the spectrum is the xenon resonance line, corresponding to transitions from the $^3P_1$ state to the $^1S_0$ ground state. The first continuum peaking at 150 nm results from transitions from vibrationally excited singlet $^1\Sigma$ and the triplet $^3\Sigma$ excimer states to the repulsive ground. By increasing the pressure, the vibrational relaxation of these states is faster than their decay. Transitions from the lowest vibrational states of these excimer states are responsible for the generation of the second continuum at 172 nm.

The peak of the excimer line in argon was observed at 130 nm. Due to a rapid change of the transmittance of the MgF_2 window between 125 nm and 130 nm (51% and 55%, respectively) and a similar reflectivity change of the MgF_2 coated mirrors inside the monochromator, the actual peak could be at a slightly shorter wavelength. This uncertainty is reflected in data of other groups, which report the maximum Ar_2 excimer emission in the range 126-130 [6,21,26].

7.1.1 Electron Energy

The emission of excimer radiation from high pressure hollow cathode discharges indicates the presence of a large concentration of high energy electrons in these discharges. Electrons with energies greater than 8 eV are required for the generation of excited and ionized rare gas atoms the precursors

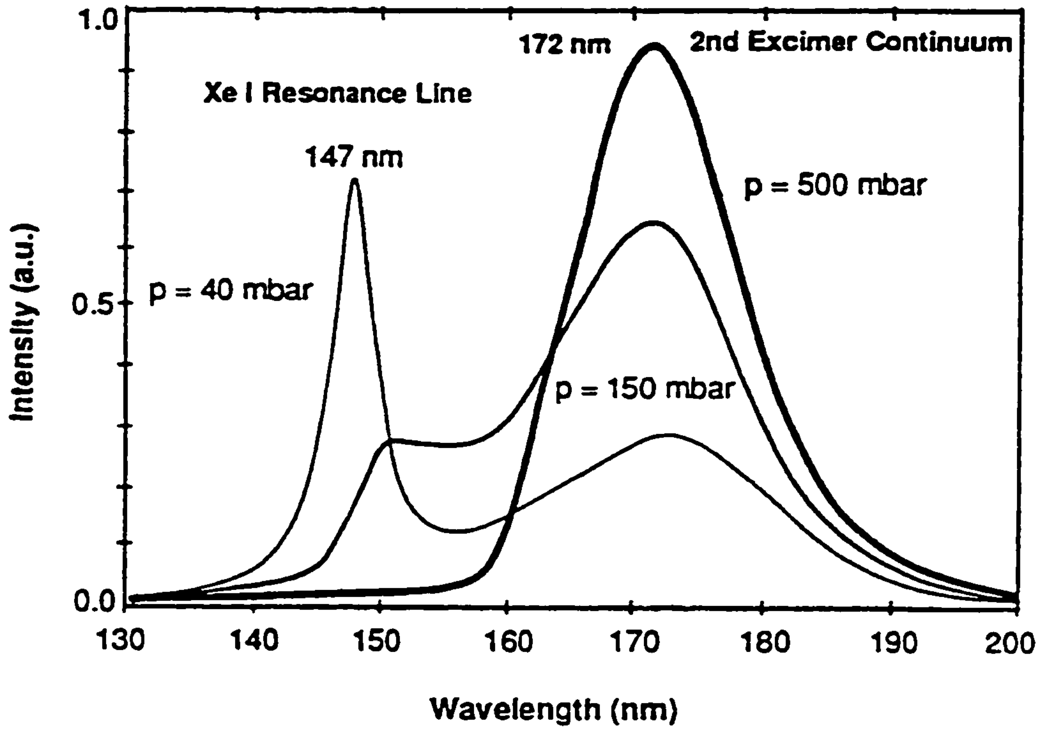

FIG. 7.1. Pressure dependence of the xenon spectrum in silent discharges [14].

of excimers. Energy of lowest excited states and the ionization potential are 11.6 ,15.76 eV and 8.3,12.1 eV for argon and xenon respectively.

The presence of high energy electrons is not too surprising since electron energy measurements in hollow cathode discharges at low pressure [49] and in the negative glow of low pressure discharges [54] have shown the presence of electrons with energies even greater than 100 eV. The presence of ionic lines, can be explained by an electron energy distribution which contains, at least at lower pressures, a large concentration of electrons with energies greater than 30 eV and even higher, able to excite atoms to the required upper level. One possible explanation for the observed decrease in intensity of the ionic lines with increasing pressure is a reduction of the density of electrons in the high energy tail of the electron energy distribution in the discharge when the pressure is increased. A second possible reason, might be the increase in the rate of three body processes, with increasing pressure, particularly the ones that lead to the formation of molecular ions, the precursor to excimers. It is not unlikely, that the concentration of electrons greater than 30 eV is not affected by the increase in pressure, but that the radiative decay of ions, excited by these electrons, competes at high pressure with an increasing collisional deexcitation of these states.

7.1.2 Excimer Modeling

In order to explain the observed pressure dependence of the radiant power of the excimer emission, a simple steady state rate equation model has been used. The two rate equations describing the generation of excited xenon atoms Xe^* and molecules Xe_2^* are:

$$\frac{d[Xe_2^*]}{dt} = [Xe^*][Xe]^2 k_R - \frac{Xe_2^*}{\tau_2} = 0 \tag{7.1}$$

$$\frac{d[Xe^*]}{dt} = \frac{P'}{w} - [Xe^*][Xe]^2 k_R - \frac{Xe^*}{\tau_1} = 0 \tag{7.2}$$

where P' is the deposited power in a unit volume of the discharge, w is the mean energy necessary to produce one excited xenon atom, k_R is the rate coefficient for the three body collision ($\approx 5\text{x}10^{-32}$ cm^6/s [75]), τ_1 is the apparent lifetime of the excited xenon atoms ($\approx 1\mu$s [68]) and τ_2 is the lifetime of the xenon excimer state ($\approx 0.5\ \mu$s [37]).

The xenon excimer concentration, neglecting diffusion, is derived from eqs. 7.1 and 7.2:

$$[Xe_2^*] = \frac{P'}{w} \frac{k_R[Xe]^2}{\left(k_R[Xe]^2 + \frac{1}{\tau_1}\right)\frac{1}{\tau_2}} \tag{7.3}$$

Using the ideal gas law, we can express the excimer concentration in terms of pressure:

$$[Xe_2^*] = \frac{\tau_2 P'}{w} \frac{k_R p^2}{k_R p^2 + k^2 T^2 / \tau_1} \tag{7.4}$$

where p is the pressure, k is the Boltzmann constant and T is the gas temperature.

If we assume that each excited xenon excimer will decay radiatively, the efficiency can be calculated as:

$$\eta = \frac{[Xe_2^\bullet] * h\nu / \tau_2}{P'} = \frac{k_R p^2}{w(k_R p^2 + k^2 T^2 / \tau_1)} * h\nu \tag{7.5}$$

The theoretical curve obtained this way is shown in Fig. 7.2. It follows the experimental curve up to 400 Torr at T = 300 K. Absolute values, however, differ considerably from experimental ones. If we e.g. assume a w-factor 3 times the threshold energy for the generation of excited states, the efficiency is calculated as 30% to 40%, compared to 6% to 9% obtained experimentally. This difference in absolute values as well as the deviation between the two curves may be due to diffusion losses, which were neglected in our calculation. Another reason for these discrepancies is photoionization of the Xe_2^* excimers [27], which is not considered in our model.

7.1.3 Effect of current

The increase of excimer radiation with the increase of current is due to an increase of the electron density n_e with current. The two different slope of the intensity current characteristics shown in Fig. 6.9, Fig. 6.11 and Fig. 6.15 is possibly due the different modes of the discharge. At low current, the discharge is in the Townsend mode with a low ionization efficiency. Increasing the current increases the discharge efficiency due to the onset of the hollow cathode effect.

7.2 Effect of Contaminants

7.2.1 Increasing the Discharge Voltage

The reason for the increase in voltage with time can be seen from the consideration of the nature of contaminants. Almost all simple compounds, such as water vapor and ammonia, form negative ions by attachment, as does oxygen itself. Negative ions are not efficient ionizers so that once an electron has been

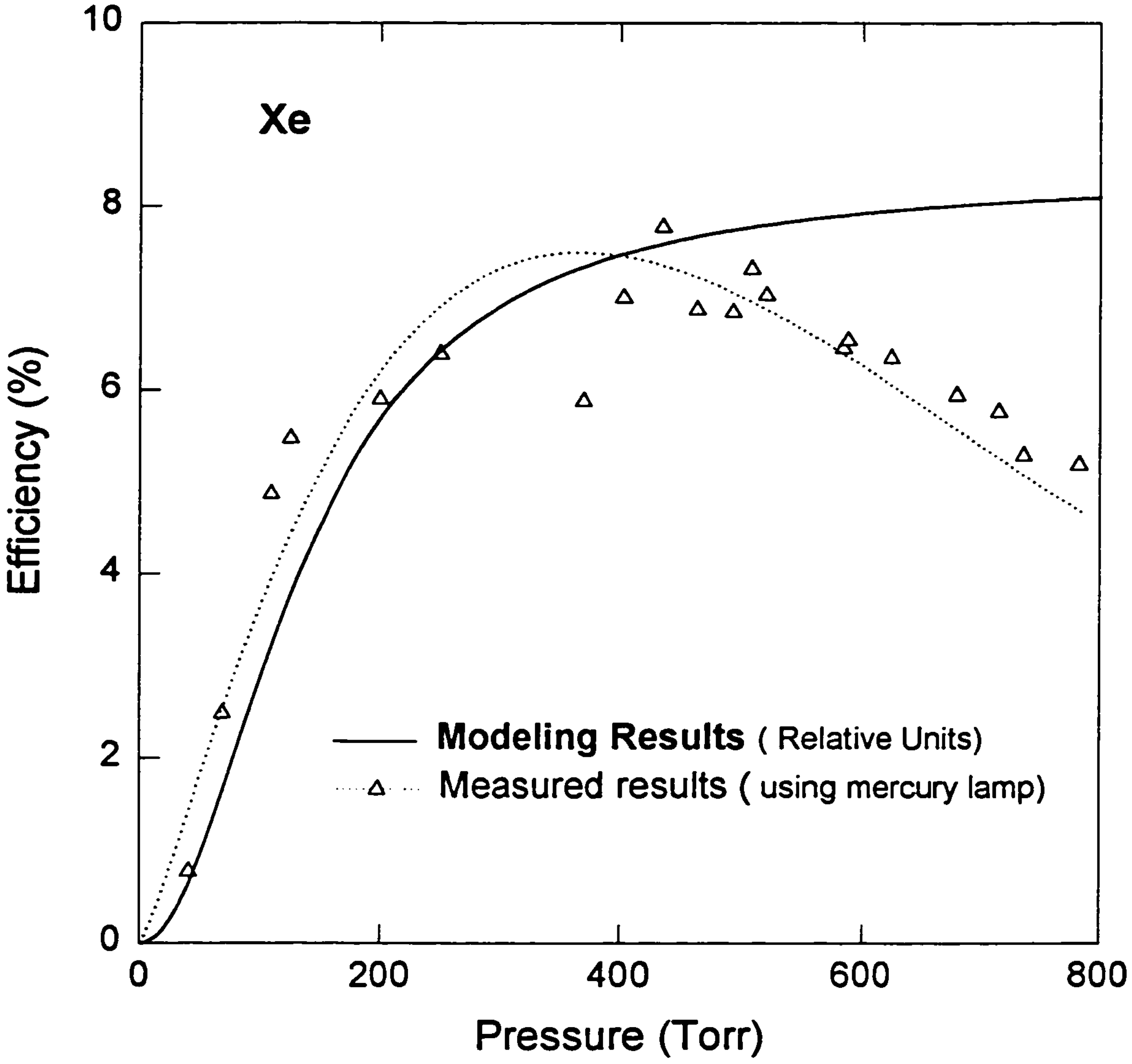

FIG. 7.2. Comparison of the results of the experiment and the model. Model results are shown as relative values.

attached to a contaminant molecule it can no longer contribute to the ionization process. Thus, water vapor and oxygen in particular tend to lower the effective ionization coefficient of a gas. The effect is the increase of the discharge voltage. For a constant supply voltage, the increase of the sustaining voltage is accompanied by a decrease in the current.

Evolution of contaminating gases from surfaces may be expected to increase exponentially with temperature. Since the temperature will for many components be a linear function of current, it follows that the rate of evolution is proportionally to e^{ki} where k is a constant and i is the current. The rate of removal of the contaminants, on the other hand, is largely dependent on their ionization rate by the discharge and being ionized by the discharge and the absorption by the anode, cathode or the walls. This clean up process is therefore likely to be proportional to the current [76]. Hence, as the current is increased, the rate of contamination evolution rises exponentially whereas the rate of removal only rises linearly. At the high current range the rate of evolution of contaminants will exceed the rate of their removal and the concentration of the contaminants will rise. These contaminants will cause an increase in the sustaining voltage with time. At a current of 4.6 mA in Fig. 6.10 it seems that balancing between contaminant evolution and removal was achieved and this is why there is no further increase in the discharge voltage with time.

The reason for the high discharge voltage for the spectra of Fig. 6.5 could be explained by the presence of contaminant in the discharge causing an increase of the voltage as discussed in the previous paragraph. Another important reason, since molybdenum is an active absorber of impurity gases a gas film can cover the molybdenum electrode. This gas film has a relatively poor secondary emission causing an increase in the sustaining voltage of the discharge [76].

7.2.2 Reducing Excimer Generation

The presence of impurities plays a big role in excimer formation and can cause a big change in the development of excimer continua. The decrease in the excimer radiation intensity with time in Fig. 6.12 can be attributed to the excess presence of contaminants.

Based on our spectral measurement shown in Fig. 6.5 and Fig. 6.6 an attempt will be made in the following to provide an explanation for this role. At low pressure the presence of impurities reduces the generation of the xenon excited states. Another effect of the presence of impurities is collisional quenching of the excited rare gas atoms [77], the precursors of the excimer. Hence, at low pressure the resonance line is not very pronounced in the spectrum of Fig. 6.5. Since the amount of impurities is only dependent on the electrodes and their surface by increasing the pressure the ratio of impurities to the xenon gas will be reduced. This is a possible explanation for the appearance of the excimer second continuum at pressures of 200 Torr. At these pressures the impurity line has decreased with an increase of the excimer line. This means that the energy deposited in the discharge is used more and more for the formation of the xenon excimers. However, as seen in Fig. 6.5 impurity lines are still present at 760 Torr. Even at atmospheric pressure, we still see an increase in excimer intensity with pressure because of the presence of impurities. Quenching of the excited states by impurities is still occurring. The first continuum was not observed since at low pressure the population of the excited excimer state is very low. At high pressure, when the population begins to increase the pressure was high enough for the relaxation of the vibrational excited states to occur faster than their radiative decay.

In the case of the conditioned system illustrated in Fig. 6.6 the effect of impurities is very small and most of the energy deposited in the discharge contribute in the formation of the excited xenon states and consequently the excited molecular xenon. Moreover, quenching of the excited atoms by impurity traces is now very limited. This is why we see strong emission of the resonance line at low pressure accompanied by the first continuum. At higher pressures, the excimer formation dominates the kinetics of the discharge with negligible quenching by impurities. This may explain the higher intensity of excimer radiation in the cleaner system.

Since xenon is heavier than argon, it seems that conditioning with xenon (method A) remove more efficiently the impurity layers from the surface of molybdenum than with argon (method B). This can explain the much longer lifetime of excimer radiation in conditioning with xenon compared to that with argon (Fig. 6.13). Another possible reason is that the better evacuation applied in method B helped to remove almost all impurities from the system. Thus, their effect on the excimer generation was very limited.

With flowing argon it was possible to keep excimer radiation constant with time along with discharge voltage and current. An increase of the flow caused an increase in the intensity of radiation. Two facts are possibly the reason for such effect. The high flow of the gas cools the system and hence improves excimer formation. Another reason would be that flowing the gas carries away contaminants.

7.3 Absolute Measurements

The three sets of measurements showed a similar pressure dependence with a slight difference in the values depending on the method used. The lowest absolute values were obtained from the radiometric measurements. This is, in our opinion, due to water vapor absorption in the air gap, which was neglected in our calculation. The water vapor absorption coefficient has a continuum from 145 to 186 nm with a peak of 124 cm^{-1} at 165.5 nm [78]. Absolute measurements were performed only with xenon. It is very difficult to find a calibrated source near the argon excimer line. Moreover, the detection system responsivity drops very much at the spectral range of the argon excimer line.

The mercury lamp showed lower values than the deuterium lamp measurement. This difference could be explained by the error in considering the mercury lamp as point source. From Fig. 7.3 [79], we can conclude that the distance to a light source should be greater than five times the largest dimension of the source for point source assumption. For a distance 10 times the source radius (5 times the diameter), the error from using the point source approximation is exactly 1 %. This condition is fulfilled in the case of the Deuterium lamp and

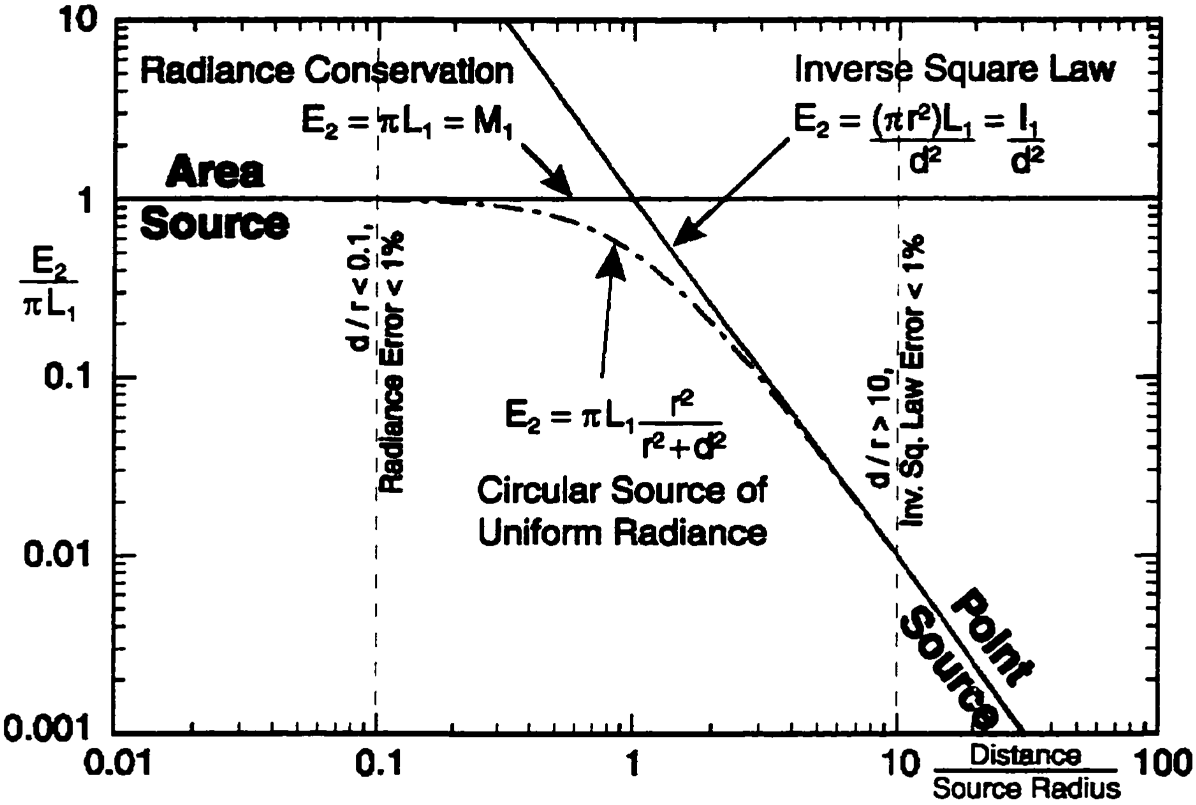

FIG. 7.3. Inverse square law approximation error [79].

the discharge where the diameter of the source is much less than the distance from the source to either the monochromator or the radiometer detector. In the case of the mercury lamp the ratio between the distance and the longest dimension of the lamp, which is in this case its length is 1.2. This ratio is expected to cause a larger error in the measurement.

CHAPTER VIII

SUMMARY AND CONCLUSIONS

Excimer emission is based on the formation of excited molecular complexes (excimers) and the transition from the bound excimer state to a repulsive ground state. In order to generate excimer radiation at high efficiency in a gas discharge two conditions need to be satisfied. The electron energy distribution needs to contain a sufficient concentration of electrons with energies required for the generation of the precursors of the excimers, which for rare gas dimers are excited and ionized rare gas atoms. Secondly, since the formation of the excimer is a three body process, the pressure needs to be high, between 0.1 to one atmosphere. Both conditions can only be satisfied simultaneously in non-thermal plasmas.

There are two ways to generate non-thermal plasmas: either by operating on a short enough time scale such that thermalization of the electrons is prevented, or by operating on a small enough spatial scale, e.g. in the cathode fall of a gas discharge. The first concept utilizes barrier discharge or silent discharges for excimer lamps. The second type of non-thermal discharges is hollow cathode discharges. In these discharges the cathode opening has a diameter on the order of twice the width of the cathode fall and the negative glow. The range of operation of hollow cathode discharges can be extended to higher pressures by reducing the hole diameter. A reduction of the diameter to 100 μm has allowed us to operate direct current hollow cathode discharges in argon and xenon up to atmospheric pressure.

Microhollow cathode discharge (MHCD) has been found to be an intense source of xenon and argon excimer radiation peaking at wavelengths of 172 nm and 130 nm, respectively. The discharge operation and the intensity of the excimer radiation are strongly affected by the presence of impurities on the electrode surfaces. Conditioning the electrodes before running the discharge helped in cleaning the surfaces and enhancing excimer formation. Excimer radiation scales linearly with current, which makes analog control of excimer emission with semi conductor devices possible.

Efficiencies of 6% to 9% have been achieved. This efficiency is comparable to values of dielectric barrier discharges. A single discharge at a pressure of 435 Torr, with a current of 3.12 mA and a forward voltage of 218 V, emits ≈ 53 mW of VUV radiation concentrated in the spectral range from 150 to 190 nm.

Further increase of the efficiency seems to be possible; according to our modeling results, efficiencies of 30% to 40 % may be obtainable. In order to obtain information on the processes, which determine the radiative emission in the VUV, measurements of the spatial distribution of the excimer emission has to be performed. In addition the temporal development of electrode vapor concentration and its effect on the excimer emission need to be studied using optical and mass spectroscopic methods.

We have shown an increase of excimer radiation of more than an order of magnitude with flowing argon. All absolute measurements were performed in static xenon discharges. Flowing xenon may increase the efficiency of radiation.

Studies of excimer radiation in cooled discharge tubes [44] have shown that the gas temperature determines the intensity of the excimer emission to a large extend. A large increase in excimer radiation was reported by liquid nitrogen cooling of the discharge tubes. We expect an increase of excimer generated from the MHCD if the discharge will be cooled. A good way for cooling the system is by forcing xenon in the system with high flow rate similar to gaseous lasers.

In our experiment, the intensity of excimer was higher than 95% of its original value after 3 hours. We expect that the lifetime of the excimer intensity in this system will not be less than hundred of hours. By using very pure gases, flowing the gases and applying methods of continuous purification the efficiency of excimer generation along with lifetime of radiation are expected to be improved.

The fact that efficient fluorescence of xenon excimers could be obtained from a simple microhollow cathode configuration suggests that all mixtures in which fluorescence was obtained under other excitation mechanisms can also be generated in MHCD. Moreover, the high electron energy in the discharge can also be utilized for efficient excitation of other atomic or molecular systems that do not lead to excimer formation. Examples are ozone generation, flue gas cleaning, pollution control, etc.

Preliminary results of experiments with microhollow cathode discharge arrays have shown that the hollow cathodes can be spaced at distances equal to the hole diameter [80-81]. Under these conditions and assuming that 50% of the radiant power can be used to irradiate a target, the radiant emittance (power density) obtainable based on the single hole result is $\approx$65 W/cm^2. This is to our knowledge more than an order of magnitude higher than any other excimer lamp and would largely extend the range of industrial applications for these kind of lamps.

The presented discharge can be considered as a small scale model of much larger flat panel excimer lamp using multiple discharges in parallel. These low costs, excimer lamps provide an interesting and promising candidate to commercially available excimer lamps based on dielectric barrier discharges. A microhollow cathode discharge excimer lamp has the potential to operate dc, at voltages of few hundred volts. The simplicity of the electrode geometry, which can be generated by means of thin film technology, may allow the formation of thin, almost two dimensional excimer lamps which can be easily adapted to any application. The lamp can be wrapped around the material, which is to be treated with UV or VUV radiation.

References

1. Ian. W. Boyd, J. Y. Zhang and P. Bergonzo, SPIE **2403**, 290 (1995).
2. U. Kogelschatz, Appl. Surf. Sci. **54**, 410 (1992).
3. A.Roth, Rad Tech Report, 21 (1996).
4. H. Esrom and U. Kogelschatz, Appl. Surf. Sci. **54**,440 (1992).
5. B. Elliasson and U. Kogelschatz, Appl. Phys. B **46**, 299 (1988).
6. U. Kogelschatz, Pure and Appl. Chem. **62**, 1667 (1990).
7. Heraeus Noblelight, Heraeus Excimer UV Lamps, catalogue.
8. Osram Planon web site, www.osram.de/txt/aktuell/planone.htm.
9. Osram Germany, Planon Lamp, catalogue.
10. U. Kogelschatz, Proc. Tenth Int. Conf. On Gas Discharges and their Applications, Swansea, 1992, Invited lectures, 972.
11. H. Esrom and U. Kogelschatz, Appl. Surf. Sci. **46**, 158 (1990).
12. P. Bergonzo, P. Patel, I. W. Boyd and U. Kogelschatz, Appl. Surf. Sci. **54**, 424 (1992).
13. P. Bergonzo and I. W. Boyd, J. Appl. Phys. **76**, 4372 (1994).
14. U. Kogelschatz, Proc. XX. Int. Conf. On Phenomena in Ionized Gases, Pisa, 1991, Invited papers, 953.
15. I. W. Boyd and J. Y. Zhang, Nucl. Instr. and Meth. In Phys. Res. B **121**, 349 (1997).
16. H. Esrom, J. Y. Zhang, and U. Kogelschatz, Polym. Surf. and interface, 1 (1996).

17. J. Y. Zhang, H. Esrom, U. Kogelschatz, and G. Emig, Appl. Surf. Sci. **69**, 299 (1993).
18. S. Habibi, M. Totsuka, J. Tanaka, T. Kinoshita and S. Matsumoto, J. Vac. Sci. Technol. B **13**, 247 (1995).
19. U. Kogelschatz, Non Thermal Plasma Techniques for Pollution Control, Springer, Berlin, 339 (1993).
20. McClellan AFB SERDP, Non Thermal Plasma Destruction Technology, Web site www.mcclellan.af.mil/EM/TECH/sd_nonth.htm.
21. B. Gellert and U. Kogelschatz, Appl. Phys. B **52**, 14 (1991).
22. B. Gellert, H. Esrom and U. Kogelschatz, ABB Review **3/91**, 21 (1991).
23. D. C. Lorents, Physica **82C**, 19 (1976).
24. C. W. Werner, E. V. George, P. W. Hoff and Ch. K. Rhodes, IEEE J. Quantum Electronics **13**, 769 (1977).
25. P. Moutard, P. Laporte, J. L. Subtil, N. Damany and H. Damany, J. Chem. Phys. **88**, 7485 (1988).
26. C. K. Rhodes, IEEE J. Quantum Electronics **10**,153 (1974).
27. D. J. Eckstrom, H. H. Nakano, D. C. Lorents, T. Rothem, J. A. Betts, M. E. Lainhart, D. A. Dakin and J. E. Maenchen, J. Appl. Phys. **64,** 1679 (1988).
28. F. Mrachal, Ph.D. thesis, Universite Paul Sabatier de Toulouse, 1996.
29. Ch. K. Rhodes, Excimer Lasers, Springer, Berlin, 47 (1979).
30. P. K. Lecichner, Phys. Rev. A **8**, 815 (1973).
31. B. Schneider and J. S. Cohen, J. Chem. Phys. **61**, 3240 (1974).

32. B. Schneider and J. S. Cohen, J. Chem. Phys. **61**, 3240 (1974) [Ref. 3.3].

33. T. Oka, K. Raama Rao, J. Redgath and R. Firestone, J. Chem. Phys. **61**, 4740 (1974).

34. N. Thonnard and G. S. Hurst, Phys. Rev. A **5**, 1110 (1972).

35. R. Bocique and P. Mortier, J. Phys. D **3**, 1905 (1970).

36. J. W. Keto, R. E. Gleason and G. K. Walters, Phys. Rev. Lett. **33**, 1375 (1974).

37. P. K. Leichner and R. J. Ericson, Phys. Rev. A **9**, 251 (1974).

38. B. Eliasson and U. Kogelschatz, IEEE Trans. Plasma Sci. **19**, 1063 (1991).

39. D. Lindau and H. F. Dobele, Rev. Sci. Instrum. **59**, 565 (1988).

40. P. G. Wilkinson and E. T. Bryam, Appl. Opt. **4**, 581 (1965).

41. A. R. Calloway, T. A. Galantowicz and W. R. Fenner, J. Vac. Sci. Technol. A **1**, 534 (1983).

42. J. Kawanaka, S. Kubodera, W. Sasaki, k. Kurosawa, K. Mitsuhashi and T. Igarashi, IEEE J. Selected Topics in Quantum Electron. **1**, 852 (1995).

43. K. Mitsuhashi, T. Igarashi, M. Komori, T. Takada, E. Futagami, J. Kawanaka, S. Kubodera, K. Kurosawa and W. Sasaki, Opt. Lett. **20**, 2423 (1995).

44. G. N. Gerasimov, B. E. Krylov, R. Hallin, A. Arnesen and F. Heijkenskjold, Opt. and Spec. **83**, 576 (1997).

45. B. Eliasson and U. Kogelschatz, IEEE Trans. on Plasma Sci. **19**, 309 (1991).

46. M. Kitamura, K. Mitsuka and H. Sato, Appl. Surf. Sci. **79/80**, 507 (1994).

47. A. D. White, J. Appl. Phys. **30**, 711 (1959).

48. G. Schaefer and K. H. Schoenbach, Physics and applications of pseudo sparks, Plenum Press, New York, 55 (1990).

49. P. Gill and C. E. Webb, J. Phys. D: Appl. Phys. **10**, 299 (1977).

50. P. F. Little and A. von Engle, Proc. Roy. Soc. A **224**, 209 (1954).

51. D. J. Sturges and H. J. Oskam, J. Appl. Phys. **37**, 2405 (1966).

52. T. Musha, J. Phys. Soc. Japan **17**, 1440 (1962).

53. A. Fiala, L.C. Pitchford, and J.P. Boeuf, Proc. XXII Int. Conf. on Phenomena in Ionized Gases, Hoboken, 1995, Contr. Papers 4, 191.

54. V. S. Borodin and Y. M. Kagan, Sov. Phys. –Tech. Phys. **11**, 131 (1966).

55. E. Badareu, C. Popovici and M. Somesan, Rev. Roum. Phys. **12**, 1 (1967).

56. W. P. Allis, Proc. Int. Conf. Ionization Phenomena in Gases, Venice, 1957, 50.

57. H. Helm, Z. Naturforschung **27**a, 1812 (1972).

58. K.H. Schoenbach, R. Verhappen, T. Tessnow, F. E. Peterkin, and W. W. Byszewski, Appl. Phys. Lett. **68**, 13 (1996).

59. J. W. Gewartowski and H. A. Watson, Principles of Electron Tubes, Princeton, NJ, 561 (1964).

60. K. H. Schoenbach, A. El-Habachi, W. Shi, and M. Ciocca, Plasma Sources Sci. Technol. **6**, 468 (1997).

61. F. W. Aston, Proc. R. Soc. A **79**, 80 (1907).

62. J. D. Cobine, Gaseous Conductors, Dover, New York, 289 (1958).

63. J. Christiansen, Physics and applications of pseudo sparks, Plenum Press, New York, 1 (1990).

64. A. R. Samson, Techniques of Vacuum Ultraviolet Spectroscopy, Pied Publication, Lincoln, Nebraska, 212 (1980).

65. Erik Schoeffel, McPherson, Inc., Chelmsford, MA, private communication.

66. Patrick Lewis, UVP, Inc., Upland, CA, private communication.

67. Joseph Ametepe, College of William and Mary, Williamsburg, VA, private communication.

68. A. El-Habachi and K. H. Schoenbach, Appl. Phys. Lett. **72,** 22 (1998).

69. K.H. Schoenbach, A. El-Habachi, W. Shi, and M. Ciocca, Conf. Record IEEE Intern. Conf. Plasma Science, San Diego, CA, 1997, 239.

70. K.H. Schoenbach, M. Ciocca, A. El-Habachi, W. Shi, F. Peterkin, and T. Tessnow, Proc.12th Intern. Conf. on Gas Discharges and their Applications, Greifswald, Germany, 1997, 280.

71. K. H. Schoenbach, A. El-Habachi, W. Shi, and M. Ciocca, Proc. XXIII Intern. Conf. on Phenomena in Ionized Gases, Toulouse, France, 1997, V22.

72. R. L. Kelly, Rep.ORNL-5922 Oak Ridge National Lab., Oak Ridge, TN,1982.

73. A. El-Habachi and K. H. Schoenbach, Submitted to Appl. Phys. Lett..

74. A. El-Habachi and K. H. Schoenbach, Conf. Record IEEE Intern. Conf. Plasma Science, Raleigh, NC, 1998, 125.

75. J.K. Rice and A.W. Johnson, J. Chem. Phys. **63**, 5235 (1975).

76. J. R. Acton and J. D. Swift, Cold Cathode Discharge Tubes, Academic Press, New York, 270 (1963).

77. W. Wieme and J. Lenaerts, J. Chem. Phys. **74**, 483 (1981).

78. K. Watanabe and M. Zelikoff, J. Opt. Soc. Am. **43**,753 (1953).

79. A. Ryer, Light Measurement Handbook, Technical Publications Dept., International Light, MA (1998).

80. W. Shi and K.H. Schoenbach, Conf. Record IEEE Intern. Conf. Plasma Science, Raleigh, NC, 1998, 283.

81. W. Shi, M.Sc. thesis, Old Dominion University, 1998.

APPENDIX A

A.1 Kinetic Model for Xenon

A complete list of the kinetic processes in xenon is given in table A.1[27], together with the rates of different reactions.

Table A.1. Kinetic model of xenon.

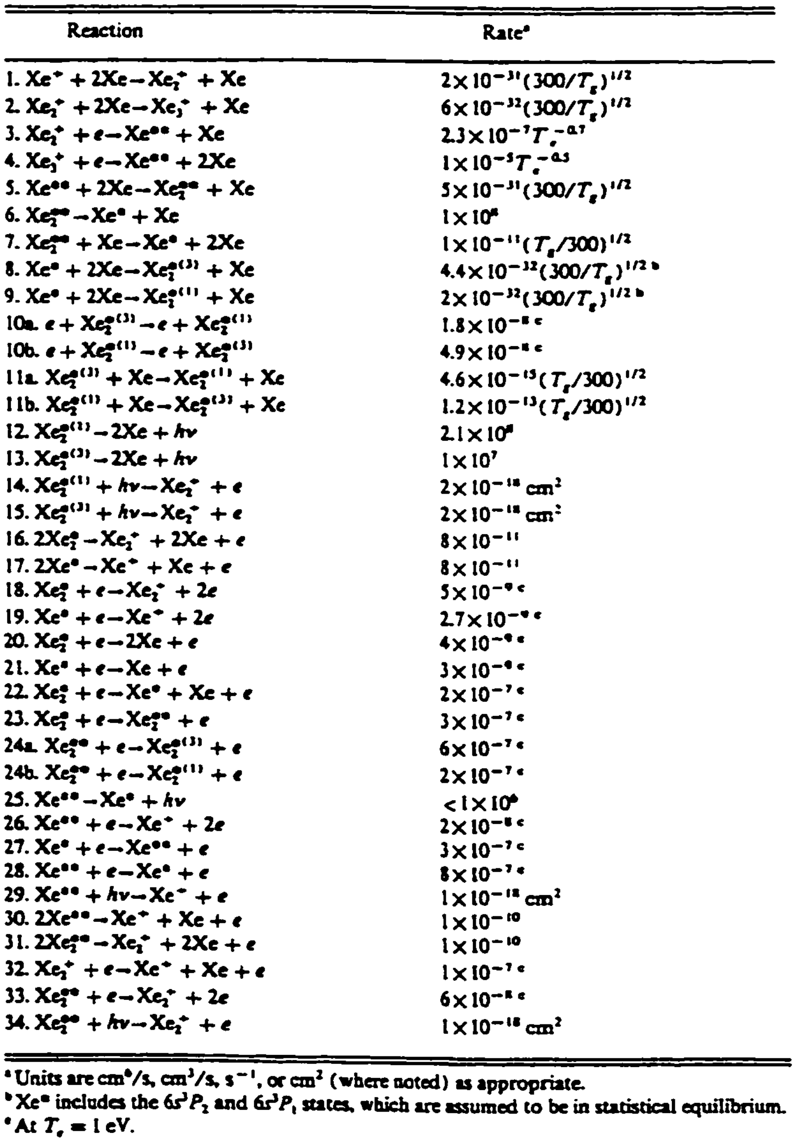

Reaction	Rate[a]
1. $Xe^{+} + 2Xe \rightarrow Xe_2^{+} + Xe$	$2\times10^{-31}(300/T_g)^{1/2}$
2. $Xe_2^{+} + 2Xe \rightarrow Xe_3^{+} + Xe$	$6\times10^{-32}(300/T_g)^{1/2}$
3. $Xe_2^{+} + e \rightarrow Xe^{**} + Xe$	$2.3\times10^{-7}T_e^{-0.7}$
4. $Xe_3^{+} + e \rightarrow Xe^{**} + 2Xe$	$1\times10^{-5}T_e^{-0.5}$
5. $Xe^{**} + 2Xe \rightarrow Xe_2^{**} + Xe$	$5\times10^{-31}(300/T_g)^{1/2}$
6. $Xe_2^{**} \rightarrow Xe^{*} + Xe$	1×10^{8}
7. $Xe_2^{**} + Xe \rightarrow Xe^{*} + 2Xe$	$1\times10^{-11}(T_g/300)^{1/2}$
8. $Xe^{*} + 2Xe \rightarrow Xe_2^{*(3)} + Xe$	$4.4\times10^{-32}(300/T_g)^{1/2}$ [b]
9. $Xe^{*} + 2Xe \rightarrow Xe_2^{*(1)} + Xe$	$2\times10^{-32}(300/T_g)^{1/2}$ [b]
10a. $e + Xe_2^{*(3)} \rightarrow e + Xe_2^{*(1)}$	1.8×10^{-8} [c]
10b. $e + Xe_2^{*(1)} \rightarrow e + Xe_2^{*(3)}$	4.9×10^{-8} [c]
11a. $Xe_2^{*(3)} + Xe \rightarrow Xe_2^{*(1)} + Xe$	$4.6\times10^{-15}(T_g/300)^{1/2}$
11b. $Xe_2^{*(1)} + Xe \rightarrow Xe_2^{*(3)} + Xe$	$1.2\times10^{-13}(T_g/300)^{1/2}$
12. $Xe_2^{*(1)} \rightarrow 2Xe + h\nu$	2.1×10^{8}
13. $Xe_2^{*(3)} \rightarrow 2Xe + h\nu$	1×10^{7}
14. $Xe_2^{*(1)} + h\nu \rightarrow Xe_2^{+} + e$	2×10^{-18} cm^2
15. $Xe_2^{*(3)} + h\nu \rightarrow Xe_2^{+} + e$	2×10^{-18} cm^2
16. $2Xe_2^{*} \rightarrow Xe_2^{+} + 2Xe + e$	8×10^{-11}
17. $2Xe^{*} \rightarrow Xe^{+} + Xe + e$	8×10^{-11}
18. $Xe_2^{*} + e \rightarrow Xe_2^{+} + 2e$	5×10^{-9} [c]
19. $Xe^{*} + e \rightarrow Xe^{+} + 2e$	2.7×10^{-9} [c]
20. $Xe_2^{*} + e \rightarrow 2Xe + e$	4×10^{-9} [c]
21. $Xe^{*} + e \rightarrow Xe + e$	3×10^{-9} [c]
22. $Xe_2^{*} + e \rightarrow Xe^{*} + Xe + e$	2×10^{-7} [c]
23. $Xe_2^{*} + e \rightarrow Xe_2^{**} + e$	3×10^{-7} [c]
24a. $Xe_2^{**} + e \rightarrow Xe_2^{*(3)} + e$	6×10^{-7} [c]
24b. $Xe_2^{**} + e \rightarrow Xe_2^{*(1)} + e$	2×10^{-7} [c]
25. $Xe^{**} \rightarrow Xe^{*} + h\nu$	$<1\times10^{6}$
26. $Xe^{**} + e \rightarrow Xe^{+} + 2e$	2×10^{-8} [c]
27. $Xe^{*} + e \rightarrow Xe^{**} + e$	3×10^{-7} [c]
28. $Xe^{**} + e \rightarrow Xe^{*} + e$	8×10^{-7} [c]
29. $Xe^{**} + h\nu \rightarrow Xe^{+} + e$	1×10^{-18} cm^2
30. $2Xe^{**} \rightarrow Xe^{+} + Xe + e$	1×10^{-10}
31. $2Xe_2^{**} \rightarrow Xe_2^{+} + 2Xe + e$	1×10^{-10}
32. $Xe_2^{+} + e \rightarrow Xe^{+} + Xe + e$	1×10^{-7} [c]
33. $Xe_2^{**} + e \rightarrow Xe_2^{+} + 2e$	6×10^{-8} [c]
34. $Xe_2^{**} + h\nu \rightarrow Xe_2^{+} + e$	1×10^{-18} cm^2

[a] Units are cm^6/s, cm^3/s, s^{-1}, or cm^2 (where noted) as appropriate.

[b] Xe^{*} includes the $6s^3P_2$ and $6s^3P_1$ states, which are assumed to be in statistical equilibrium.

[c] At $T_e = 1$ eV.

A.2 Monochromator Grating

Most monochromators use gratings to disperse light into the spectrum. A typical diffraction grating consists of a substrate, with a large number of parallel grooves ruled or replicated in its surface and overcoated with a reflecting material such as aluminum. The quality and spacing of the grooves are crucial to the performance of the grating. The wavelength of reflected light varies with angle, as defined by the grating equation, where m is the order of the spectrum (an integer). Only wavelengths which satisfy the grating equation pass through the exit slit. The remainder of the light is scattered and absorbed inside the monochromator. As the grating is rotated, the angles α and β change, although the difference between them remains constant and is fixed by the geometry of the monochromator.

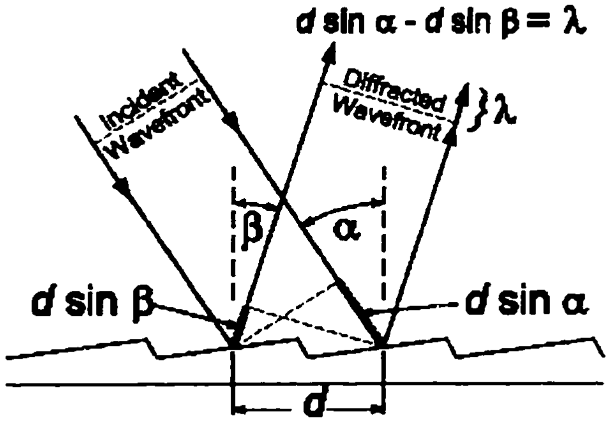

Grating Equation:
$m\lambda = d(\sin\alpha \pm \sin\beta)$

A.3 Blaze Angle

If monochromatic light strikes a grating then a fraction of it is diffracted into each order. The fraction diffracted into any order can be termed the efficiency of the grating in that order. Gratings are not equally efficient at all wavelengths for a variety of detailed reasons. The efficiency can be tuned by changing the groove facet angles, or shape and depth. The optimization of efficiency by appropriate groove shaping has become known as blazing. The blaze wavelength is the wavelength for which the grating is most efficient.

A.4 Point Source Approximation

Consider a point (sufficiently small) source of radiant energy, which is radiating uniformly in all directions. If the rate at which energy is radiated is P watts, then the source has a radiant intensity J of P/4π watts per steradian. Of course there are no truly point sources and no practical sources, which radiate uniformly in all directions. But if a source is quite small relative to its distance, it can be treated as a point, and its radiation, in the directions in which it does radiate, can be expressed in watts per steradian.

For a surface, which is r cm from the source, then 1 cm^2 of this surface will subtend $1/r^2$ steradians from the source. The irradiance H on this surface is the incident radiant power per unit area and is obtained by multiplying the intensity of the source in watts per steradian by the solid angle subtended by the unit area. Thus, the irradiance is given by:

$$H = \frac{J}{r^2} = \frac{P}{4\pi r^2}$$

The units of irradiance are watts per square centimeter ($\mathrm{W/cm}^2$).

A.5 Deuterium Lamp Calibration

In calibrating the deuterium lamp down to 160 nm, William and Mary group [67] employed a published extrapolation technique. They measured the normalized spectral radiance of the deuterium lamp and compared it to the normalized irradiance data supplied by the factory over the wavelength range of 200 to 320 nm. Plotting the two data sets on the same wavelength and intensity scale, they found a strong agreement over this wavelength range with a root mean square deviation of about 1%. Since the wavelength distribution of the spectral radiance is nearly the same as that of the spectral irradiance, extrapolation of the deuterium lamp spectral irradiance curve down to 160 nm was possible allowing them to calibrate the lamp output down to such wavelength. Fig. A.1 shows the calibrated spectrum of the deuterium lamp.

A.6 Mercury Lamp Calibration

The data measured with our monochromator was confirmed using manufacturer data. Considering the ratio between the 184.9 nm and the 253.7 nm lines in the mercury arc spectrum (Fig. A.2), and assuming that the quartz envelope of the lamp transmits light at 184.9 nm with 60% efficiency, the ratio between the two lines is found to be 25.

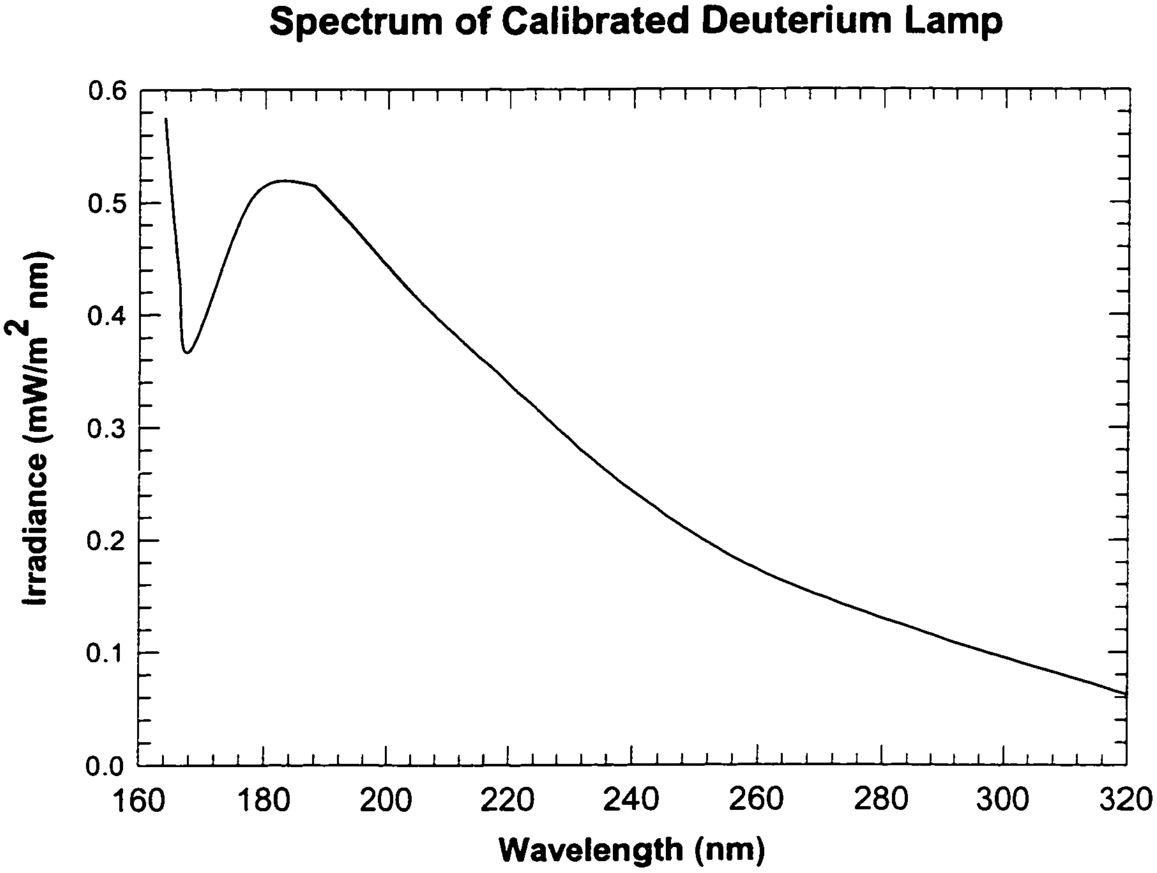

FIG. A.1. Calibrated deuterium lamp spectrum [67].

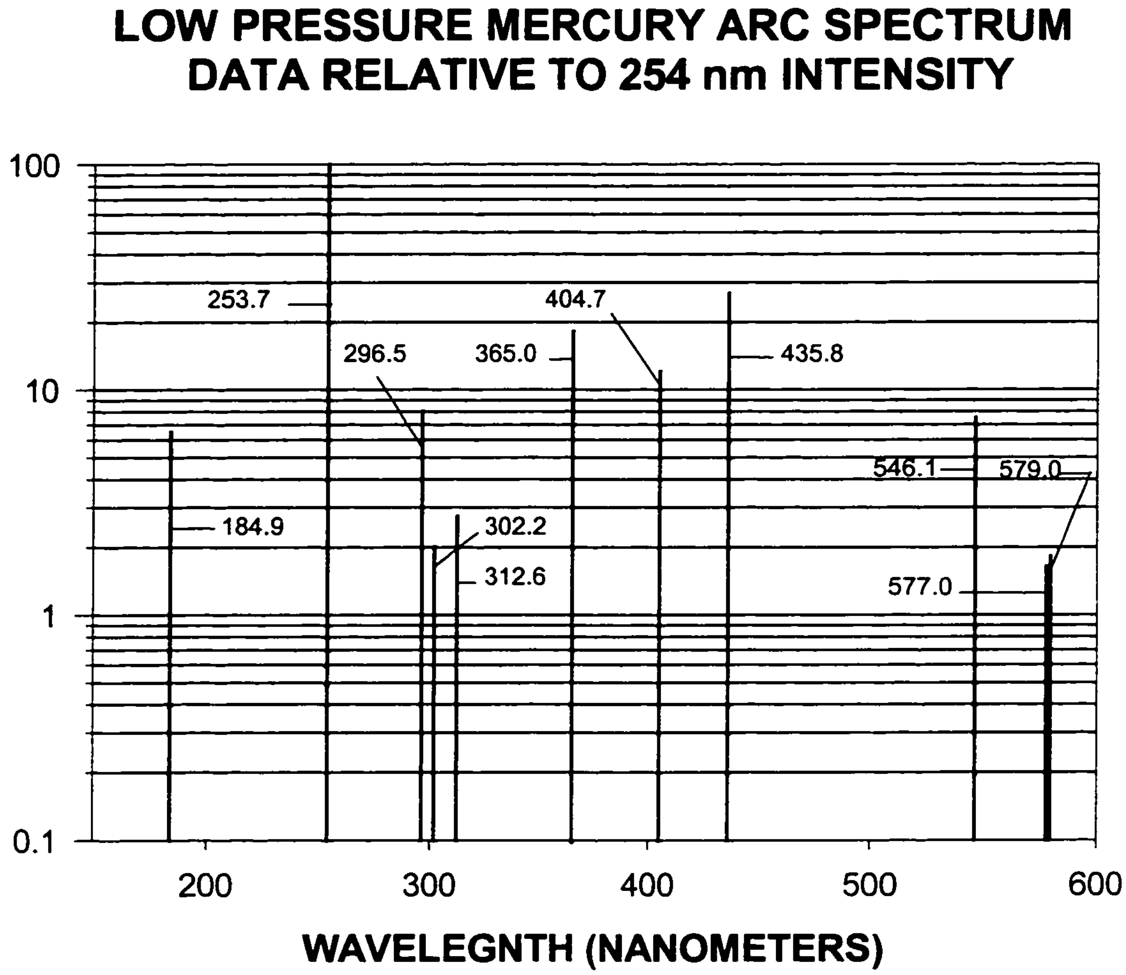

FIG.A.2. Low pressure mercury arc spectrum.

A.7 Radiometer Measurements

Fig. A.3 shows the responsivity of the SED185 detector supplied from the manufacturer along with the fitted function used in our measurement.

The fitted function, D(λ), is:

$$D(\lambda) = a\left(\frac{c-1}{c}\right)^{\frac{1-c}{c}}\left[\frac{x-x_0}{b}+\left(\frac{c-1}{c}\right)^{\frac{1}{c}}\right]^{c-1} * \exp^{-\left[\frac{x-x_0}{b}+\left(\frac{c-1}{c}\right)^{\frac{1}{c}}\right]^{c}} + \frac{c-1}{c}$$

where a = 99.0961

b = 24.2232

c = 1.7502

and x_0 = 184.2397

Fig. A.4 shows the fitted function, $P_R(\lambda)$, for the excimer line profile.

$$P_R(\lambda) = a\exp^{-0.5\left(\frac{x-x_0}{b}\right)^2}$$

where a = 594.0541

b = 8.2626

x_0 = 170.632

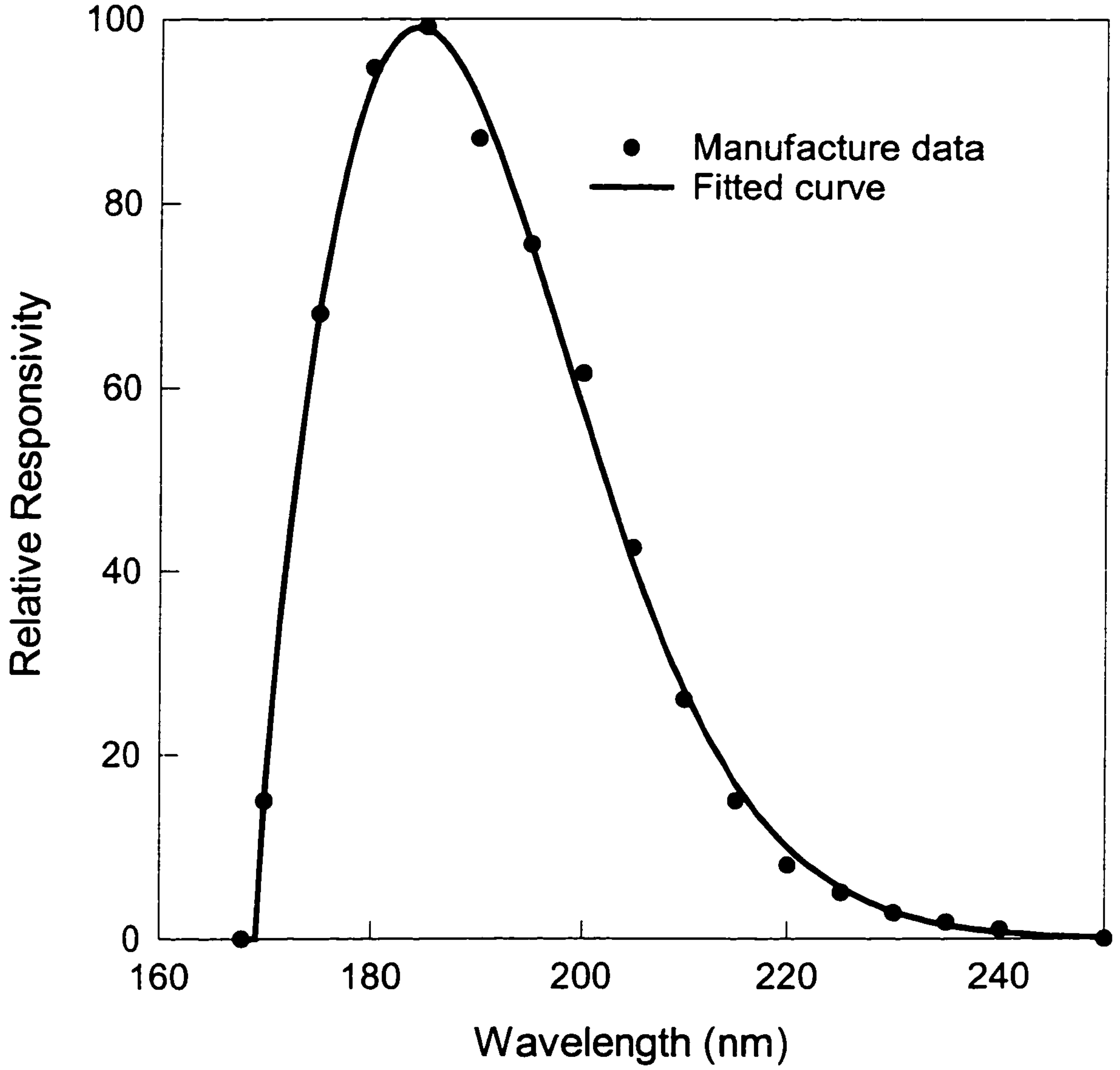

FIG. A.3. Spectral responsivity of the SED 185 deep UV detector.

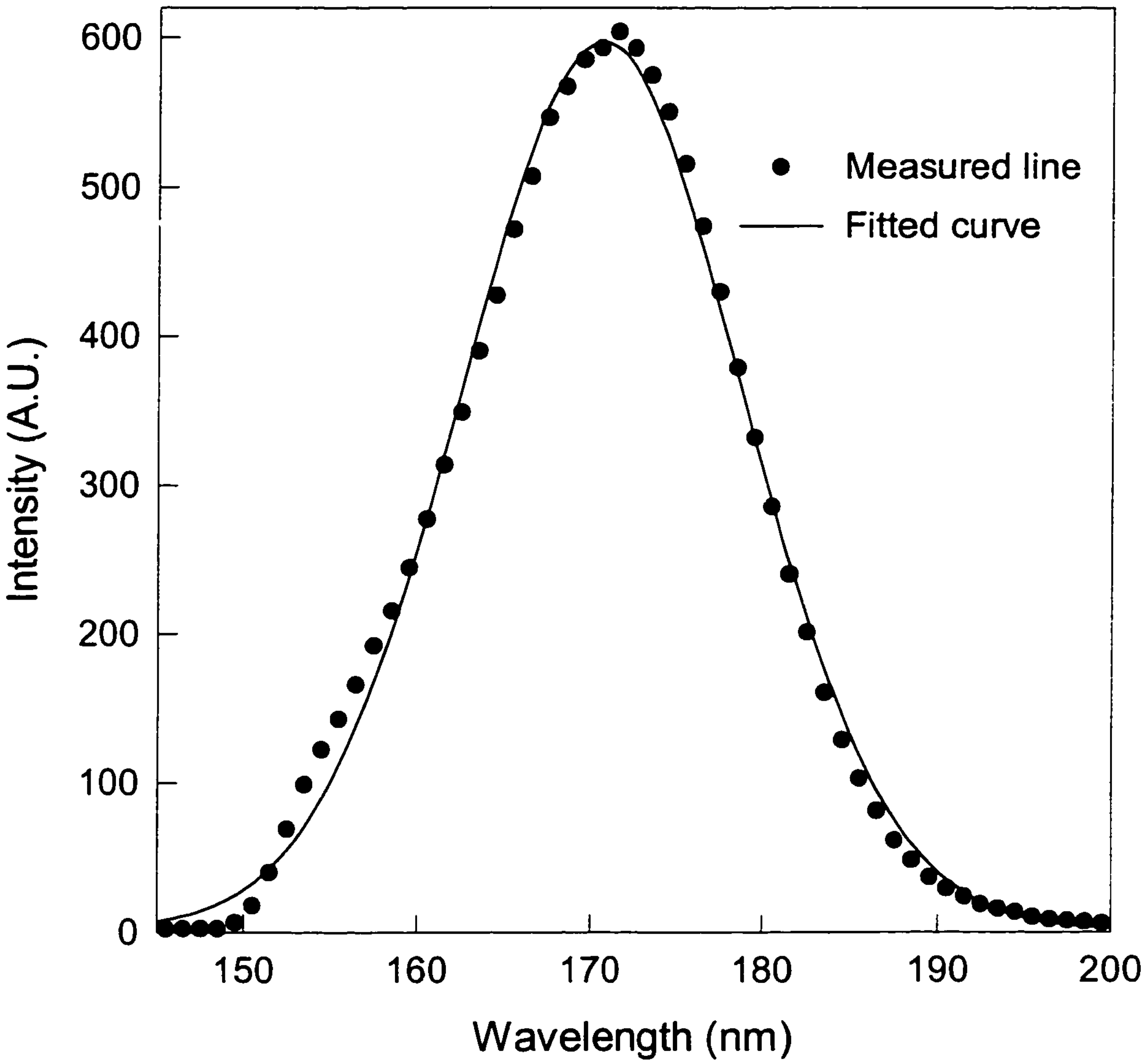

FIG. A.4. Curve fitting of the xenon excimer line.

VITA

Ahmed El-Habachi

Current Address:
920 Rockbridge Ave. #119
Norfolk, VA23508, USA
Tel: (757) 4891001
Fax: (757) 4891998
Habachi@ee.odu.edu

Permanent Address:
6 Abdel Hamid El Abady st.
Roushdy, Alexandria, EGYPT
Tel: (203) 5424690
Fax: (203) 5871447
nhabachi@hotmail.com

Education:

Doctorate of Philosophy in Electrical Engineering — August 1998
Old Dominion University, Norfolk, VA23529
GPA: 4.0/4.0

Master of Science in Electrical Engineering — March 1994
Alexandria University, Egypt

Bachelor of Science in Electrical Engineering — June 1991
Power Systems and Automatic Control section
Grade: Distinction with degree of honor (Highest grade)

Work Experience:

Research Assistant, Peri laboratory
Old Dominion University, Norfolk, VA (August. 1995-present)

- Designed gas discharge vacuum chamber for the Microhollow Cathode Discharge (MHCD)
- Built a VUV spectroscopy system and different electrical circuits for the MHCD
- Automated the whole MHCD experiment by using stepper motor driver and the required data acquisition techniques

Teacher Assistant, Electrical Power Engineering Dept., Faculty of Engineering, Alexandria University, Egypt (1991-1995)

- Taught Fundamental of electric engineering, electric circuit, automatic control, power system protection and electrical measurements
- Instructed undergraduate lab: fundamental of electrical engineering, circuits, computer, measurement, electronics and electrical machines
- Helped in graduation projects of transmission line design, stability in power systems, relay coordination and high & low voltage distribution

IMAGE EVALUATION
TEST TARGET (QA-3)

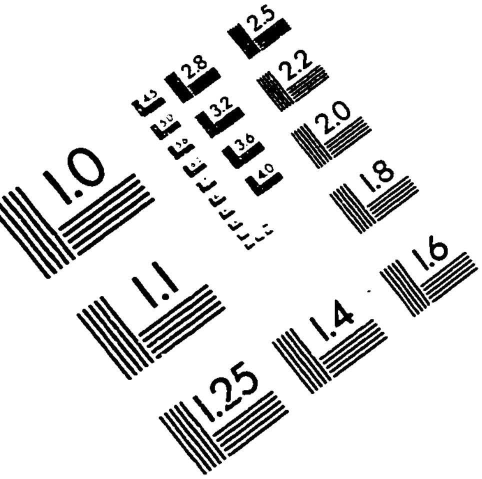

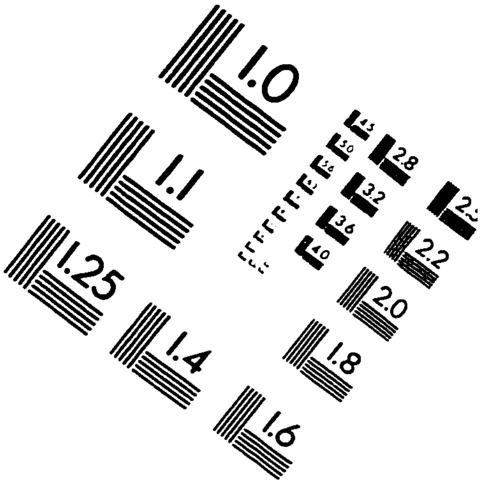

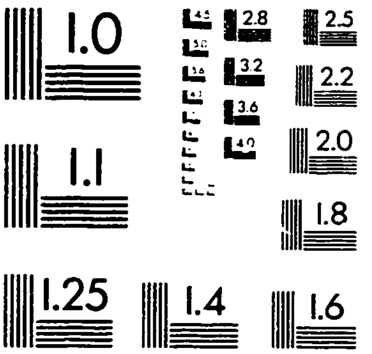

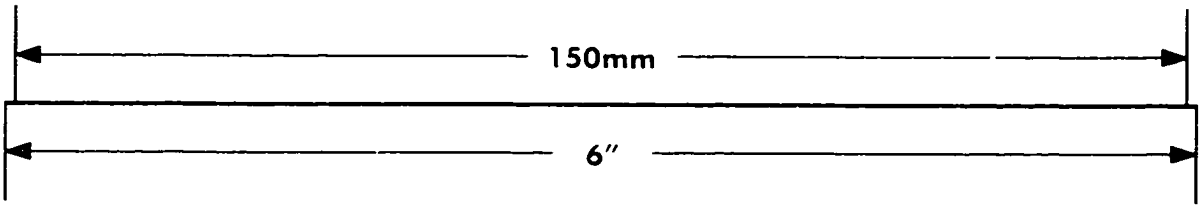

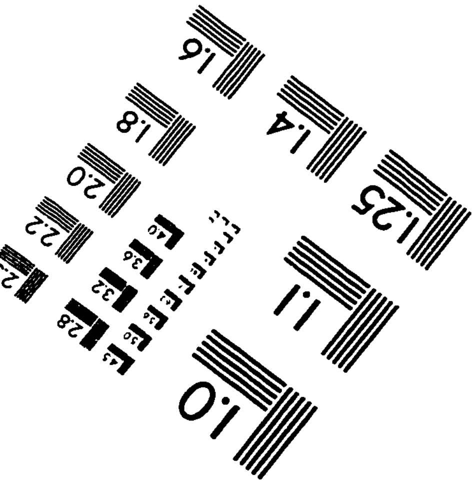

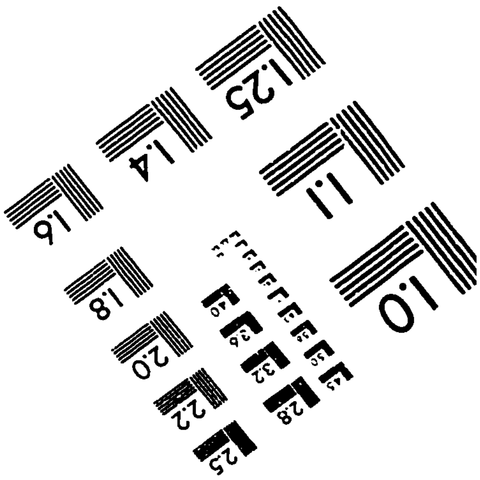

APPLIED IMAGE . Inc
1653 East Main Street
Rochester, NY 14609 USA
Phone: 716/482-0300
Fax: 716/288-5989